

**Biosensor Arrays for Molecular Source Identification in Mass-Transport
Systems**

by

Maryam Abolfath Beygi Dezfooli

B.Sc., Electrical and Computer Engineering, University of Tehran, Iran, 2005

M.Sc., Electrical Engineering, University of Tehran, Iran, 2008

A THESIS SUBMITTED IN PARTIAL FULFILLMENT OF
THE REQUIREMENTS FOR THE DEGREE OF

DOCTOR OF PHILOSOPHY

in

The Faculty of Graduate and Postdoctoral Studies

(Electrical and Computer Engineering)

THE UNIVERSITY OF BRITISH COLUMBIA
(Vancouver)

December 2013

© Maryam Abolfath Beygi Dezfooli, 2013

Abstract

In this thesis, we investigate the use of biosensor arrays for detection of molecular species in dynamical fluid systems. First, we construct dynamical models for the transport of target molecules in a fluid over an array of surface-based biosensors. Using multiple time and length scales in the system dynamics, we develop a novel approximate model for the system. The derived model is an extension of the two-compartment model, which is used in the analysis of mass-transfer binding experiments. Then, we investigate how measurements of multiple biosensors can improve the estimation of target molecule concentration in a mass transfer system. The estimation problem is solved as a nonlinear least squares problem based on the derived model. The properties of the finite-sample estimator is investigated by deriving analytic expressions and Monte Carlo simulations. As an example, the results are illustrated for a protein-based biosensor. Second, we address the problem of detecting minute concentrations (nano to pico-molar) of target molecules with a single sensor. It is shown that substantial improvements in the response rate can be obtained by distributing the sensing surface area to form an array of spaced smaller sensors while the total sensing area remains fixed. The output signals of the individual sensors in the array are combined to form a single output signal for measurements. Formulas are derived for quantifying the improvement of the array response and for optimizing the size of the sensors. The analytical results are compared with experimental data for a protein-based biosensor and a surface plasmon resonance biosensor. Finally, we construct a mathematical proof for the accuracy of the two-compartment model, which is the basis of most of our analyses.

Preface

I am the first author and principal contributor of all chapters. All chapters are co-authored by Prof. Vikram Krishnamurthy, who supervised the research. Chapter 4 is also co-authored by Dr. Bruce Cornell*, who provided us with experimental data and insightful information.

The following publications describe the work completed in this thesis. In some cases, the conference papers contain materials overlapping with the journal papers.

Journal Papers

- M. Abolfath-Beygi and V. Krishnamurthy, "Multiple surface-based sensors for enhanced molecular detection in fluid flow systems," *IEEE Sensors Journal*, vol. 13, no. 4, pp. 1265-1273, Apr. 2013, doi: 10.1109/JSEN.2012.2229268.
- M. Abolfath-Beygi and V. Krishnamurthy, "Biosensor arrays for estimating molecular concentration in fluid flows," *IEEE Trans. on Signal Processing*, vol. 62, no. 1, pp. 239–251, Jan. 2014, doi: 10.1109/TSP.2013.2287680.

Conference Papers

- M. Abolfath-Beygi and V. Krishnamurthy, "Detection of target molecules using surface-based biosensor arrays in fluid flows," in *Proc. of the International Conference on Acoustics, Speech and Signal Processing (ICASSP)*, pp. 3913–3916, 2012.

*Surgical Diagnostics Ltd, St Leonards, Australia

- M. Abolfath-Beygi and V. Krishnamurthy, "Biosensor arrays for collaborative detection of analytes," in *Proc. of the Asilomar Conference on Signals, Systems and Computers*, pp. 1699–1703, 2011.
- M. Abolfath-Beygi and V. Krishnamurthy, "Cooperative maximum likelihood estimation for fluid flow dynamics in biosensor arrays," in *Proc. of the International Conference on Acoustics, Speech and Signal Processing (ICASSP)*, pp. 3788–3791, 2011.

Table of Contents

Abstract	ii
Preface	iii
Table of Contents	v
List of Tables	viii
List of Figures	x
Acknowledgments	xv
Dedication	xvi
1 Introduction	1
1.1 Estimation in Distributed Parameter Systems: Basic Concepts	5
1.2 Estimation of Molecular Concentration in Advection-Diffusion Systems	8
1.3 Diffusion, Advection and Reaction on Surface-Based Biosensors	11
1.3.1 Mass-Transport and Reaction Interplay	11
1.3.2 Mass-Transport Phase Diagram	12
1.4 Two Case-studies	16
1.4.1 Ion Channel Switch Biosensor	16
1.4.2 BIACORE: A Surface Plasmon Resonance Biosensor	19

Table of Contents

1.5	Contributions and Results	20
1.6	Thesis Organization	23
2	Multi-Compartment ODE model: Analysis	25
2.1	PDE Model for Analyte Flow Over a Biosensor Array	27
2.2	Multi-Compartment Model Approximation	32
2.2.1	Review of the Two-Compartment Model	33
2.2.2	The Multi-Compartment Model	36
2.3	Case-Study: Ion Channel Switch Biosensor	40
2.3.1	Dynamics of Analyte Flow on Ion Channel Switch Biosensor	40
2.3.2	Illustration of the Accuracy of the Multi-Compartment Model	42
2.4	Summary	45
3	Estimating Molecular Concentrations in Fluid Flows	49
3.1	Least Squares Estimator of the Initial Concentration	51
3.2	Analytic expressions for the variance and bias of the estimate \hat{A}^*	53
3.3	Estimation Results for an Array of Ion Channel Switch Biosensor	58
3.4	Summary	61
4	Improving Analyte Collection Rate on Multiple Sensors	66
4.1	Multiple-Sensor Array can Mitigate Mass-Transport Limits	69
4.1.1	Binding Kinetics in the Mass-Transport Phase Diagram	70
4.1.2	Improving Analyte Collection Rate Using Multiple Sensors	72
4.2	Case-Study I: Ion Channel Switch Biosensor	77
4.3	Case-Study II: BIACORE Biosensor	79
4.3.1	Effect of Flow Rate on Analyte Collection Rate	82
4.4	Summary	83

Table of Contents

5	On the Accuracy of the Two-Compartment Model	87
5.1	The Two-Compartment Model Based on the Lévêque Solution	88
5.2	Proof of the Accuracy of the Two-Compartment Model	94
5.3	Summary	107
6	Conclusions and Discussion	108
6.1	Research Contributions	108
6.2	Discussion and Future Work	111
	Bibliography	115

List of Tables

3.1	Comparison between the simulated and approximate values for the variance and bias of the estimate \hat{A}^* obtained by (3.1): The simulated and analytical values of the standard deviation and normalized bias for $S = 300$ time samples are shown. The sampling rate is 1 sample/s. The target molecule concentration at the inlet of the flow chamber is $A^* = 10^{-8}$ Mol/m ³ . The noise variance is set at $\sigma^2 = 0.1\bar{D}(0)$, where $\bar{D}(0)$ is the value of the response at $t = 0$	62
3.2	The variations of the first and second terms on the right-hand side of (3.7) for the results of Table 3.1.	62
4.1	Maximum attainable improvement in analyte collection rate, defined in (4.4), for two real-life biosensors; The ion channel switch biosensor (a) and the BIACORE biosensor (b). The improvement is obtained by replacing a single sensor with a uniform array of N smaller sensors of similar type. The analyte injection concentration is $A^* = 1\text{pM}$ (a) and $A^* = 25\text{nM}$ (b). The total length of the sensors in each array is $L = 2\text{mm}$ (a) and $L = 1\text{mm}$ (b), which is equal to the length of the initial single sensor. The sensor spacing is considered to be sufficiently large in each case to allow the analyte concentration to reach its maximum value in the gaps between the sensors. (Parameters are specified in Section 4.2 and Section 4.3 and their values for the initial single sensor are given in Table 4.2 and Table 4.3.)	68

List of Tables

4.2	Parameter values for streptavidin-biotin interaction on ICS biosensor	78
4.3	Parameter values for the BIACORE biosensor	81
4.4	The maximum improvement in analyte collection rate for different flow rates: The improvement, as defined in (4.4), is obtained by replacing a single BI- ACORE biosensor with a uniform array of two BIACORE biosensors. The total sensing surface area is fixed. The total length of the biosensors in the array is $L = 1\text{mm}$, which is equal to the length of the single biosensor. Other parameter values are given in Table 4.3. The sensor spacing is considered to be sufficiently large in each case to allow the analyte to replenish between the individual sensors.	83

List of Figures

1.1	Solution with target molecule (analyte) concentration A^* flows with volumetric flow rate Q through a flow chamber of height h and width w_c over a biosensor of length L and width w_s . The biosensor is functioning with θ receptors per unit area. The kinetic rate constants for the first-order binding reaction are k_{on} and k_{off} . The analyte diffusion constant is γ . The dimensionless Damkohler and Péclet numbers are obtained by (1.4) and (1.6).	13
1.2	A typical mass-transport phase diagram for the binding kinetics of a biosensor [1]: Region (i) corresponds to full collection regimes, where the analyte binding rate on the biosensor is equal to the input advective flux. In region (ii), the depletion region on the biosensor surface is thin compared to both the height of the flow chamber and the biosensor length. In this region, the mass-transport limited analyte binding rate, at the steady state, is obtained by (1.7). The depletion region in region (iii) is much thinner than the height of the flow chamber but comparable to the biosensor length itself. The mass-transport limited analyte binding rate, in this region, is computed by Ackerberg et al [2]. Region (iv) has not, to our knowledge, been studied thus far.	15
1.3	Example: Ion Channel Switch Biosensor [3]. When analyte binds to the antibodies, the conducting dimer is split into non-conducting channels.	18
1.4	An Ion Channel Switch (ICS) biosensor embedded in an impedance meter device.	18

List of Figures

1.5	Diagrammatic illustration of the surface plasmon resonance principle [4]	20
2.1	The physical dynamics is first described by a PDE model, which is converted to a multi-compartment ODE model for further analysis.	26
2.2	An equally spaced linear array of three biosensors in a rectangular flow chamber. The fluid containing target molecules (analytes) enters from the left side. The analyte concentration at the inlet of the flow chamber is A^* as expressed in the boundary condition (2.4).	29
2.3	Formation of a depletion region above the biosensor surface in the flow chamber: The two-compartment model can describe the dynamics of the system in this flow profile. The analyte concentration in the outer compartment is constant, equal to the concentration at the inlet whereas the concentration in the depletion inner compartment is slowly varying.	33
2.4	Multi-compartment model for two successive biosensors in the array.	36
2.5	Convergence studies of the finite element solution of the PDE model (2.2)-(2.7): Convergence studies are performed by investigating (2.29). For the PDE model (2.2)-(2.7), (2.29) is formulated as (2.30), where $A(t, \cdot, \cdot)$ and $\mathbf{u}_i(t, \cdot)$ are the reference solutions of the PDE model obtained for the finest mesh size $\Delta = 10^{-5}\text{m}$. The convergence order is obtained as $\lambda \approx 1$	45
2.6	The normalized error (2.28) between the multi-compartment ODE model (2.15)-(2.19) and the PDE model (2.2)-(2.7) for $A^* = 10^{-8} \text{ Mol/m}^3$ (a) and $A^* = 10^{-11} \text{ Mol/m}^3$ (b). The flow rate is $Q = 10 \mu\text{L/min}$. There are $N = 4$ biosensors with the length $L = 2 \text{ mm}$ and spacing $d = 1 \text{ mm}$ in the flow chamber.	46

- 2.7 The normalized error (2.28) between the multi-compartment ODE model (2.15)-(2.19) and the PDE model (2.2)-(2.7) for different flow rates for $A^* = 10^{-8}$ Mol/m³ (a) and $A^* = 10^{-11}$ Mol/m³ (b) for the second (a) and fourth (b) biosensor. There are $N = 4$ biosensors in the flow chamber in each case, but the results are illustrated for only the biosensor with the maximum variations in the error. The biosensor length and spacing are respectively $L = 2$ mm and $d = 1$ mm. 47
- 3.1 The response $\tilde{g}(A, t) = F(\bar{\mathbf{u}}_1(t))$ of a single biosensor, obtained by the two-compartment model (2.12)-(2.14) with $A_1 = A$, is insensitive to low concentrations of target molecules. By increasing the concentration of target molecules, the sensitivity of $\tilde{g}(A, t)$ (the magnitude of the derivative $\partial\tilde{g}(A, t)/\partial A$) initially increases and then decreases to zero for large values of concentration. The response is plotted for a time horizon of 300s. 63
- 3.2 The ascending behaviour of d_i , defined in (3.16), is investigated by comparing $H(A)$ and $\alpha^2 H(\alpha A)$ (a), where $H(A)$ is defined in (3.17). The plot in the interval $A \in (A^m, A^n)$ is magnified (b). For the value of A in this interval, we have $\alpha^2 H(\alpha A) > H(A)$. In our example of the estimation problem, the concentration at the inlet of the flow chamber $A^* = 10^{-8}$ Mol/m³ belongs to this interval. Using $N \leq N^* = 4$ biosensors, for N^* obtained by (3.18), the variance of the estimation is decreased to less than $1/N$ of the variance obtained by a single biosensor. . . 64
- 3.3 The absolute error $e_i(t) = \bar{D}_i(t) - \bar{D}_i^{\text{ODE}}(t)$ between the responses of the PDE model (2.2)-(2.7) and the multi-compartment ODE model (2.15)-(2.19) for $A^* = 10^{-8}$ Mol/m³. The flow rate is $Q = 10$ μ L/min. The number of biosensors is $N = 4$. The biosensor length and spacing are respectively $L = 2$ mm $d = 1$ mm. 65

4.1	Depletion in analyte concentration along a sensor. (a): The analytes are bound close to the entry to the flow chamber causing a depletion in analyte concentration for subsequent binding sites and an overall slowing of the sensor response. (b): Replacing the sensor with two spaced out half-sized sensors allows analyte to be replenished between the individual sensors. . .	69
4.2	The variations of maximum improvement in analyte collection rate in the mass-transport limited regime, as defined in (4.7): The improvement is based on replacing a single sensor with N sensors while the total sensing area is fixed. The parameter k , defined in (4.5), is the ratio of the analyte collection rate on the single sensor to the input advective flux. By increasing the value of k , the attainable improvement in analyte collection rate reduces.	76
4.3	The response of a uniform array of N ICS biosensors for different values of N . The total sensing surface area is fixed. All the biosensors have the same width and their total length is $L = 2\text{mm}$. Other parameter values are given in Table 4.2. The analyte injection concentration is $A^* = 1\text{pM}$ (a) and $A^* = 10\text{pM}$ (b). The sensor spacing $d = \frac{5L}{N}$ is five times the length of individual sensors in the array.	80
4.4	The response of a uniform array of N BIACORE biosensors for different values of N . The total sensing surface area is fixed. The total length of the biosensors is $L = 1\text{mm}$. Relevant parameter values are given in Table 4.3. The analyte injection concentration is $A^* = 25\text{nM}$. The sensor spacing is $d = \frac{2L}{N}$	82

4.5	Comparison between the responses of a single BIACORE biosensor and a uniform array of two biosensors for different flow rates Q . The solid lines correspond to the single biosensor response and the dashed lines illustrate the responses of the two-biosensor arrays. The total sensing surface area is fixed. Relevant parameter values are given in Table 4.3. The analyte injection concentration is $A^* = 25\text{nM}$. The maximum sensor spacing is $d = \frac{2L}{N}$ for $Q = 60\mu\text{L}/\text{min}$	84
5.1	The fluid containing analytes enters from the left side of the flow chamber. The analyte concentration at the inlet is A^* as expressed in the boundary conditions in 5.6.	89

Acknowledgments

First and foremost, I offer my sincerest gratitude to my supervisor, Prof. Vikram Krishnamurthy, for his invaluable advice, insightful guidance, and enormous patience. He has improved the quality of my research and presentation by his constructive comments from the early stages of my research until the very end. He has supported me and encouraged me throughout my PhD study, introduced me to new ways of thinking, and provided me with excellent research topics.

I would like to extend my sincerest appreciation to Dr. Bruce Cornell, at Surgical Diagnostics, for providing me with experimental data and detailed experimental information.

I am also thankful to the members of my doctoral committee for their time and effort.

I wish to thank my friends at the University of British Columbia, who inspired me along the way, especially Mr. Vahid Shah-mansouri, Ms. Saeedeh Ebrahimi, and Mr. Rowshan Rahmanian.

I also wish to thank my dear husband, Aryan Navabi, for his patience, love and continuous support along completion of this work.

Lastly, and most importantly, I wish to thank my mom for her love and support, whose comforting words are worth more than diamonds. To her, I dedicate this thesis. I would also like to thank my dear sister, Parisa, for her love and kindness, who has always helped me through difficult times. I am also very thankful to my dear grand parents, Ehteram and Ali, for their love and continuous support. Without my family, I could not achieve this success and finish this road.

Dedication

With love, to my mom.

Chapter 1

Introduction

Biosensors are analytical devices that incorporate a biologically derived material or biomimetic component to interact with the chemical constituent under study. Detection of target molecules with a biosensor involves a biochemical mechanism, which is transformed into a measurable signal. The measured signal is then processed to infer the value of an unknown quantity such as the target molecule concentration. Biosensors have a wide range of applications in medical and clinical diagnosis, environmental monitoring, and water treatment facilities for detection of target molecules [5, 6, 7]. A common example of a commercial biosensor is the blood glucose biosensor [8], which uses an enzyme to break down blood glucose. In this thesis, we deal with surface-based biosensors. A surface-based sensor is one in which target molecules in solution are captured at a two dimensional surface arising from collision and binding between the target molecules in solution and receptors coated on the surface.

There is a recent trend to miniaturize the biological sensing systems. The parallelism made through such miniaturization is of great interest. Scaling enables integration of more components and detection sites on the same platform, which increases the throughput of the analysis [9]. Biosensor arrays have been fabricated using silicon nitride, silicon carbide, and glass substrates [5]. The assembly and measurement of biosensors are supported by a top microfluidic layer that could take a variety of forms including fluidic channels or fluidic reservoirs that are filled and emptied by a robotic fluid delivery system. Integration of biosensor interfaces, on-chip electrodes and packaging structures can revolutionize

high throughput drug screening [10] and simultaneous measurement of multiple target concentrations in clinical diagnosis and environmental monitoring [5, 11, 12]. Simultaneous measurement of target molecule concentration also permits onboard calibration to correct for systematic variations that can occur across the array and to correct for electrode-to-electrode variation between different sensors. One consequence of using a biosensor array to measure the target species concentration rather than a single biosensor of comparable area is the improvement in the quality of estimating the response rate [5].

Biosensors can be used for characterization or estimation of any unknown parameter corresponding to the location, emission rate, concentration, or temporal properties of a molecular source.

There are two main approaches for studying the motion and spreading of particles in a fluid; The macroscopic approach is based on the assumption that the fluid can be treated as a continuum. In order that a fluid can be modeled as a continuum, all of its kinematic and transport properties should be continuous. Based on an approximate analysis for liquids, the length scale at which a continuous behaviour is expected is about 10 nm [13]. When the target molecules in a continuous fluid are closely packed relative to the length scale of the flow, rather than treating and tracking individual target molecules, one can describe collections of individual target molecules statistically. This approach yields a concentration field that represents an ensemble average of the stochastic behaviour of individual target molecules. This ensemble average is produced by concentrated solutions. In order to have concentration as a continuous point quantity, the number of target molecules in the experimental window should be large enough to get reasonably stationary statistics [13]. In this case, the concentration field evolves with time and space according to a partial differential equation (PDE) which follows the continuity equation in physics [14]. In a continuum approach, the biochemical interactions between fluid and the biosensor can be described by

differential equations which are determined by reaction rate theory. Continuity assumption is reasonable even at microscopic length scales, when there are many thousands of molecules within the length scale of interest. Continuum approach in liquid flows is the scope of this work where the number of fluid molecules, target molecules, and biosensor molecules are orders of magnitude larger than one thousand in the experimental window. When the continuum assumption fail, for example, when the length scale is much smaller than 10nm in liquid flows, a molecular approach accounts for the dynamics of the flow and biosensors. One of the main molecular fluid techniques which is used primarily for liquid flows is molecular dynamics (MD). The MD technique is a straightforward application of Newton's second law, in which the product of mass and acceleration of each molecule is equated to the forces on the molecule that are computed according to a model, quite often the Lennard-Jones model [13]. The technique begins with a collection of molecules distributed in space with random velocities with Boltzmann distribution. The intermolecular forces at each time step are computed and used to evolve the particles forward in time [15]. Theoretically, MD can be used for all molecular systems including continuous systems. However, the MD technique is highly computationally intensive. The Newton's second law and the Lennard-Jones forces should be computed excessively to evolve the molecules through time. In a continuum fluid, there are billions of molecules, which can take the MD technique years to solve the system. In this thesis, we take a macroscopic approach to the transport of target molecules over biosensors.

Identification of an unknown parameter in a mass-transport and dispersal model involves solving an estimation problem in an infinite dimensional dynamical system, also known as distributed parameter system, which is governed by either a deterministic or stochastic differential equation. Here, we focus on the deterministic transport models where a deterministic PDE describes the dynamics of the concentration field as the average be-

haviour of molecules in a variety of transport phenomena. There are many theoretical and numerical challenges in solving parameter estimation problems in distributed parameter systems, which will be described later in this chapter.

This work is focused on analysis and modeling of biosensor arrays. Dynamical models are developed for analysis of biosensor arrays in advection-diffusion systems. We use our developed models for two main purposes; estimating molecular concentration in a mass-transport system and enhancing molecular detection by improving the geometry of biosensors. We shortly refer to "target molecule" by the term "analyte", which is used in clinical chemistry and refers to the substance that is the subject of an analytical procedure. The recognition event on a biosensor is based on surface capture, which is governed by both chemical reactions on the surface and transport of analytes by advection and diffusion. We illustrate our results in this thesis for two real life biosensors, a protein-based biosensor and a surface plasmon biosensor, whose structures and operations are described in this chapter.

In the next section, we describe the general concepts and underlying challenges towards solving parameter estimation problems in distributed parameter systems. In Section 1.2, we review current literature on estimation problems in mass-transport systems and explain our directions in this work. Section 1.3 explains the physics of the flow of analytes on a reactive biosensor. In order to describe the dynamics of the biosensors and the analyte concentration in a mass-transport system, we need to investigate different binding kinetic conditions on a biosensor surface as a result of interplay between mass-transport and reactions. Section 1.4 outlines the structure and operation of the biosensors for which our results in this thesis are illustrated. We then outline our contributions in this work in Section 1.5.

1.1 Estimation in Distributed Parameter Systems: Basic Concepts

In this section, the problem of parameter estimation in distributed parameter systems (infinite dimensional dynamical systems) is described. The mathematical literature on parameter estimation can be divided into theoretical and numerical work. The predominant part of the theoretical work is devoted to developing concepts of uniqueness of solutions [16] and continuous dependence of the identified parameter on the observed data. These concepts are regarded as parameter identifiability and stability in the literature, which will be briefly explained in this section. The numerical works are concerned with developing efficient algorithms to solve the estimation problem.

In the following, a general parameter identification problem in a distributed parameter system is formulated. An expression of the form

$$L(D^k u(x, t), D^{k-1} u(x, t), \dots, Du(x, t), u(x, t), x, q) = 0, \quad (1.1)$$

for $x \in \Omega \subset \mathbb{R}^n$ can represent a general form of a k -th order PDE with the required boundary condition, where L is a vector function and

$$D^k u(x, t) = \left\{ \frac{\partial^k u(x, t)}{\partial^{\alpha_0} t \partial^{\alpha_1} x_1 \partial^{\alpha_2} x_2 \dots \partial^{\alpha_n} x_n} \mid \sum_{i=0}^n \alpha_i = k \right\}.$$

Here q is the set of parameters in the model, which are fully or partially unknown. The state space model of the form (1.1) describes the dynamics of a physical, biological, etc., process Γ and is obtained by a priori knowledge of the process. We introduce the observation operator C which maps the state trajectory $u(x, t)$ to the observation space M . We can formulate an idealized identification problem, in order to identify the parameter q in the

model, as finding a parameter q^* such that

$$m = Cu(x, t; q^*), \tag{1.2}$$

where m is the measurement of the process Γ . An idealized identification problem has an unrealistic nature because, first, model equations such as (1.1) only approximately describe the process Γ of interest and secondly $m \neq Cu$ due to measurement errors. Considering these circumstances in addition to the fact that we cannot expect to solve (1.2) explicitly even in an error free model, turns our attention to an estimation problem, where we consider parameter estimation problems as optimization problems. We consider the problem of minimizing an error criterion $J(u(\cdot, \cdot; q), m, q)$ subject to u satisfying the dynamics specified in (1.1). There are two types of error criteria: The equation error criterion and the output error criterion. The equation error criterion is only applicable when the entire state can be observed, i.e. where $C = I$. Given the state model (1.1), the equation error criterion is given by

$$J_{eq}(m, q) = \int_0^\tau \int_\Omega [L(D^k m(x, t), D^{k-1} m(x, t), \dots, Dm(x, t), m(x, t), x, q)]^2 dxdt.$$

An advantage of the equation error criterion is that it is essentially quadratic in the parameters if L is linear in q . However, it can be rarely used in practice since it requires observation of the entire space. The output error criterion is given by

$$J_{out}(u, m, q) = |Cu(\cdot, \cdot; q) - m|_M^2, \tag{1.3}$$

which is minimized subject to u satisfying the PDE model (1.1) to obtain q^* . The output error criterion can be used in a wide scope even if only a minimal data set is available. The estimation problem is generally ill-posed as it can be the case where there is no solution

q^* or one may have multiple solutions for q^* [17]. Even if a unique q^* satisfying (1.2) exists, this q^* might not depend continuously on the observations m . Since there are inherent errors in the observation process, the absence of continuous dependence is quite undesirable from a practical point of view. The above mathematical aspects of parameter estimation problems are investigated in theory under the title of parameter identifiability.

There are slight variations in different notions of identifiability [17], although parameter identifiability can be loosely defined as the injectivity of the map from the parameter set to the observation space. Consider the parameter to output mapping

$$\Phi : Q \longrightarrow M,$$

with $\Phi(q) = Cu(q)$, where C is the observation map described in 1.2. Due to the model and measurement errors, the actual observation m does not lie in the output space M . For determination of the best parameter q^* , we use the output least squares method where the output error criterion is minimized;

$$q^* = \arg \min_{q \in Q} |\Phi(q) - m|_M^2.$$

Here, the output least squares method can be divided into two steps; first, finding a projection m_{pr} of the actual observation m onto the space M , and secondly finding a preimage q^* of m_{pr} in Q such that $\Phi(q^*) = m_{pr}$. For the parameter q to be identifiable, it is required to have the uniqueness of the projection of m onto M as well as injectivity of Φ at q^* , i.e. $\Phi(q) = \Phi(q^*)$ for some $q \in Q$ implies $q = q^*$. Parameter identifiability has been widely investigated in literature, where sufficient identifiability conditions are established for various classes of partial differential equations on bounded and unbounded spatial domains (see [18, 19, 20]).

If the unknown parameter in the formalized estimation problem does not depend continuously on the observation data, small perturbations in the data can lead to large deviations in the solution leading to instability of the solution. Solving such problems requires special numerical methods called the regularization methods. Tikhonov regularization, also known as ridge regression in statistics, is the most commonly used method of regularization of ill-posed problems. In this method, a regularization term is added to the output error criterion (1.3) to make the solution stable (For details see [21, 22]).

There are two main approaches to solving parameter estimation problems. Most commonly, a discrete state-space model is used as a result of space discretization of the PDE model. The most common discretization methods include the finite-difference method [23], the finite-element method, modal analysis [24], spline approximations [17] and spectral methods [25]. Dealing with a large order of the state-space system in contrast to a small number of measured states is a disadvantage of these approaches [26]. In the rare cases where the PDE model is analytically tractable, methods with continuous models use analytical solutions to solve the estimation problem.

1.2 Estimation of Molecular Concentration in Advection-Diffusion Systems

In this section, we describe the challenges that exist in solving an estimation problem in mass-transport system using multiple biosensors. We compare our work with current literature on estimation and molecular source identification problems in mass-transport systems.

The physical process of the flow of target molecules is described by an advection-diffusion equation [27]. We avoid turbulence and consider only molecular diffusion in our

model because the Reynolds number is small and viscous forces are dominant.

Using our developed dynamical models, we investigate estimation of target molecule concentration in a fluid flow using an array of surface-based biosensors. This is a highly challenging array signal processing problem due to three non-standard features:

Firstly, measurements can affect the system state through boundary conditions. This is unusual since in most statistical inference problems, observation does not change the system state. Each sensor can affect the measurement of other sensors by grabbing the target molecules.

Secondly, the PDE system is analytically intractable and a discrete state-space model should be used to solve the estimation problem numerically. Conventional discretization methods lead to high-dimensional nonlinear models, which should be solved in several iterations.

Thirdly, the large order of the state-space system in contrast to the small number of measured states can lead to an unidentifiable parameter estimation problem.

Many environmental applications of fluid dynamical models involve state or parameter estimation in an advection-diffusion PDE system (see [17, 28, 29, 30, 31]). Nehorai *et al* [32]-[33] proposed several methods for localization of biochemical point sources, both static and dynamic. In [32], the authors use a maximum likelihood method for localizing a chemical point source in two cases of infinite and closed environments. The solution of diffusion equations with ordinary boundary conditions in both cases are analytically derived. In the close environment, the solution is obtained by interpreting it as a superposition of the actual source and an infinite number of mirror images. The detection problem is a binary hypothesis testing, where the solution is obtained by a modified generalized ratio test. The Cramer-Rao lower bound for the unbiased estimate of parameters is also derived. In [33], a single moving sensor is examined for localization by exploiting spatial and temporal di-

versity in an array of stationary sensors. Since the cases correspond to either conventional boundary conditions or an infinite environment with no boundaries, the solution to the diffusion equation can be derived analytically resulting in low computational complexity and forthright methods. Matthes et al [34] used an analytical solution to the advection-diffusion equation in conjunction with a least-squares approach to estimate the source location. In [35], Bayesian inference is applied to solve a chemical source determination problem, where the posterior joint distribution of location, intensity, and temporal properties of a point source is obtained by a Markov chain Monte Carlo method. The authors develop a dual problem for the advection-diffusion equation using adjoint dispersion equations. The total number of the dual problems that need to be solved is equal to the product of the number of detectors by the number of samples. It apparently requires significantly less amount of computations compared to resolving the main equation for every source term. In this work, a advective flux is assumed on the boundary. Chow et al [36], Kosovic et al [37] and Rapley et al [38] recognized that source reconstruction may be undertaken using a combination of Bayesian inference and MCMC methods but did not implement adjoint dispersion equations for quickly computing source receptor relationships. As a result, their calculations were computationally intensive.

The above works directly use point-wise target molecule concentration values at the sensor location as the measurements to solve the estimation problem. This implies that sensors do not change the state of the system in the above systems whereas in this work, biosensors affect the system state through their measurements by absorbing the target molecules and imposing unconventional boundary conditions on the system. Therefore, the biosensors measurements are not straightforwardly related to the target molecule concentration at the biosensor location. Measurements complicate the estimation problem by affecting the target molecule concentration in the flow and by introducing new state

variables to the system.

1.3 Diffusion, Advection and Reaction on Surface-Based Biosensors

As well as estimating molecular concentration, the developed dynamical models in this work are utilized for improving detection of low molecular concentrations. We investigate how a biosensor array, compared to a single biosensor, can improve detection of low molecular concentrations. We take a physical approach based on the analysis of advection-diffusion models on surface-based biosensors to show how an array of multiple biosensors can enhance target molecular detection. Next section provides the literature for understanding the physics of mass-transport and reaction on a biosensor surface. This section describes different binding kinetics and mass-transport conditions in the transport of molecules over a reactive biosensor surface. In Section 1.3.1 different binding kinetic regimes are introduced, which classify the operation region of the sensor based on the interactions of mass-transport and reactions on the sensor. Section 1.3.2 explores the effect of different conditions of advection and diffusion (mass-transport conditions) on the concentration flow profile and the diffusion rate of target molecules on the sensor surface.

1.3.1 Mass-Transport and Reaction Interplay

We describe the effect of mass-transport (advection and diffusion) and reaction through a paradigmatic model in Fig.1.1. The solution containing target molecules with concentration A^* flows, with volumetric flow rate Q , through a channel of height h and width w_c . A biosensor of width w_s is embedded in the channel floor. The biosensor length along the flow direction is L . The binding site concentration on the biosensor is θ per unit area.

Different binding kinetic regimes compare the effects of mass-transport and reaction rate on binding kinetics. When the transport rate of analytes to the surface by advection and diffusion is much slower than the intrinsic reaction rates on the surface, the analytes binding rate is mass-transport limited. In this regime, once a molecule is transported to the surface, it binds to the binding sites instantaneously. The binding kinetic regime is determined by the dimensionless Damkohler number D_a which is the ratio of the reaction-rate limit to the transport (diffusive) limit on the analyte binding rate [1, 39]. In the system of Fig.1.1, the Damkohler number D_a is defined as

$$D_a = \frac{Lk_{on}A^*\theta w_s}{J_d}, \quad (1.4)$$

where L is the length of the sensor, k_{on} is the forward reaction rate, θ is the total binding site concentration, and J_d is the initial diffusive flux, which will be computed later in this chapter under different mass-transport conditions. When D_a is sufficiently large, the kinetics are mass-transport influenced and they become mass-transport limited when $D_a \gg 1$. When $D_a \ll 1$, the reactive flux is much smaller than the diffusive flux and the binding kinetics are reaction-limited [39].

1.3.2 Mass-Transport Phase Diagram

The binding kinetics regime indicates the extent of mass-transport effect on the binding rate of analytes by comparing the initial reactive flux and the diffusive flux J_d in (1.4). The diffusive flux J_d is the rate at which mass-transport brings analytes to the biosensor surface in Fig.1.1 and depends on the concentration profile in the flow chamber. In this section, we will describe how the flux J_d is computed in the flow chamber of Fig.1.1. In the model system of Fig.1.1, the fluid flow is laminar with a parabolic fully-developed velocity profile $v(z)$ defined by

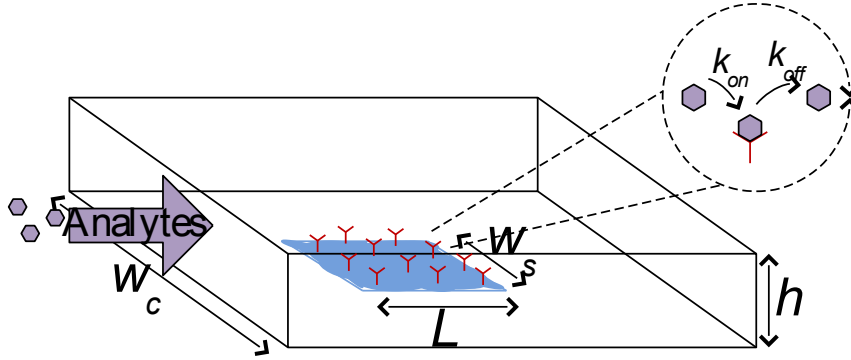


Figure 1.1: Solution with target molecule (analyte) concentration A^* flows with volumetric flow rate Q through a flow chamber of height h and width w_c over a biosensor of length L and width w_s . The biosensor is functioning with θ receptors per unit area. The kinetic rate constants for the first-order binding reaction are k_{on} and k_{off} . The analyte diffusion constant is γ . The dimensionless Damkohler and Péclet numbers are obtained by (1.4) and (1.6).

$$v(z) = \frac{6Q}{w_c h^2} z \left(1 - \frac{z}{h}\right), \quad (1.5)$$

at the height z above the biosensor. Here, Q is the total volumetric flow rate in the flow chamber. The concentration profile and the transport rate of analytes to the surface, in a advective flow is determined by the values of the dimensionless Péclet number and the dimensionless length of the biosensor defined as $\lambda = \frac{L}{h}$ [1]. The Péclet number is defined as the ratio of the time it takes the analyte to diffuse across the channel to the time it is swept away the same distance by advection [1];

$$P_{eH} = \frac{Q}{\gamma w_c}, \quad (1.6)$$

where γ is the analyte diffusion constant, Q is the volumetric flow rate as described in (1.5), and w_c is the width of the flow chamber. Consider the biosensor as an infinite sink, where analytes bind immediately upon encountering the biosensor surface. In other words, the biosensor is operating in a transport-limited regime, where the Damkohler

number is infinite. This causes formation of a depletion region above the biosensor, where the analyte concentration on the biosensor surface remains zero. When the transport of analytes in the flow chamber is purely diffusive, the depleted region grows infinitely with the thickness $\delta = \sqrt{\gamma t}$ along the flow chamber [1]. When advection is added and the flow velocity is too small, the depletion region still expands along the flow chamber, i.e. $\delta \gg h$, until advection halts its growth when the diffusive flux $J_d = \frac{\gamma A^* w_c h}{\delta}$ balances the advective flux QA^* . This equilibrium gives the thickness of the depletion region as $\delta = \frac{hw_c\gamma}{Q} = \frac{h}{P_{eH}}$. The initial assumption that the depletion region is extended along the channel requires that $\delta \gg h$ or equivalently $P_{eH} \ll 1$. When the Péclet number is too large $P_{eH} \gg 1$, the diffusion on the biosensor surface cannot keep up with the input advective flux. The concentration profile changes and a thin boundary layer forms above the biosensor. Figure 1.2 shows a phase diagram [1], where mass-transport conditions are categorized into different regions based on the values of the Péclet number P_{eH} and the sensor dimensionless length λ . In each region, the thickness of the depletion region and the mass-transport limit on the analyte collection rate has a different formulation in terms of λ and P_{eH} . Region (i) in the diagram corresponds to the full collection regime, where the analyte collection rate on the sensor is equal to the input advective flux. The focus of this thesis is on region (ii) where $P_{eH} \gg \lambda$ and $P_{eH} \gg 1/\lambda^2$. In this region, the mass-transport limit J_d on the steady-state binding rate on the biosensor surface is equal to [1, 40]

$$J_d = A^* w_s \gamma F, \quad F \approx 1.47 P_{eH}^{1/3} \lambda^{2/3}. \quad (1.7)$$

In the computation of (1.7), it is assumed that the biosensor has infinite capacity and analyte instantaneously binds to the binding sites once it encounters the surface. This implies that the analyte concentration on the surface remains zero during the experiment.

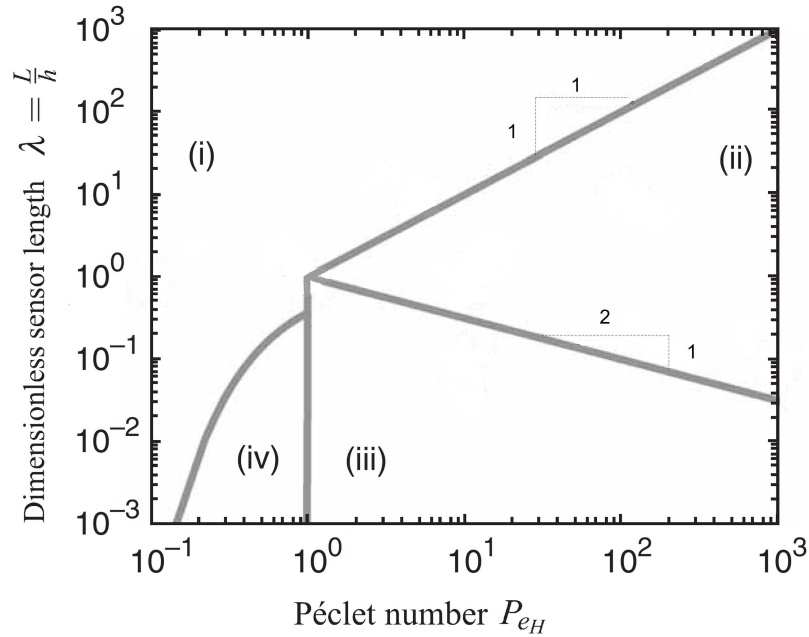


Figure 1.2: A typical mass-transport phase diagram for the binding kinetics of a biosensor [1]: Region (i) corresponds to full collection regimes, where the analyte binding rate on the biosensor is equal to the input advective flux. In region (ii), the depletion region on the biosensor surface is thin compared to both the height of the flow chamber and the biosensor length. In this region, the mass-transport limited analyte binding rate, at the steady state, is obtained by (1.7). The depletion region in region (iii) is much thinner than the height of the flow chamber but comparable to the biosensor length itself. The mass-transport limited analyte binding rate, in this region, is computed by Ackerberg et al [2]. Region (iv) has not, to our knowledge, been studied thus far.

However, in practice the reaction rates are finite and the analyte concentration near the biosensor surface increases with time resulting in slower analyte diffusion rate towards the biosensor. The corresponding analysis relates directly to the two-compartment model widely used in modeling a variety of binding experiments [41, 42, 43, 44], which is described in the next chapter. When the binding kinetics are reaction-limited, the entire flow chamber achieves equilibrium at the constant concentration A^* very quickly and there is no depletion region.

1.4 Two Case-studies

In this section, the structure and operation of two types of biosensors, a protein-based biosensor, namely the ion channel switch (ICS) biosensor and a surface plasmon resonance biosensor are described. We use these biosensors to illustrate our results in practice.

1.4.1 Ion Channel Switch Biosensor

Ion channel switch (ICS) biosensor was originally developed by Cornell et al [3]. It is a generic biosensor that can detect low molecular weight drugs, large proteins and micro-organisms [5, 45] with concentrations as low as 1 pM [3, 46, 47].

Biological ion channels are water-filled sub-nanosized pores formed by protein molecules in the membranes of all living cells [48, 49]. They play a crucial role in living organisms by selectively regulating the flow of ions in and out of a cell thereby controlling the cell's electrical and biochemical activities. ICS biosensor is a surface-based biosensor, which incorporates artificial ion channels built out of Gramicidin A peptides in a synthetic lipid bilayer. The conductance of the ion channels is switched by the analyte recognition event. The inner lipid layer is tethered to a gold substrate. The ion channels within this layer are tethered whereas the ones in the outer layer diffuse freely. Applying a small alternative potential between the gold substrate and a reference electrode in the test solution, as shown in Figure 1.3, generates a charge at the gold surface. The flow of ions through a channel occurs when a mobile channel in the outer layer aligns to a fixed channel in the inner layer to form a conducting dimer. Therefore, the conductance of the biosensor is proportional to the number of conducting dimers. The arrival of target molecule cross-links antibodies attached to the mobile outer layer channels, to those attached to tethered lipids. This anchors the channels distant, on average, from their inner layer partners as shown in Figure 1.3. The expected number of dimers is thus decreased which results in

the reduction of the conductance of the biosensor. Reduction in the electric current in the external circuit indicates analyte recognition. The time variations of the biosensor conductance can be recorded as the biosensor response. Fig.1.4 shows a clinical prototype of ICS biosensor embedded in a digital impedance reader device.

The ICS biosensor provides an interesting example of engineering at the nano-scale. It is significant that the functionality of the device depends on approximately 100 lipids, and a single ion channel modulating the flow of billions of ions in a typical sensing event of approximately 5 minutes. Since the gramicidin channels (each with conducting pore of diameter 0.4 nm and length 2.8 nm) move randomly in the outer lipid leaflet of the membrane (1.4 nm thick), we can view the biosensor as a fully functioning nano-machine with moving parts . Indeed, each individual gramicidin channel diffuses randomly over an area of order $1 \mu\text{m}^2$. Furthermore, the 4 nm thick lipid bilayer is tethered 4 nm away from the gold surface by hydrophylic spacers thereby allowing ions to diffuse between the membrane and gold. This permits a flux in excess of 10^6 ions per second to traverse each channel [5].

The fabrication of the ICS biosensor has several interesting properties that make it an appealing case study. The ICS biosensor incorporates a self assembled monolayer providing enhanced stability. The tethered bilayer permits two-dimensional diffusion of gramicidin channels which provides a remarkable gating mechanism. Since gramicidin has a terminal ethanolamine group which permits a range of chemistries, the biosensor may be prepared for use with a wide range of receptors to detect many different analytes. The ICS sensing mechanism does not require washing (unlike an ELISA assay), provides large transduction amplification (millions of ions for every channel dimerization) and a high detection sensitivity since a single channel can diffuse and identify analyte molecules bound to many capture sites [5].

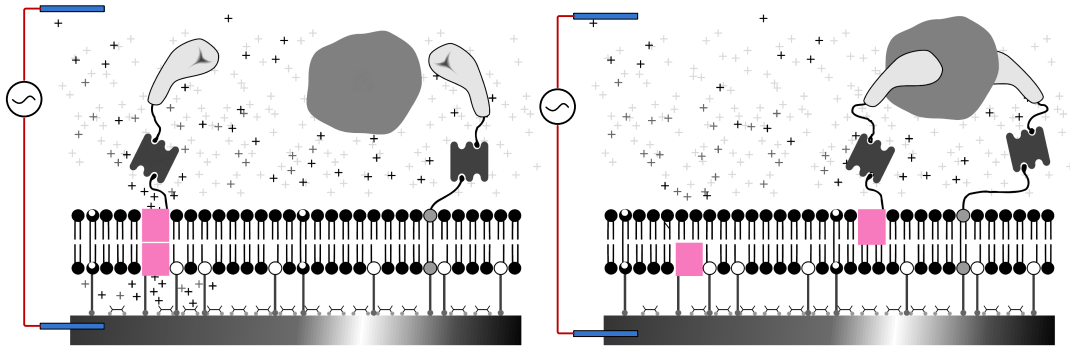


Figure 1.3: Example: Ion Channel Switch Biosensor [3]. When analyte binds to the antibodies, the conducting dimer is split into non-conducting channels.

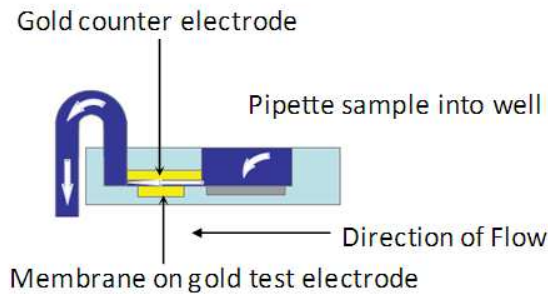


Figure 1.4: An Ion Channel Switch (ICS) biosensor embedded in an impedance meter device.

The resistance of the ICS biosensor, when no analyte is present, is approximately $60\text{k}\Omega$. This can be reconciled with the $10^{11}\Omega$ per channel resistance of gramicidin A as follows. Since there are 10^8 gramicidin channels per cm^2 , each electrode of area 0.03cm^2 contains approximately 3×10^6 channels with approximately half of them dimerized. So the effective resistance of all the dimerized ion channels (which act as parallel resistors) is approximately $60\text{k}\Omega$. The measured current is the average effect of the formation and disassociation of thousands of dimers and is approximately continuous-valued [45]. More details on the construction and operation of this biosensor can be found in [5, 45].

1.4.2 BIACORE: A Surface Plasmon Resonance Biosensor

Surface plasmon resonance (SPR) is a phenomenon that occurs during optical illumination of a metal surface and it can be harnessed for biomolecular interaction analysis [50]. It is best described as a charge density oscillation at the interface between two media with oppositely charged dielectric constants. A surface plasmon can be excited by light as demonstrated in Fig.1.5. Experimentally, resonance is achieved either by varying the incident light wavelength at a fixed angle at or above the critical angle or alternatively by varying the angle at a fixed wavelength [4]. At the surface plasmon resonance angle, the photon energy and momentum of the incident optical field coincide with the charge density wave along the metal-dielectric interface [51]. The photon energy is then transferred to the charge density wave. This phenomenon can be observed as a concomitant decrease or a sharp attenuation in the reflected light intensity as shown in Fig.1.5. Interaction of contaminant material (e.g. bacterial cell or toxin) with specific antibody immobilised on the surface results in a change in mass at the surface, which in turn causes a change in refractive index. This correspondingly alters the resonance state and is recorded as a shift in the angular position of the reflectance minimum (I to II, Fig.1.5) [4]. Surface plasmon resonance occurs in the visible region in so-called free electron-like metals such as silver and gold. Furthermore, the thickness of the metal film should be a fraction of the wavelength.

The pioneers of commercial SPR-based biosensing were Pharmacia BiosensorAB, now BIAcoreAB, who launched in 1990 the original BIAcore system, the world's first SPR-based analytical instrument for studying biomolecular interactions [4]. This was one of the first commercial SPR biosensing devices widely used to investigate the kinetics of a variety of molecular interactions [52, 53, 54]. Unlike ICS biosensor, where analyte binding initiates several chemical reactions on the surface, in the BIACORE system, a single chemical reaction occurs between the analyte and the immobilized reactant on the sensor

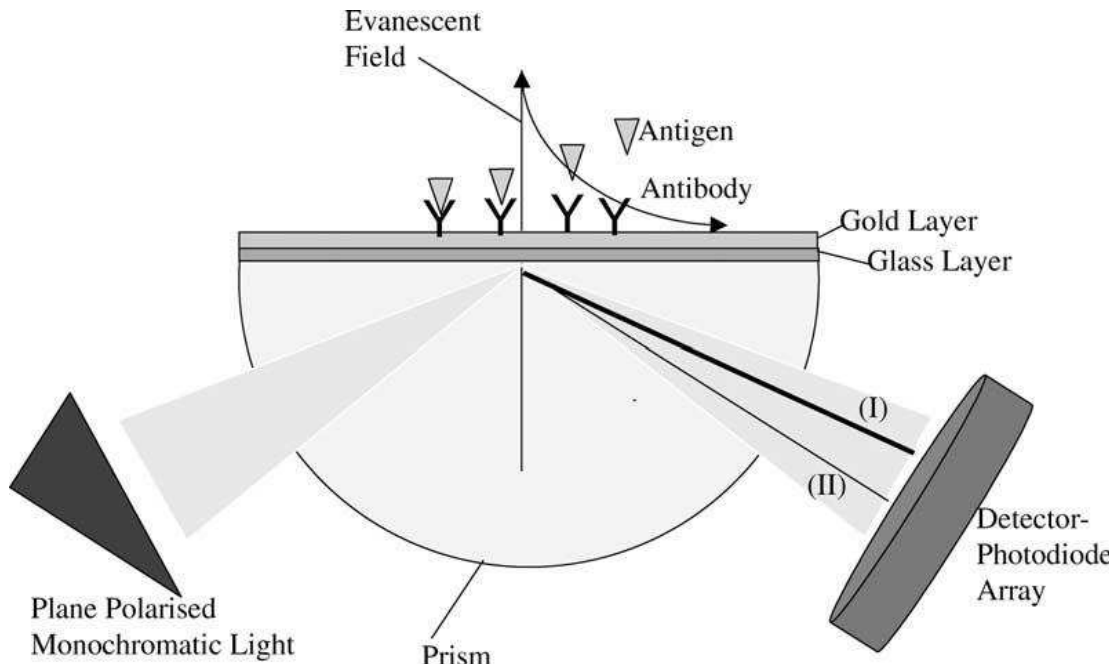


Figure 1.5: Diagrammatic illustration of the surface plasmon resonance principle [4]

chip. As mentioned, analyte detection is based on the SPR phenomenon, where a shift in the angular position of the reflectance minimum is caused by the change in mass due to analyte binding [55, 56].

1.5 Contributions and Results

This thesis is focused on modeling and analysis of surface-based biosensor arrays for detection of target molecules. We consider the applications where "concentration" as a macroscopic variable can describe the dynamics of target molecules in the fluid. Current research on modeling of biosensors is mainly focused on modeling and analysis of a single biosensor [1, 41]. We develop a white box PDE model for the dynamics of a biosensor array. We then develop an approximate model which is used for estimation of molecular concentration. The estimation problem is different from its relevant estimation problems in current

literature since it considers measurement effects on the system. We also take a novel approach in discretizing the system for solving the estimation problem. The approximation method is based on the two-compartment model used in the analysis of mass-transport influenced binding experiments [1]. The approximate model yields an ODE system with the number of states much less than that obtained by conventional discretization methods mentioned in Section 1.2. We use a nonlinear least squares method for solving the problem. The variations of estimation bias and variance versus the number of biosensors are investigated by deriving analytic expressions.

The Reynolds number is very small, on the order of 10^{-4} and viscous forces are much stronger than inertial forces. Therefore, the flow is laminar and in the absence of turbulence, advection-diffusion equation governs the variations of target molecule concentration. The diffusion constant for biomolecules in aqueous solutions ranges from 10^{-11} to 10^{-9} m^2/s [57]. For flow rates in the order of $\mu\text{L}/\text{min}$ and flow chamber dimensions less than few millimetres, the Péclet number is large. Based on our case-studies, we consider the biosensors that are operating in region (ii) of the mass-transport phase diagram in Fig.1.2 which spans a wide range of applications in binding experiments. We consider the most general binding kinetics regime which is the mass-transport influenced regime.

After solving the estimation problem, we investigate distributed placement of sensing surfaces for improving analyte detection by using an array of small biosensors instead of a single biosensor of the same total sensing area. Then, the size of the biosensors in the array is optimized using our approximate ODE model to achieve maximum response rate. Our contributions in this thesis are organized as follows:

1. In Chapter 2, an advection-diffusion PDE model is constructed for modeling concentration variations of target molecules that flow past a linear array of biosensors. To facilitate estimation of the target molecule concentration, a multi-compartment

approximation method is developed to describe the dynamics of the problem by a system of ODEs. The ICS biosensor, described in Section 1.4, is used as an actual example to illustrate our results. The PDE and ODE models for this biosensor are specified and solved numerically. We show how the PDE model and ODE approximations can satisfactorily model this novel biosensor.

2. In Chapter 3, We use the measurements of a biosensor array to estimate the injection analyte concentration in a flow chamber. In this configuration, biosensors are implanted on separate substrates connected to different electrodes. The estimation of analyte concentration is posed as a parameter estimation problem in the derived ODE model of Chapter 2. The estimate is computed numerically for the ICS biosensor array via the nonlinear least squares method. The finite-sample variance and bias of the estimator is approximated by deriving analytic expressions. The attainable improvement in the estimate based on the number of biosensors is evaluated using the results from the ODE model and the derived expressions. One of the main results is that the measurements from N biosensors can yield a smaller estimation variance compared to the estimate obtained by N independent measurements. The work in Chapter 2 and Chapter 3 is published in [58, 59, 60].
3. Chapter 4 addresses the problem of detecting minute concentrations (nano to picomolar) of analyte in a fluid flow chamber using an array of surface-based sensors. It is shown that in the mass-transport influenced case, when the Damkohler number D_a defined in (1.4) is not too small, substantial improvements in the response rate can be obtained from an array of spaced small sensing surfaces relative to a single large sensor. The measurements of individual sensors in the array are combined to form a single output signal for measurement. Formulas are derived for quantifying the improvement in the detection performance. Also, the size of the sensors is

optimized to achieve the maximum detection response. The results of the model are compared with experimental data obtained for the ICS biosensor and a surface plasmon resonance biosensor. The work in this chapter is published in [61].

4. We construct a mathematical proof for the two-compartment model. The proof provides an upper bound for the modeling error in the approximation of the immobilized species concentration. This approximation error is important because eventually modeling the dynamics of these species is our goal in the analysis of the biosensor response.

1.6 Thesis Organization

In Chapter 2, the PDE model for the dynamics of the flow of target molecules over an array of biosensors is described. We then derive the multi-compartment ODE model for solving the concentration estimation problem. To illustrate the accuracy of the derived model, the PDE model and multi-compartment model are compared numerically for an array of ICS biosensors. Using the derived model, the least squares estimate of the target molecule concentration is obtained in Chapter 3. The properties of the finite-sample estimator is analyzed by deriving analytic expressions for the variance and bias of the estimate. Then, the example of ICS biosensor array, given in Chapter 2, is used again to illustrate our estimation results. Based on the analysis of Section 1.3.1 and Section 1.3.2, a formula is derived for characterizing the improvement of multiple biosensors compared to a single biosensor of the same total sensing area in Chapter 4. Using the formula, the size of individual biosensors in the array is optimized to achieve maximum analyte collection rate. To validate our predictions, numerical studies and experimental data are compared. The results for two case-studies, an ICS biosensor and a surface plasmon resonance biosensor, are provided. In

Chapter 5, a detailed mathematical model is constructed for the two-compartment model. Finally, Chapter 6 contains discussions of the main results, conclusions, and proposals of future research directions.

Chapter 2

Multi-Compartment ODE model:

Analysis

Current work on modeling and analysis of biosensors mainly focus on a single biosensor whereas, in this thesis, we develop models to describe the dynamics of an array of biosensors. To our best knowledge, analysis of biosensor arrays in current literature is limited to reaction-limited regimes where depletion regions are small and biosensor effects on concentration are negligible. However, our developed models in this work are not limited to any kinetics regime and are applicable to both reaction limited and mass-transport limited regimes. We first construct a PDE model to describe the system dynamics. Then, we propose a method based on the two-compartment approximation [62] in order to convert the PDE to a lumped-parameter system of ODEs. The two-compartment model is used in modeling a variety of binding experiments, influenced by diffusion and mass transport, to study and characterize the kinetic properties of biomolecular interactions in a single biosensor [42, 55]. By developing the existing two-compartment model, a new multi-compartment model is derived to describe the dynamics of a linear array of multiple biosensors in a flow chamber. In this model, the PDE model is approximated by a system of ordinary differential equations. We use the developed multi-compartment model for parameter estimation in Chapter 3 and improving biosensor response rate in Chapter 4. Fig.2.1 presents the main contributions of this chapter which are stated as follows:

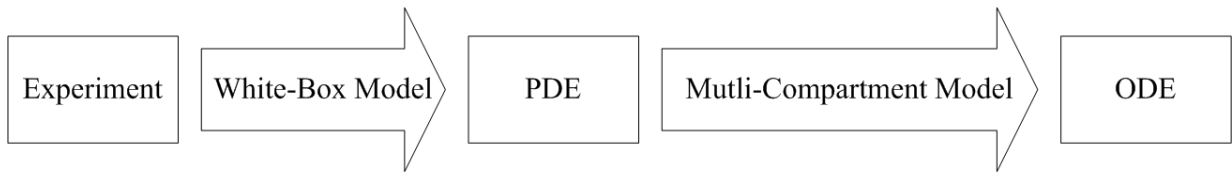


Figure 2.1: The physical dynamics is first described by a PDE model, which is converted to a multi-compartment ODE model for further analysis.

1. An advection-diffusion PDE model is constructed to model the variations of the concentration of analytes that flow past a linear array of biosensors. This model is based on a similar PDE model, which accurately describes the dynamics of a single biosensor [63]. To facilitate estimation of the analyte concentration, an approximation method is developed to describe the dynamics of the problem by a system of ordinary differential equations (ODEs). The proposed multi-compartment ODE model is derived by exploiting the multiple-scale behaviour of the system, together with the divergence theorem.
2. The ICS biosensor is used as an actual example to illustrate our results. The PDE model for this biosensor is specified and solved numerically using the Comsol multi-physics finite element analysis software. We show how the PDE model and ODE approximations can satisfactorily model this novel biosensor.

The use of the multi-compartment model in the analysis of biosensor arrays has the following advantages:

- (a) The model provides an insight to the behaviour of the system, which is significantly useful for designing and optimizing the parameters.
- (b) Not only is the multi-compartment ODE model an insightful model, but it can also be used in estimating unknown quantities by converting the infinite-dimensional system to a finite-dimensional one. In the conventional discretiza-

tion techniques for solving estimation problems in PDEs such as the finite-difference method and the finite-element method, the number of derived ODEs is larger compared to the derived multi-compartment model. In our given example in this chapter, the number of ODEs in the finite element solver is of the order 1000. On the other hand, in the multi-compartment approximation, the PDE equation inside the domain is converted to exactly N ODEs where N is the number of biosensors. Still, it is shown in Section 2.3 that the model yields an excellent approximation.

- (c) More importantly, with the aid of this model, the variance and bias of the estimator are evaluated. This model allows us to explain the variations of estimation variance with the number of biosensors. The variations of the estimation bias can be explained using the derived analytic expression.

The organization of this chapter is as follows: In Section 2.1, the PDE model for the flow of analytes over a biosensor array is described. The PDE model can be generally used for any type of reactive surface other than biosensors. Then, the multi-compartment ODE model is derived in Section 2.2. Section 2.3 presents the estimation results for an example of ICS biosensors introduced in Chapter 1.

2.1 PDE Model for Analyte Flow Over a Biosensor Array

The aim of this section is to estimate the analyte concentration in a flow system where the dynamics are described by an advection-diffusion PDE model. Consider a flow chamber with a rectangular cross section where analytes flow past multiple surface-based biosensors. There are N identical biosensors forming a linear array along the flow direction on the

chamber floor. We introduce three-dimensional Cartesian coordinates (x, y, z) with the x -axis along the flow direction and the z -axis along the height of the flow chamber and perpendicular to the surface of the biosensors as shown in Fig.2.2 for $N = 3$. Biosensor i , for $i \in \{1, \dots, N\}$, is located in the range $[x_{i,1}, x_{i,2}]$ along the x -axis and $[0, w]$ along the y -axis. In this system, the flow chamber and the biosensors have the same width w ($w_c = w_s = w$). The inlet of the flow chamber lies in the $y - z$ plane. The system is symmetric about the y -axis since the ratio of the height to the width of the flow chamber is selected to be less than $1/20$ [64]. The dimensions of the flow chamber and biosensors are:

$$\text{Flow chamber: Height} = h, \quad \text{Length} = l \quad \text{Width} = w, \quad (2.1)$$

$$\text{Biosensors: Length} = L, \quad \text{Width} = w, \quad \text{Spacing} = d,$$

$$\text{Biosensor } i \text{ is located at } x \in [x_{i,1}, x_{i,2}] \text{ and } y \in [0, w].$$

When analytes in the solution arrive at the biosensors, chemical reactions are initiated resulting in a change in impedance that is translated to a change in the measured current.

Below, an advection-diffusion PDE is used to describe the spatio-temporal evolution of analyte concentration in the flow chamber. It is coupled with a set of ODEs on the boundary, which describes the adsorption of analytes on the biosensors as a result of chemical reactions.

Fluid flow dynamics: The analyte concentration in the flow chamber (2.1), denoted by $A(t, x, z)$ is governed by an advection-diffusion PDE [45]

$$\frac{\partial A}{\partial t} = \gamma \left(\frac{\partial^2 A}{\partial x^2} + \frac{\partial^2 A}{\partial z^2} \right) - v(z) \frac{\partial A}{\partial x}, \quad x \in (0, l), \quad z \in (0, h). \quad (2.2)$$

Here γ is the diffusion constant of the analyte and $v(z)$ is the flow velocity in x direction

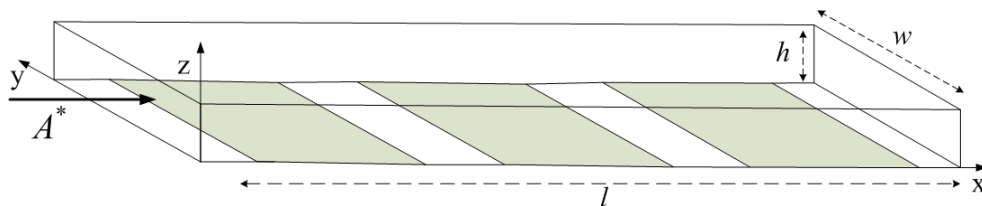


Figure 2.2: An equally spaced linear array of three biosensors in a rectangular flow chamber. The fluid containing target molecules (analytes) enters from the left side. The analyte concentration at the inlet of the flow chamber is A^* as expressed in the boundary condition (2.4).

with total volumetric flow rate Q . The Reynold number is small and the flow is laminar due to the small cross-section area of the flow chamber. In our experimental examples, the Reynold number is of the order of 10^{-4} . Since viscous forces are strongly dominating inertial forces, surface roughness such as biosensor edges cannot cause turbulence in the system. The flow is fully developed with a parabolic velocity profile $v(z)$, defined by (1.5) in Section 1. Here, w_c is replaced by w . The parabolic velocity profile requires the assumptions that the edges of the biosensors are sufficiently far from the entry and exit ports and also small ratio of the height to the width of the flow chamber [14]. Initially, the flow chamber is empty and the concentration inside the flow chamber is zero. So the initial condition is written as

$$A(0, x, z) = 0, \quad x \in (0, l), \quad z \in (0, h). \quad (2.3)$$

The boundary conditions for PDE (2.2) are specified as follows: The concentration at the inlet of the flow chamber is constant during the estimation process and equal to A^* . At the outlet of the flow chamber, it is assumed that the exit of analytes is due entirely to the flow [55]. Therefore, there is no diffusive flux at the outlet of the flow chamber. There is insulated boundary condition at $z = h$ since no molecules can travel across the boundary. The gaps between the biosensors on the chamber floor, at $z = 0$, are also insulated. These

boundary conditions are described as

$$\begin{aligned}
 A(t, 0, z) = A^*, \quad \frac{\partial A}{\partial x}(t, l, z) = 0, \quad \frac{\partial A}{\partial z}(t, x, h) = 0, \\
 \frac{\partial A}{\partial z}(t, x, 0) = 0, \quad x \notin \cup_{i=1}^N [x_{i,1}, x_{i,2}].
 \end{aligned}
 \tag{2.4}$$

Chemical dynamics: On the surface of each biosensor, the diffusive flux of analytes is equal to the rate of consuming analytes by the reactions [45]. This statement is translated into the following boundary condition on biosensor i for $i \in \{1, 2, \dots, N\}$. According to (2.1), it can be expressed that

$$\gamma \frac{\partial A}{\partial z}(t, x, 0) = \mathbb{R}(A(t, x, 0), \mathbf{u}_i(t, x)), \quad x \in [x_{i,1}, x_{i,2}],
 \tag{2.5}$$

where the vector $\mathbf{u}_i(t, x)$ contains the concentration values of the immobilized species on biosensor i at time t and location x . $\mathbb{R}(A, \mathbf{u}_i)$ is the rate at which the chemical reactions consume analytes per unit area on the biosensor surface. This rate depends on the concentration of analytes and immobilized species on the biosensor.

The order of A and \mathbf{u}_i in the consumption rate $R(A, \mathbf{u}_i)$ depends on the type of the recognition mechanism. Biosensors function based on either a biocatalytic or a bioaffinity recognition mechanism [65]. In the former, the recognition mechanism is based on a reaction catalysed by macromolecules. The glucose biosensor is an example. Biocatalytic reaction rates are often chosen to be first order dependent on the target molecule concentration [65]. The biosensors with bioaffinity recognition mechanism are based on the interaction of target molecule with macromolecules. Protein receptor and antigen-antibody based biosensors such as ion channel-based biosensors [3] and surface plasmon resonance biosensors [4] fit into this category. Binding and dissociation kinetics on this type of biosensors can be modeled using first order reactions [66]. When the target molecule is a first

order reactant on the biosensor, the rate $\mathbb{R}(A, \mathbf{u}_i)$ can be expressed as [67]

$$\mathbb{R}(A, \mathbf{u}_i) = AR_f(\mathbf{u}_i) - R_b(\mathbf{u}_i), \quad (2.6)$$

where $R_f(\cdot)$ and $R_b(\cdot)$ are functions which are specified by the rate law of reactions on the biosensor. Here, $AR_f(\mathbf{u}_i)$ and $R_b(\mathbf{u}_i)$ respectively refer to the association and dissociation rate of target molecules. The association rate $AR_f(\mathbf{u}_i)$ is linear in the analyte concentration A on the biosensor surface. The dynamics of the immobilized species of biosensor i at location $x \in [x_{i,1}, x_{i,2}]$ are described by a system of ODEs as [68, 69]

$$\frac{d\mathbf{u}_i(t, x)}{dt} = \mathbb{F}(\mathbf{u}_i(t, x), A(t, x, 0)), \quad \mathbf{u}_i(0, x) = \mathbf{u}_0. \quad (2.7)$$

Here, $\mathbb{F}(\cdot)$ is a vector function whose elements describe the dynamics of the concentration $\mathbf{u}_i(t, x)$ of immobilized species on the biosensor, in terms of the elements of $\mathbf{u}_i(t, x)$ and the target molecule concentration $A(t, x, 0)$ at the surface of the biosensor. It is determined by the rate law of reactions on the biosensor. The constant \mathbf{u}_0 is the initial concentration of immobilized species on each biosensor.

Aim: The aim is to estimate the concentration A^* at the inlet of the flow chamber, which appears in the boundary conditions (2.4). After describing the biosensor array model, statistical estimation algorithms are given in Section 2.2 and Section 3.2 to estimate A^* , given noisy measurements from the biosensors.

Measurement equation: Finally, the measurement equation is specified. The biosensor translates the changes in the concentration quantities \mathbf{u}_i , on biosensor i , to a corresponding electrical signal denoted by $g_i(A^*, t)$. The notation emphasizes on the fact that the response is an implicit function of the concentration A^* at the inlet of the flow chamber.

The response $g_i(A^*, t)$ of biosensor i can be written as

$$g_i(A^*, t) = G(\bar{\mathbf{u}}_i(t)), \quad \bar{\mathbf{u}}_i(t) = \frac{\int_{x_{i,1}}^{x_{i,2}} \mathbf{u}_i(t, x) dx}{x_{i,2} - x_{i,1}}. \quad (2.8)$$

Here, $G(\cdot)$ is the transducer function and $\bar{\mathbf{u}}_i(t)$ denotes the surface average of the concentration vector $\mathbf{u}_i(t, x)$. In Section 2.3, we give a specific example of an actual biosensor where $G(\cdot)$ models the conductance of the biosensor. For biosensor i , the measurement sampling points are denoted by $t_{i,k}$ for $k \in \{1, \dots, S\}$. It is a general notation that allows independent selection of sampling time points for different biosensors. Considering the PDE model (2.2)-(2.7), the measurement taken at biosensor i at time $t_{i,k}$, denoted by $m_{i,k}$, is

$$m_{i,k} = g_{i,k}(A^*) + n_{i,k}, \quad i \in \{1, \dots, N\}, \quad k \in \{1, \dots, S\}, \quad (2.9)$$

where $n_{i,k}$ is the corresponding measurement noise and $g_{i,k}(A^*)$ refers to the response $g_i(A^*, t)$ at time $t = t_{i,k}$. In (2.9), S is the number of measurement samples taken at each biosensor. The noise samples $n_{i,k}$ for $i \in \{1, \dots, N\}$ and $k \in \{1, \dots, S\}$ are independent normally distributed with zero mean and finite variance σ^2 . Here, $n_{i,k}$ captures the measurement noise in the measurement circuit, which is widely assumed to have normal distribution.

2.2 Multi-Compartment Model Approximation

Given the measurement equation (2.9) and the PDE model of Section 2.1 defined by (2.2)-(2.7), the aim is to estimate the concentration A^* at the boundary in (2.4). The PDE is coupled with a set of ODEs through the boundary conditions (2.5) and is highly unlikely to be analytically tractable. Asymptotic analysis of the advection-diffusion equation on a single flat plate in current literature [1, 40, 70, 71] endorses this statement. Even when the

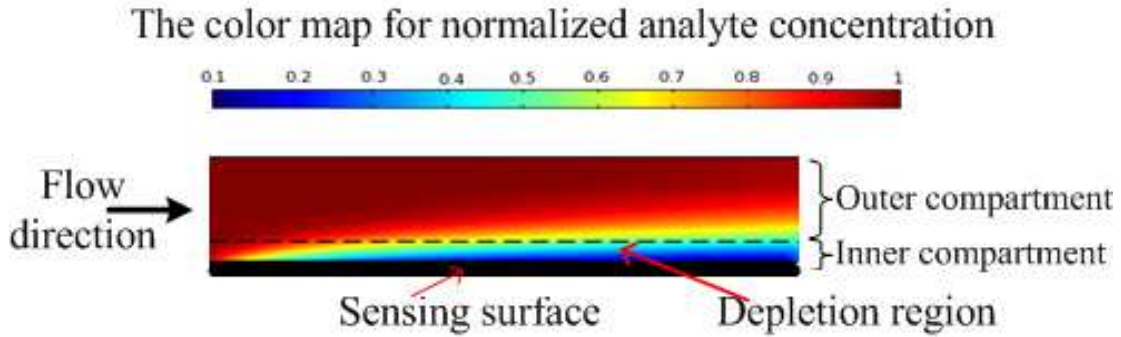


Figure 2.3: Formation of a depletion region above the biosensor surface in the flow chamber: The two-compartment model can describe the dynamics of the system in this flow profile. The analyte concentration in the outer compartment is constant, equal to the concentration at the inlet whereas the concentration in the depletion inner compartment is slowly varying.

target molecule concentration is constant in the flow chamber, reactions on the biosensor, which are described by a set of nonlinear ordinary differential equations (ODEs), cannot be solved analytically [67]. Reaction-diffusion problems have been widely solved numerically [41, 42, 68, 72]. To estimate A^* in (2.4), a multi-compartment ODE model is introduced that approximates the PDE by a system of ODEs. The introduced model is an extension of the existing two-compartment model [55] and is derived based on the multi-scale behaviour of the system and applying the divergence theorem. After reviewing the two-compartment model in Section 2.2.1, the multi-compartment model is derived.

2.2.1 Review of the Two-Compartment Model

Consider a flow of molecular species over a single surface-based biosensor, as shown in Fig.2.3, where the molecules wander through solution and bind to the receptors immediately upon encountering the surface. As discussed in Chapter 1, in a mass-transport influenced regime, a depletion region forms above the biosensor surface. We consider the case where the time it takes the sensor to achieve equilibrium is much greater than the time for the depletion region to form. In this case, the concentration profile achieves a

quasi-steady state [1]. As described in Chapter 1, the thickness of the depletion region and the flow concentration profile are determined by the values of two dimensionless parameters in the system; the Péclet number and the dimensionless ratio $\lambda = L/h$, where L and h are respectively the biosensor length and the height of the flow chamber [1]. In region (ii) of the mass-transport phase diagram in Fig.1.2, when the Péclet number is sufficiently large, i.e. $P_{eH} \gg \lambda$ and $P_{eH} \gg 1/\lambda^2$, the depletion region is thin compared to the height of the flow chamber and the biosensor length [1], as shown in Fig.2.3. When the Péclet number is large, the PDE equation (2.2) is singularly perturbed. By non-dimensionalizing the PDE and performing some asymptotic analysis, two characteristic length scales are distinguished along the dimension perpendicular to the flow direction [73, 74]. The formation of a thin depletion region on the biosensor surface is due to this two-length scale behaviour as well as a two-time scale behaviour in the system. The two time-scale behaviour occurs because the time it takes the sensor to achieve equilibrium is much greater than the time for the depletion region to form [1]. In this case, we ignore the initial fast variations of analyte concentration in the flow chamber and obtain the slow-time scale solution or the quasi-steady solution of the system, where the depletion region evolves quasi-steadily. In the quasi-steady state, the analyte concentration above the depletion region is at equilibrium, equal to the inlet concentration A^* , and the analyte concentration in the depletion region is slowly varying. The steady-state diffusive flux on the biosensor is obtained as $J = \gamma L w_s \nabla A$, where the gradient on the surface is approximated by $\nabla A = \frac{A^* - a(t)}{\delta}$. Here, δ is the thickness of the depletion region and $a(t)$ is the time-varying analyte concentration in the depletion region. The thickness of the depletion region is approximated as [1]

$$\delta = \frac{h}{1.47} \left(\frac{\lambda}{P_{eH}} \right)^{1/3}. \quad (2.10)$$

Thus, the diffusive flux on the biosensor is obtained by

$$J = (A^* - a(t)) w_s \gamma F, \quad F \approx 1.47 P_{eH}^{1/3} \lambda^{2/3}. \quad (2.11)$$

In the mass-transport limited case, when the biosensor acts as an infinite sink, the analyte concentration on the biosensor surface remains zero and the analyte diffusive flux is obtained by (1.7) as described in Chapter 1.

The two-compartment model approximates the quasi-steady solution of the PDE model (2.2)-(2.7), based on (2.11). Since the dynamics of the immobilized species occur in the slow time, the two-compartment model approximates the concentration variations of these species accurately. As shown in Fig.2.3, the flow chamber on top of the biosensor is divided vertically into two compartments, the outer compartment and the inner compartment, where the latter encompasses the depletion region. The PDE model (2.2)-(2.7) is approximated by a set of coupled ODEs, which models the quasi-steady response of the system by ignoring the brief transitions before the outer compartment concentration falls or rises to the concentration at the inlet of the flow chamber. Consider a single biosensor in the flow chamber (2.1), where the biosensor length is equal to the length of the flow chamber as shown in Fig.2.3. In this model, the concentration in the outer compartment, denoted by A_1 , is equal to the concentration A^* at the inlet of the flow chamber. The dynamics of the spatial average of analyte concentration in the inner compartment, denoted by $a_1(t)$, is described by [43]

$$\delta \frac{da_1(t)}{dt} = \frac{\gamma}{\delta} (A_1 - a_1(t)) - \mathbb{R}(a_1(t), \bar{\mathbf{u}}_1(t)), \quad a_1(0) = 0, \quad (2.12)$$

where

$$\delta = 0.7 \left[\frac{\gamma w h^2 L}{Q} \right]^{1/3} \quad (2.13)$$

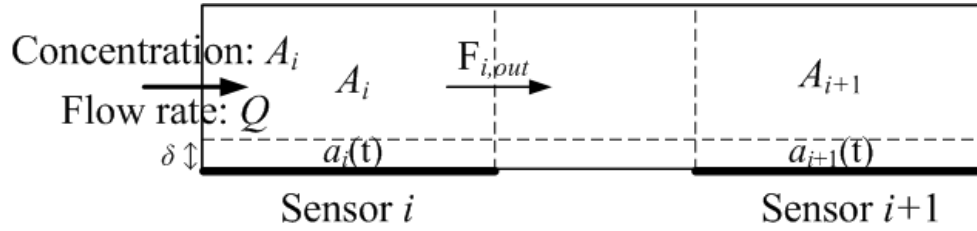


Figure 2.4: Multi-compartment model for two successive biosensors in the array.

is the height of the inner compartment or the depletion zone and is obtained by replacing P_{eH} by (1.6) and $\lambda = \frac{L}{h}$ in (2.10). Here, γ is the diffusion constant, h and $w = w_s = w_c$ are the height and width of the flow chamber, L is the biosensor length, and Q is the volumetric flow rate defined in (1.5). The first term on the right-hand side of (2.12) accounts for the transport of analytes from the outer compartment to the inner compartment obtained by replacing $a(t)$ with $a_1(t)$ in (2.11) whereas $\mathbb{R}(\cdot, \cdot)$ is the rate at which the analytes bind to the biosensor surface. Therefore, the difference between these two terms determines the rate of change of the inner compartment concentration. The average concentration of immobilized species on the biosensor, denoted by $\bar{\mathbf{u}}_1(t)$, depends on $a_1(t)$ through the following set of ODEs, which is coupled with (2.12):

$$\frac{d\bar{\mathbf{u}}_1(t)}{dt} = \mathbb{F}(\bar{\mathbf{u}}_1(t), a_1(t)), \quad t > 0, \quad \bar{\mathbf{u}}_1(0) = \mathbf{u}_0. \quad (2.14)$$

2.2.2 The Multi-Compartment Model

In this section, the PDE model (2.2)-(2.7) is approximated by a system of ordinary differential equations. The flow chamber is partitioned into a series of two-compartment blocks, which are connected by middle compartments as shown in Fig.2.4. For each biosensor, the response can be described by an individual two-compartment model with a different outer compartment concentration. We apply the divergence theorem to the advection-

diffusion PDE of (2.2) in the outer compartment associated with each biosensor to find the concentration at the inlet of the next biosensor.

The following multi-compartment characterization is the main result of this section. Consider the flow of analytes over an equally spaced linear array of N identical biosensors in the flow chamber (2.1). Assume that $P_{eH} \gg 1/\lambda^2$ and $P_{eH} \gg \lambda$. Suppose the analyte concentration at the inlet of the flow chamber is constant and equal to A^* . The concentration of analytes and immobilized species are described by the PDE model (2.2)-(2.7). Assume that the binding rate $\mathbb{R}(A, \mathbf{u})$ on each biosensor is of the form (2.6). Then, the dynamics of the surface average concentration of immobilized species on biosensor i , denoted by $\bar{\mathbf{u}}_i(t)$, can be approximately described by

$$\delta \frac{da_i(t)}{dt} = \frac{\gamma}{\delta} (A_i - a_i(t)) - \mathbb{R}(a_i(t), \bar{\mathbf{u}}_i(t)), \quad t > \tilde{t}_i \quad (2.15)$$

$$\frac{d\bar{\mathbf{u}}_i(t)}{dt} = \mathbb{F}(\bar{\mathbf{u}}_i(t), a_i(t)), \quad t > \tilde{t}_i \quad (2.16)$$

$$a_i(\tilde{t}_i) = 0, \quad \bar{\mathbf{u}}_i(\tilde{t}_i) = \mathbf{u}_0, \quad i \in \{1, \dots, N\}.$$

Here, A_i is the outer-compartment concentration above biosensor i , which is obtained by the following recursion for $i \in \{1, \dots, N-1\}$:

$$A_{i+1} = \alpha A_{i-1}, \quad \alpha = 1 - \frac{w\gamma L D_a}{Q\delta(1 + D_a)}, \quad A_1 = A^*, \quad (2.17)$$

where D_a is the Damkohler number obtained as

$$D_a = \frac{\delta R_f(\mathbf{u}_0)}{\gamma}. \quad (2.18)$$

Here, R_f is defined in (2.6).

In (2.15), $a_i(t)$ denotes the spatial average of analyte concentration in the inner com-

partment of biosensor i . The height of the inner compartment above each biosensor is denoted by δ , which is obtained by (2.13). The time \tilde{t}_i , defined as

$$\tilde{t}_i = \frac{wx_{i,1}h}{Q}, \quad i \in \{1, \dots, N\}, \quad (2.19)$$

approximates the time when the flow reaches the near end of biosensor i . The accuracy of the above model is evaluated for an array of ICS biosensors in Section 2.3.

Derivation of the multi-compartment model (2.15)-(2.19): We use an inductive construction described as follows: Assume that the ODE set (2.15)-(2.16) with concentration A_i describes the dynamics of biosensor i . Then, we derive (2.15)-(2.16) for biosensor $i + 1$, where A_{i+1} is obtained by (2.17). For $i = 1$, the ODE set (2.15)-(2.16) represents the well-known two-compartment model for the first biosensor.

Assume that (2.15-2.16) is accurate for biosensor i and that the associated outer compartment has the concentration A_i . The aim is to compute the outward flux that is indicated by $F_{i,out}$ in Fig.2.4 at the outlet of the outer compartment above biosensor i . By applying the divergence theorem to (2.2) in the region inside this compartment, the total outward flux through this volume is obtained as zero. Hence, $F_{i,out}$ is obtained by subtracting the flux towards the inner compartment from the inward flux A_iQ at the inlet of the compartment:

$$F_{i,out} = QA_i - \frac{Lw\gamma}{\delta} (A_i - a_i(t)). \quad (2.20)$$

We then estimate the concentration in the middle compartment between biosensors i and $i + 1$ by

$$A_{i+1} = \frac{\int_{\Delta t} F_{i,out} dt}{Q\Delta t}, \quad (2.21)$$

where Δt is the time it takes the flow to traverse the middle compartment obtained as

$$\Delta t = \frac{hwd}{Q}, \quad (2.22)$$

where d is the spacing between the biosensors. Using (2.20), (2.21) can be written as

$$A_{i+1} = A_i \left(1 - \frac{Lw\gamma}{Q\delta} \right) + \frac{Lw\gamma}{\delta Q \Delta t} \int_{\Delta t} a_i(t) dt. \quad (2.23)$$

In order to compute the above integral, we exploit the two-time scale behaviour of the ODE set (2.15)-(2.16). In the ODE system (2.15)-(2.16), $a_i(t)$ is fast varying compared to $\bar{\mathbf{u}}_i$ because of the small coefficient h_0 of the derivative $da_i(t)/dt$ [55, 73]. For high flow rates, Δt has a small value that lies within the transit time response of $a_i(t)$. During this time, the slow variable $\bar{\mathbf{u}}_i(t)$ is roughly constant and equal to its initial value. By replacing $R(A, \mathbf{u})$ with (2.6) and $\bar{\mathbf{u}}_i(t)$ with the constant \mathbf{u}_0 , a linear ODE for the variations of $a_i(t)$ is obtained by (2.15), which is solved as

$$a_i(t) = \frac{\gamma A_i}{\gamma + \delta R_f(\mathbf{u}_0)} \left(1 - \exp \left(-\frac{\gamma + \delta R_f(\mathbf{u}_0)}{\delta^2} t \right) \right). \quad (2.24)$$

For the given binding rate $\mathbb{R}(\cdot, \cdot)$ in (2.6), the Damkohler number D_a is obtained by (2.18).

Considering the definition of the Damkohler number D_a in (2.18), (2.24), and (2.22), (2.23) can be rewritten as

$$A_{i+1} = A_i \left(1 - \frac{wL\gamma D_a}{Q\delta(1 + D_a)} - \frac{A_i L \delta}{dh (1 + D_a)^2} \left(1 - \exp \left(-\frac{\gamma h w d}{\delta^2 Q} (1 + D_a) \right) \right) \right).$$

Since δ is small, the second term on the right-hand side of the above equation is negligible and therefore A_{i+1} can be approximated as (2.17). The concentration A_{i+1} is obtained

as the concentration at the inlet of biosensor $i + 1$. Therefore, biosensor $i + 1$ acts like a single biosensor in the flow chamber with constant concentration at the inlet. Thus, the ODE set (2.15)-(2.16) with the concentration A_{i+1} in the outer compartment can be used to describe the variations of \mathbf{u}_{i+1} on biosensor $i + 1$.

2.3 Case-Study: Ion Channel Switch Biosensor

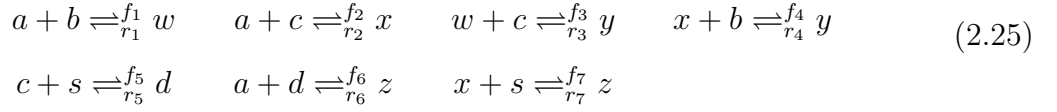
In this section, the multi-compartment model of Section 2.2.2 is evaluated for an array of ICS biosensors introduced in Chapter 1. The PDE model of Section 2.1 is specified for this biosensor by describing the corresponding chemical reactions and measurement equation in Section 2.3.1. Comparison between the responses of the multi-compartment model and the PDE model in Section 2.3.2, shows that the multi-compartment model describes the system accurately.

2.3.1 Dynamics of Analyte Flow on Ion Channel Switch

Biosensor

In this section, the PDE model of Section 2.1 is constructed for a linear array of ICS biosensors by specifying the reaction equations and boundary conditions on the biosensor. As described in Section 1.4.1 in Chapter 1, binding of analytes to the capture sites on the ICS biosensor reduces the average formation of conducting dimers on the biosensor. In this process, seven chemical reactions with eight immobilized species are involved [45]. The primary species include binding site b with concentration B , free moving ion channel c with concentration C , tethered ion channel s with concentration S , and dimer d with concentration D . Initially, free moving ion channels c , tethered channel s , dimers d are in equilibrium through a reversible chemical reaction. The arrival of analytes initiates six

other reactions and the equilibrium shifts towards decreasing the dimer concentration. The analyte binds to the primary species to form complexes w , x , y , and z with concentrations W , X , Y , and Z according to the following chemical reactions:



Here, f_j and r_j for $j \in \{1, 2, \dots, 7\}$, respectively denote the forward and backward reaction rate constants. The corresponding rate equations for the reactions (2.25) are

$$\begin{aligned} R_1 &= f_1AB - r_1W & R_2 &= f_2AC - r_2X & R_3 &= f_3WC - r_3Y & R_4 &= f_4XB - r_4Y \\ R_5 &= f_5CS - r_5D & R_6 &= f_6AD - r_6Z & R_7 &= f_7XS - r_7Z. \end{aligned}$$

The vector $\mathbf{u} = [B, C, D, S, W, X, Y, Z]^T$ contains the concentration values of the immobilized species. Here, $(\cdot)^T$ denotes transpose. Define $f(\mathbf{u}, A) = [R_1, R_2, R_3, R_4, R_5, R_6, R_7]^T$, where $(\cdot)^T$ denotes transpose. The concentration vector of the species on biosensor i at position x is denoted by $\mathbf{u}_i(t, x)$ and its dynamics is described by [62]

$$\frac{d\mathbf{u}_i(t, x)}{dt} = Mf(\mathbf{u}_i(t, x), A(t, x, 0)) \quad \text{for } t > 0, \quad \mathbf{u}_i(0) = \mathbf{u}_0, \quad (2.26)$$

where M is a 7×7 constant matrix whose elements are 0, 1 and -1 and is derived from the reactions in (2.25) [62]. From the reactions (2.25), the binding rate of analytes to the surface of biosensor i can be written as $\mathbb{R}(A, \mathbf{u}_i) = f_1AB_i + f_2AC_i + f_6AD_i - r_1W_i - r_2X_i - r_6Z_i$. Thus, the corresponding boundary condition in (2.5) can be expressed as

$$\gamma \frac{\partial A}{\partial z} \Big|_{z=0} = Aq^T \mathbf{u}_i - p^T \mathbf{u}_i, \quad i \in \{1, 2, \dots, N\}, \quad (2.27)$$

where the vectors q and p are defined as $q = [f_1 \ f_2 \ f_6 \ 0 \ 0 \ 0 \ 0 \ 0]^T$ and $p = [0 \ 0 \ 0 \ 0 \ r_1 \ r_2 \ 0 \ r_6]^T$. Applying a small alternative potential between the gold substrate and a reference electrode in the test solution generates a charge at the gold surface, which causes electrons flow through ion channels. By measuring the current in the external circuit, we can record the variations of biosensor conductance, which is proportional to the surface average dimer concentration. Denoting the average dimer concentration of biosensor i by $\bar{D}_i(t)$, the observation equation, on biosensor i , can be written as $m_i(t) = \bar{D}_i(t) + n_i(t)$, where $n_i(t)$ is a white Gaussian noise. In the analysis of patch clamping of ion channels using hidden Markov models, it is justified that the noise in the measured current of ion channels can be considered to be Gaussian [75].

2.3.2 Illustration of the Accuracy of the Multi-Compartment Model

This section considers a uniform biosensor array comprising four identical ICS biosensors. The aim is to show that the multi-compartment model of Section 2.2.2 yields an excellent approximation to the flow dynamics. The height and width of the flow chamber are $h = 0.1$ mm and $w = 3$ mm. The biosensor length and array spacing are respectively $L = 2$ mm and $d = 1$ mm and the diffusion constant is $\gamma = 10^{-6}$ cm²/s. For the given example, the accuracy of the multi-compartment model is validated for the concentration A^* in the range $10^{-11} \sim 10^{-8}$ Mol/m³ and the flow rate in the range $10 \sim 100\mu\text{L}/\text{min}$. The notation Mol/m³ stands for mole per meter cube.

The response of biosensors obtained by the multi-compartment model (2.15)-(2.19) is simulated and compared with the response of the PDE model (2.2)-(2.4), (2.26)- (2.27). The Comsol multi-physics simulation software is used to solve the PDE via the finite

element method. [†] The relative error tolerance of the solution is less than 0.001. The ODE set (2.15)-(2.19) is solved using the `ode23s` ODE solver in the MATLAB ODE suite [77]. This solver is based on the Rosenbrock methods [78] for stiff differential equations that contain multiple characteristic time scales.

Since the measured output of the biosensor is proportional to the average dimer concentration, define the normalized error between the ODE and PDE responses as

$$e_i(t) = |\bar{D}_i(t) - \bar{D}_i^{\text{ODE}}(t)| / \bar{D}_i(t), \quad i = 1, \dots, N, \quad (2.28)$$

where $\bar{D}_i(t)$ is the average dimer concentration on biosensor i , obtained by the PDE model (2.2)-(2.4), (2.26)-(2.27). $\bar{D}_i^{\text{ODE}}(t)$ is the corresponding response from the multi-compartment model (2.15)-(2.19). Fig.2.6 shows the normalized error (2.28) versus time for the values $A^* = 10^{-11}$ and $A^* = 10^{-8}$ Mol/m³ of the concentration at the inlet of the flow chamber. It can be seen that the error during 400 seconds of simulation time is less than 0.007% for $A^* = 10^{-11}$ Mol/m³ and less than 4.5% for $A^* = 10^{-8}$ Mol/m³ for all the biosensors.

Fig.2.7 shows the normalized error (2.28) for different flow rates for $A^* = 10^{-8}$ Mol/m³ and $A^* = 10^{-11}$ Mol/m³. There are four biosensors in the flow chamber but the results are illustrated for only the biosensor which has the maximum range of variations in the error. The figure shows that by increasing the flow rate to 100μL/min, the multi-compartment model (2.15)-(2.19) remains accurate within 4.5% error.

In order to validate the accuracy of the multi-compartment method, one should validate the convergence of the finite element solution to the exact PDE solution. According to

[†]The predefined `convection and diffusion` application mode in Comsol is used to define the governing PDE in the domain. The ODEs on the boundary are defined through the `weak form` boundary setting. There are 2947 triangular elements in the finite element solver. The PDE system is converted to algebraic equations, which are solved by a multifrontal massively parallel sparse direct solver (MUMPS) [76]. MUMPS is a solver for large sparse systems of linear algebraic equations, which is based on parallel computing and distributed memory [76].

[79], stability and consistency of the finite element solver imply the convergence of the solution. The underlying finite element discretization method in COMSOL Multiphysics is the Galerkin method [80]. When discretizing (2.2), the numerical scheme becomes unstable for a large Péclet number, which is the case in our problem. However, stabilization methods exist to take care of this problem. In our case, Comsol uses the streamline-upwind/petro-galerkin (SUPG) method, which is a consistent stabilized method [80, 81]. In SUPG, an artificial diffusion is added to the numerical scheme while keeping it consistent [82]. A powerful way to investigate the convergence of the finite element solution is to confirm that [83]

$$\|u(\cdot, t) - u_{\Delta}(\cdot, t)\|_{L^2(\Omega)} \leq C\Delta^{\lambda}, \quad (2.29)$$

as $\Delta \rightarrow 0$. Here, $u(\cdot, t)$ denotes the PDE solution at time t , $u_{\Delta}(\cdot, t)$ is the finite element solution with the mesh size Δ , and $\lambda > 0$ is the convergence order of the finite element method. The constant C is independent of λ . If the PDE solution is not available in analytic form, the convergence study can still be carried out by using the finite element solution on the finest mesh as the so-called reference solution. This is the standard approach in the case that the PDE solution is not available [83]. For the PDE model (2.2)-(2.7), (2.29) translates to

$$\|A(t, \cdot, \cdot) - A_{\Delta}(t, \cdot, \cdot)\| + \sum_{i=1}^N \|\mathbf{u}_i(t, \cdot) - \mathbf{u}_{i,\Delta}(t, \cdot)\| \leq C\Delta^{\lambda}, \quad (2.30)$$

where $A(t, \cdot, \cdot)$ and $\mathbf{u}_i(t, \cdot)$ are the reference solutions of the PDE model and are obtained for the finest mesh size selected as $\Delta = 10^{-5}\text{m}$. One way to visualize (2.30) is a log-log plot of the error on the left-hand side of (2.30) versus the reciprocal of the mesh spacing, $1/\Delta$ [83]. Fig.2.5 show plots of this type for different time points. The plots are obtained

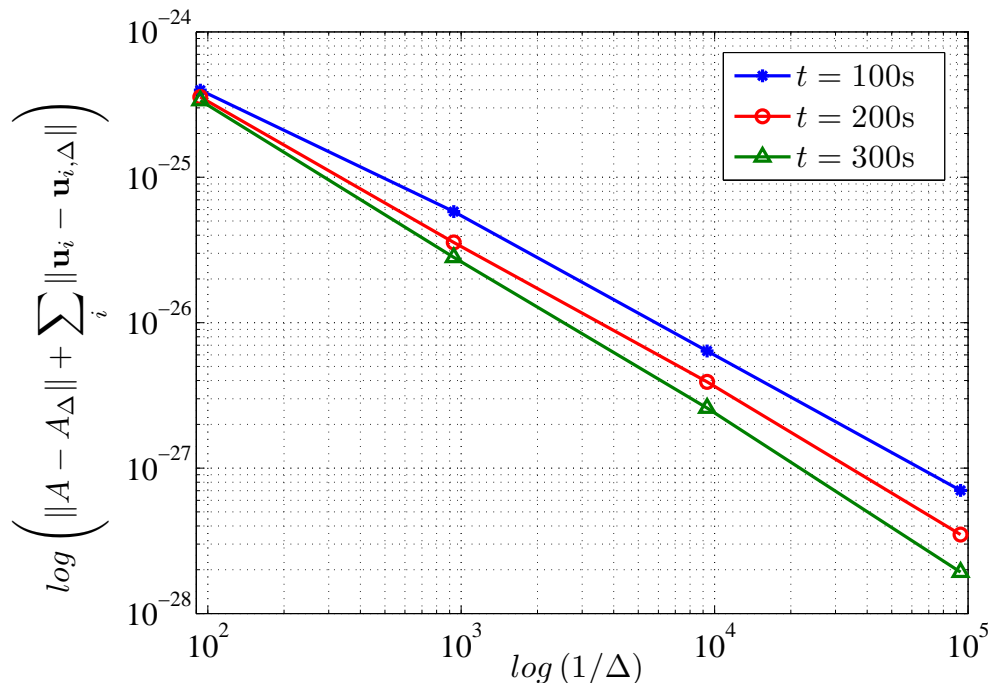
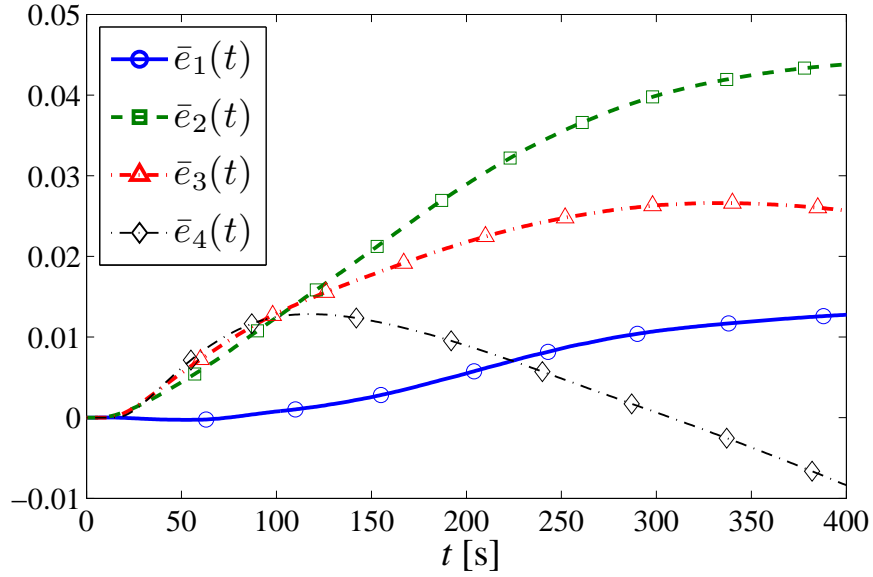


Figure 2.5: Convergence studies of the finite element solution of the PDE model (2.2)-(2.7): Convergence studies are performed by investigating (2.29). For the PDE model (2.2)-(2.7), (2.29) is formulated as (2.30), where $A(t, \cdot, \cdot)$ and $\mathbf{u}_i(t, \cdot)$ are the reference solutions of the PDE model obtained for the finest mesh size $\Delta = 10^{-5}\text{m}$. The convergence order is obtained as $\lambda \approx 1$.

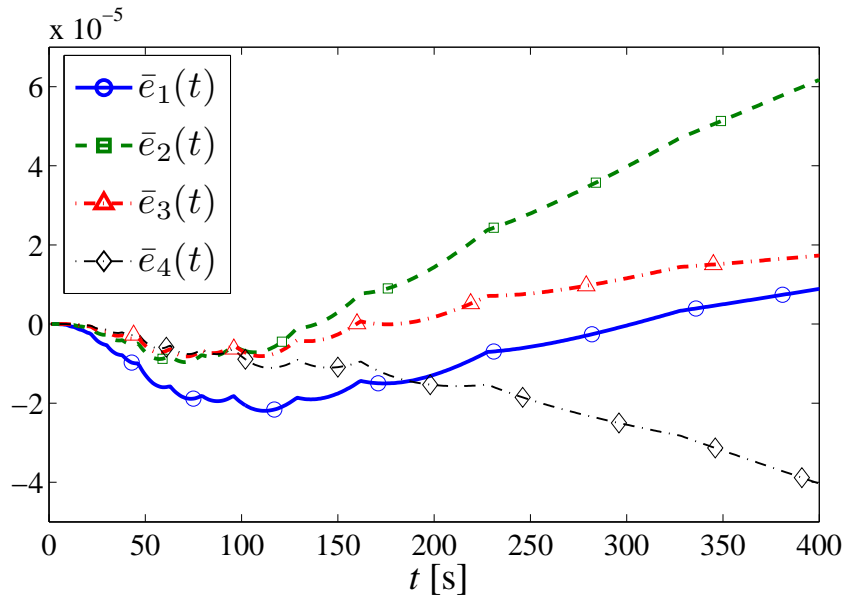
by post processing the solution data in MATLAB. In order to compute the L^2 norm of the difference between the reference solution and a solution on a lower refined mesh, we use interpolation on the reference finest mesh. The results of Fig.2.5 show that the convergence order is $\lambda \approx 1$.

2.4 Summary

In this chapter, we constructed the PDE model (2.2)-(2.7) to describe the dynamics of the flow of analytes over a linear array of reactive surface-based biosensors in a flow chamber. The PDE model is general in the sense that it is applicable to any type of capture sur-



(a)



(b)

Figure 2.6: The normalized error (2.28) between the multi-compartment ODE model (2.15)-(2.19) and the PDE model (2.2)-(2.7) for $A^* = 10^{-8}$ Mol/m³ (a) and $A^* = 10^{-11}$ Mol/m³ (b). The flow rate is $Q = 10$ μ L/min. There are $N = 4$ biosensors with the length $L = 2$ mm and spacing $d = 1$ mm in the flow chamber.

face. The PDE model is then approximated by the multi-compartment model (2.15)-(2.19), which is derived by extending the two-compartment model using asymptotic analysis and

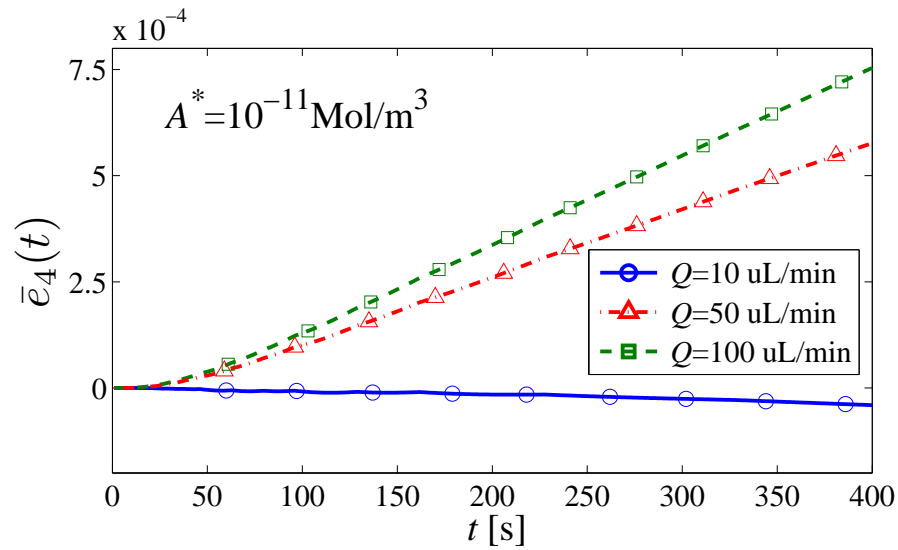
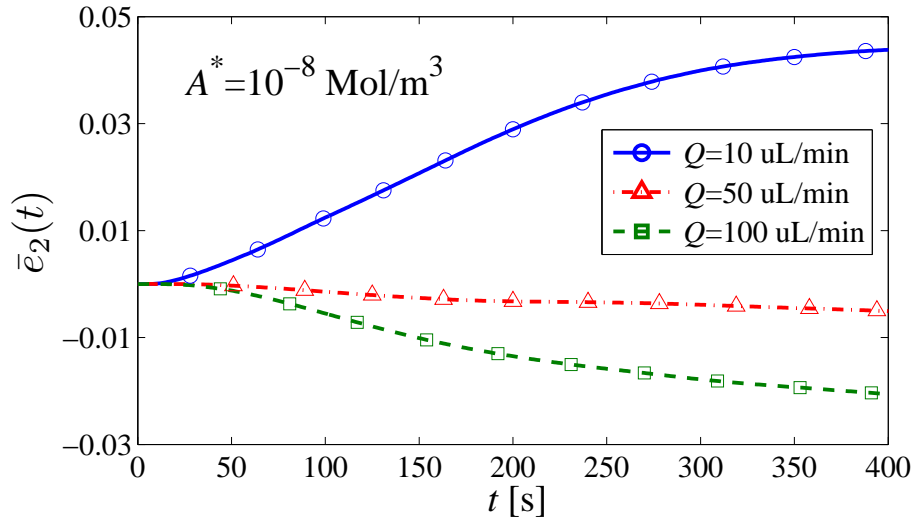


Figure 2.7: The normalized error (2.28) between the multi-compartment ODE model (2.15)-(2.19) and the PDE model (2.2)-(2.7) for different flow rates for $A^* = 10^{-8} \text{ Mol/m}^3$ (a) and $A^* = 10^{-11} \text{ Mol/m}^3$ (b) for the second (a) and fourth (b) biosensor. There are $N = 4$ biosensors in the flow chamber in each case, but the results are illustrated for only the biosensor with the maximum variations in the error. The biosensor length and spacing are respectively $L = 2 \text{ mm}$ and $d = 1 \text{ mm}$.

the divergence theorem. The multi-compartment model provides an insight to understanding the dynamics of a biosensor array. We use this model in the next chapter for estimation of injection concentration in the flow chamber. In Chapter 4, we utilize this model to improve biosensor response.

The approximate multi-compartment model predicts the response of the ICS biosensor array accurately for the injection analyte concentrations between 10^{-11} Mol/m³ and 10^{-8} Mol/m³. The prediction error remains less than 7% during 400 seconds of simulation time. As mentioned in Section 2.2.1, the approximate model describes the system accurately in the quasi-steady state before the biosensors achieve equilibrium. Thus, the modeling error grows with time as the biosensor reactions approach equilibrium. However, the model is accurate within the time range required for analyzing the dynamics of analyte and biosensor interactions and estimation of the injection analyte concentration in the flow chamber. In this model, the entire infinite dimensional state space PDE system is converted to only a few dimensional ODE system. The derived ODE system does involve even less state space variables than those obtained by applying conventional discretization methods such as the finite element method.

Chapter 3

Estimating Molecular Concentration in Fluid Flows

Using the multi-compartment model, derived in Chapter 2, this chapter deals with estimating the concentration of target molecules that flow past multiple biosensors in the flow chamber (2.1). This is a parameter estimation problem in the advection-diffusion-reaction PDE model (2.2)-(2.7). The PDE model comprises a parabolic PDE coupled with Dirichlet and Neumann boundary conditions [84, 85, 86].

The problem involves estimation of the injection concentration at the inlet of the flow chamber, which is one of the boundary conditions in the parabolic PDE (2.2). The PDE is coupled with ODEs on the boundary and cannot be solved analytically. Therefore, numerical methods should be used to solve the estimation problem. Modal approximation method, spline methods, and operator factorization methods are some of conventional numerical methods, which involve approximating the infinite dimensional space with a finite dimensional space of functions [17]. These approximation methods result in solving a high-dimensional system, which is nonlinear in most problems including our case. Instead of using these approximation methods, we use the multi-compartment model developed in Chapter 2 to convert the system description from a distributed-parameter into a lumped-parameter form. Using the multi-compartment model to solve the estimation problem significantly reduces the amount of computation in each step of the solution. This conversion results in a system of a few ODEs, which is used to estimate the analyte con-

centration in this chapter. The infinite dimensional parabolic PDE is exactly converted to N ODEs, where N is the number of biosensors in the array. These ODEs are coupled with the ODE sets on the boundary. The model is derived by extending the well-known two-compartment model, which has been widely used for studying binding kinetics of molecular species [41, 55, 68, 87, 88, 89]. In this chapter, we develop the two-compartment model to a multi-compartment model applicable to an array of biosensors. We use the derived model to estimate the analyte concentration using a biosensor array. As mentioned earlier in Chapter 1, this is a non-standard estimation problem since the measurement process affects the system state. Each biosensor grabs analytes and changes the concentration of the flow over the successive biosensors. The aim of this work is to investigate how the number of biosensors affects the error in the estimation of the initial target molecule concentration. The multi-compartment model provides an insight to the dynamical behaviour of the system, which is used to explain the variations of estimation variance with the number of biosensors. Based on the multi-compartment model, analytic expressions are derived to evaluate the estimation variance and bias. The variations of the estimation bias and variance can be justified through the derived expressions.

The main contributions of this chapter are stated as follows:

1. Estimation of analyte concentration is posed as a parameter estimation problem in the derived multi-compartment ODE model of Chapter 2. The estimate is computed numerically for an ICS biosensor via the nonlinear least squares method.
2. The main result is the derivation of analytic expressions for the finite-sample variance and bias of the estimator based on the multi-compartment model. Using these expressions, the attainable improvement in the estimation bias and variance can be quantitatively predicted. The results are justified through the multi-compartment model.

3. It is shown that there is an extra improvement to the estimation error compared to the conventional case of multiple-sensor measurements. By extra improvement, we mean that the estimation variance can be reduced to less than $1/N$ by using N biosensors. This unusual result can be explained using the derived expression for the variance and the saturating behaviour of the biosensor response. An analytic expression is derived for the maximum number of biosensors for which this result is valid.

In Section 3.1, the concentration estimation problem is formulated as an output least squares problem and solved using the multi-compartment model of Section 2.2. The properties of the finite-sample least-squares estimator is analyzed in Section 3.2.

3.1 Least Squares Estimator of the Initial Concentration

With the multi-compartment characterization of the analyte concentration, developed in Chapter 2, this section deals with estimating the concentration A^* at the inlet of the flow chamber. The estimation is formulated as a least squares problem for the multi-compartment ODE model (2.15)-(2.19).

The concentration A^* at the inlet of the flow chamber is estimated using nonlinear regression. Using N biosensors and S time samples at each biosensor, the estimate of A^* , denoted by \hat{A}^* , is obtained as

$$\hat{A}^* = \arg \min_{A \in R^+} S^{-1} \sum_{i=1}^N \sum_{k=1}^S (m_{i,k} - \tilde{g}_{i,k}(A))^2, \quad (3.1)$$

where $m_{i,k}$ is the measurement of biosensor i at time $t_{i,k}$, and $\tilde{g}_{i,k}(A) = \tilde{g}_i(A, t_{i,k})$ is the

response of biosensor i at time $t_{i,k}$ obtained by the approximate multi-compartment ODE model (2.15)-(2.19) with the initial concentration $A_1 = A$. Here, $\tilde{g}_i(A, t)$ in the multi-compartment ODE model is the counterpart of the PDE response (2.8). Considering (2.8), $\tilde{g}_i(A, t)$ is obtained as

$$\tilde{g}_i(A, t) = G(\bar{\mathbf{u}}_i(t)), \quad (3.2)$$

where $\bar{\mathbf{u}}_i(t)$ satisfies the multi-compartment ODE model (2.15)-(2.19). According to (2.9), the measurement $m_{i,k}$, at time $t_{i,k}$ on biosensor i , for $i \in \{1, \dots, N\}$ and $k \in \{1, \dots, S\}$, can be expressed as

$$m_{i,k} = \tilde{g}_{i,k}(A^*) + e_{i,k}(A^*) + n_{i,k}, \quad (3.3)$$

where $e_{i,k}(A)$ refers to the difference between the ODE response $\tilde{g}_{i,k}(A)$ and its corresponding PDE response $g_{i,k}(A)$. The least squares estimate \hat{A}^* is the solution of the optimization problem defined by (3.1)-(3.2), where $\bar{\mathbf{u}}_i(t)$ satisfies the multi-compartment ODE model (2.15)-(2.19) and the measurements are given by (3.3). The Gauss-Newton method [90] is used to solve the least squares problem.

In order to solve the optimization problem (3.1), the model is first non-dimensionalized. Since the system dynamics in our example change in a very small range of values, non-dimensionalization reduces the effect of numerical errors on the convergence of the algorithm.

Consider the multi-compartment ODE model (2.15)-(2.19) with the parameter δ given in (2.13). Denote $\tau = \frac{\gamma t}{h^2}$, $\beta_i = \frac{\bar{\mathbf{u}}_i}{\bar{\mathbf{u}}_0^{(1)}}$, $\beta_0 = \frac{\bar{\mathbf{u}}_0}{\bar{\mathbf{u}}_0^{(1)}}$, $\tilde{\tau}_i = \frac{\gamma \tilde{t}_i}{h^2}$, and $h_1 = \frac{\delta}{h}$, then the ODE model

(2.15)-(2.19) can be rewritten as

$$\begin{aligned} h_1 \frac{da_i}{d\tau} &= \frac{1}{h_1} (\alpha^{i-1} A^* - a_i) - \frac{h}{\gamma} \mathbb{R} \left(a_i, \bar{\mathbf{u}}_0^{(1)} \beta_i \right), \quad \tau > \tilde{\tau}_i \\ \frac{d\beta_i}{d\tau} &= \frac{h^2}{\gamma \bar{\mathbf{u}}_0^{(1)}} \mathbb{F} \left(\beta_i \bar{\mathbf{u}}_0^{(1)}, a_i \right), \quad \tau > \tilde{\tau}_i \\ a_i(\tilde{\tau}_i) &= 0, \quad \beta_i(\tilde{\tau}_i) = \beta_0, \quad i \in \{1, \dots, N\}. \end{aligned} \quad (3.4)$$

Here, $\bar{\mathbf{u}}_0^{(1)}$ denotes the first element of the vector $\bar{\mathbf{u}}_0$.

Using (3.2), (3.1) can be rewritten as

$$\hat{A}^*(S) = \arg \min_{A^* \in \mathbb{R}^+} \sum_{i=1}^N \sum_{k=1}^S \left(m_{i,k} - G(\bar{\mathbf{u}}_0^{(1)} \beta_i(\tau_{i,k})) \right)^2, \quad (3.5)$$

where $\beta_i(\tau)$ for $i \in \{1, \dots, N\}$ satisfies (3.4). The optimization problem (3.4)-(3.5) is a one-dimensional optimization problem, which is solved by the Gauss-Newton method.

3.2 Analytic expressions for the variance and bias of the estimate \hat{A}^*

Using the multi-compartment model, the variance and bias of the estimator \hat{A}^* can be approximated as

$$E \left(\hat{A}^* - E(\hat{A}^*) \right)^2 \approx \frac{\sigma^2}{\sum_{i=1}^N \alpha^{2i-2} \sum_{k=1}^S \left| \frac{\partial \tilde{g}}{\partial A}(\alpha^{i-1} A^*, \tilde{t}_{i,k}) \right|^2}, \quad (3.6)$$

$$E \left(\hat{A}^* - A^* \right) \approx \frac{\sum_{i=1}^N \sum_{k=1}^S \alpha^{i-1} e_{i,k}(A^*) \frac{\partial \tilde{g}}{\partial A}(\alpha^{i-1} A^*, \tilde{t}_{i,k})}{\sum_{i=1}^N \alpha^{2i-2} \sum_{k=1}^S \left| \frac{\partial \tilde{g}}{\partial A}(\alpha^{i-1} A^*, \tilde{t}_{i,k}) \right|^2} \quad (3.7)$$

$$-\frac{\sigma^2 \sum_{i=1}^N \sum_{k=1}^S \alpha^{3i-3} \frac{\partial \tilde{g}}{\partial A}(\alpha^{i-1} A^*, \tilde{t}_{i,k}) \frac{\partial^2 \tilde{g}}{\partial A^2}(\alpha^{i-1} A^*, \tilde{t}_{i,k})}{2 \left(\sum_{i=1}^N \alpha^{2i-2} \sum_{k=1}^S \left| \frac{\partial \tilde{g}}{\partial A}(\alpha^{i-1} A^*, \tilde{t}_{i,k}) \right|^2 \right)^2},$$

where $\tilde{g}(A, t) = F(\bar{\mathbf{u}}_1(t))$ is the response of a single biosensor, obtained by the two-compartment model (2.12)-(2.14), when the initial concentration is $A_1 = A$ and the sensor edge is positioned at the inlet of the flow chamber. The derivatives $\frac{\partial \tilde{g}}{\partial A}(\alpha^{i-1} A^*, \tilde{t}_{i,k})$ and $\frac{\partial^2 \tilde{g}}{\partial A^2}(\alpha^{i-1} A^*, \tilde{t}_{i,k})$ are respectively the values of $\partial \tilde{g} / \partial A(A, t)$ and $\partial^2 \tilde{g} / \partial A^2(A, t)$ at $A = \alpha^{i-1} A^*$ and $t = \tilde{t}_{i,k}$. Here $\tilde{t}_{i,k}$ denotes the time difference $\tilde{t}_{i,k} = t_{i,k} - \tilde{t}_i$. Time variations of $\partial \tilde{g} / \partial A$ and $\partial^2 \tilde{g} / \partial A^2$ depend on the variations of the first and second derivatives of the concentration vector $\bar{\mathbf{u}}_1$ with respect to the initial concentration $A_1 = A$. By taking the first and second derivatives of the system of ODEs (2.12) and (2.14) with respect to A_1 , other sets of ODEs are obtained, which describe the time variations of the derivatives of the concentration vector $\bar{\mathbf{u}}_1$ with respect to the initial concentration A_1 . The new sets of ODEs can be solved numerically to obtain the values of $\partial \tilde{g} / \partial A$ and $\partial^2 \tilde{g} / \partial A^2$ in (3.6) and (3.7). In the experiments involving the ICS biosensor, the approximations (3.6) and (3.7) are used to explain how the variance and bias of the estimator vary with the number of biosensors. In the following, the derivation of (3.6) and (3.7) is explained.

Derivation of (3.6) and (3.7): Denote the derivative of the objective function in (3.1) by $U(A, \mathbf{m})$, where the vector \mathbf{m} contains all the measurements $m_{i,k}$ for $i \in \{1, \dots, N\}$ and $k \in \{1, \dots, S\}$. The derivative is obtained as

$$U(A, \mathbf{m}) = 2S^{-1} \sum_{i,k} \frac{\partial \tilde{g}_{i,k}}{\partial A}(A) (\tilde{g}_{i,k}(A) - m_{i,k}) \quad (3.8)$$

For the estimate \hat{A}^* , the derivative is zero:

$$U(\hat{A}^*, \mathbf{m}) = 0, \quad (3.9)$$

which indicates that \hat{A}^* is an implicit function of \mathbf{m} . In the following, \hat{A}^* is approximated by the third order Taylor series expansion at $m_{i,k} = \tilde{g}_{i,k}(A^*)$ for all $i \in \{1, \dots, N\}$ and $k \in \{1, \dots, S\}$. The first term in the expansion is the value of \hat{A}^* obtained at error free measurements $m_{i,k} = \tilde{g}_{i,k}(A^*)$. From (3.8) and (3.9), \hat{A}^* is equal to A^* at this point. For simplicity, $\sum_{i=1}^N \sum_{k=1}^S$ is denoted by $\sum_{i,k}$ and the value of the derivative $\partial^\beta \hat{A}^* / \partial m_{i,k}^\beta$ at the point $m_{i,k} = \tilde{g}_{i,k}(A^*)$ and $\hat{A}^* = A^*$ is denoted by $\partial_{i,k}^\beta \hat{A}^*$ in the rest of this section. The third order Taylor series expansion yields

$$\begin{aligned} \hat{A}^* &= A^* + \sum_{i,k} (n_{i,k} + e_{i,k}(A^*)) \partial_{i,k} \hat{A}^* \\ &+ \frac{1}{2} \sum_{i,k} (n_{i,k} + e_{i,k}(A^*))^2 \partial_{i,k}^2 \hat{A}^* \\ &+ \frac{1}{6} \sum_{i,k} (n_{i,k} + e_{i,k}(A^*))^3 \partial_{i,k}^3 \hat{A}^* + \sum_{i,k} O((n_{i,k} + e_{i,k})^4). \end{aligned} \quad (3.10)$$

Here, $O(f(x))$ as $x \rightarrow 0$ is the big 'O' notation, which denotes the set of all functions $h(x)$ such that $|h(x)| \leq c|f(x)|$ for $|x| < \delta$ for $\delta > 0$ and $c > 0$ [91]. Denote $e = \max(|e_{i,k}(A^*)|)$ for $i \in \{1, \dots, N\}$ and $k \in \{1, \dots, S\}$. According to (3.10), the bias of the estimator can then be expressed as

$$\begin{aligned} E(\hat{A}^* - A^*) &= \sum_{i,k} e_{i,k}(A^*) \partial_{i,k} \hat{A}^* + \sum_{i,k} \frac{\sigma^2}{2} \partial_{i,k}^2 \hat{A}^* \\ &+ \sum_{i,k} \frac{e_{i,k}^2(A^*)}{2} \partial_{i,k}^2 \hat{A}^* + \sum_{i,k} \frac{\sigma^2}{2} e_{i,k}(A^*) \partial_{i,k}^3 \hat{A}^* \\ &+ \sum_{i,k} \frac{1}{6} e_{i,k}^3(A^*) \partial_{i,k}^3 \hat{A}^* + O(\sigma^4) + O(\sigma^4)O(e) + O(\sigma^2)O(e^2) + O(e^4) \end{aligned} \quad (3.11)$$

The variance of the estimator can be expressed as

$$E(\hat{A}^* - E(\hat{A}^*))^2 = E(\hat{A}^* - A^*)^2 - (E(\hat{A}^* - A^*))^2$$

Expanding the above terms by using (3.10) and (3.11) yields

$$E \left(\hat{A}^* - E(\hat{A}^*) \right)^2 = \sum_{i,k} \sigma^2 \left| \partial_{i,k} \hat{A}^* \right|^2 \quad (3.12)$$

$$+ O(\sigma^4) + O(\sigma^2 e) + O(e^5).$$

According to (3.11), the bias of the estimator can be expressed as

$$E \left(\hat{A}^* - A^* \right) = \sum_{i,k} e_{i,k}(A^*) \partial_{i,k} \hat{A}^* + \sum_{i,k} \frac{\sigma^2}{2} \partial_{i,k}^2 \hat{A}^* \quad (3.13)$$

$$+ O(e^2) + O(\sigma^2 e) + O(\sigma^4)$$

In the following, the values of $\partial_{i,k} \hat{A}^*$ and $\partial_{i,k}^2 \hat{A}^*$ that appear in (3.12) and (3.13) are obtained by taking the first and second derivatives of (3.9) with respect to $m_{i,k}$ and evaluate them at $\hat{A}^* = A^*$ and $m_{i,k} = \tilde{g}_{i,k}(A^*)$ for $i \in \{1, \dots, N\}$ and $k \in \{1, \dots, S\}$. Taking the first derivative of (3.9) with respect to $m_{i,k}$ yields

$$\frac{\partial U}{\partial \hat{A}^*} \frac{\partial \hat{A}^*}{\partial m_{i,k}} + \frac{\partial U}{\partial m_{i,k}} = 0$$

Using (3.8), the derivatives $\frac{\partial U}{\partial \hat{A}^*}$ and $\frac{\partial U}{\partial m_{i,k}}$ at $\hat{A}^* = A^*$, $m_{i,k} = \tilde{g}_{i,k}(A^*)$ are obtained as

$$\left. \frac{\partial U}{\partial \hat{A}^*} \right|_{\hat{A}^*=A^*, m_{i,k}=\tilde{g}_{i,k}(A^*)} = 2S^{-1} \sum_{i,k} \left| \frac{\partial \tilde{g}_{i,k}}{\partial A}(A^*) \right|^2$$

$$\left. \frac{\partial U}{\partial m_{i,k}} \right|_{\hat{A}^*=A^*, m_{i,k}=\tilde{g}_{i,k}(A^*)} = -2S^{-1} \frac{\partial \tilde{g}_{i,k}}{\partial A}(A^*),$$

which yields

$$\partial_{i,k}\hat{A}^* = \frac{\frac{\partial\tilde{g}_{i,k}}{\partial A}(A^*)}{\sum_{j,l}\left|\frac{\partial\tilde{g}_{j,l}}{\partial A}(A^*)\right|^2}. \quad (3.14)$$

Thus, (3.12) can be written as

$$E\left(\hat{A}^* - E(\hat{A}^*)\right)^2 \approx \frac{\sigma^2}{\sum_{i,k}\left|\frac{\partial\tilde{g}_{i,k}}{\partial A}(A^*)\right|^2}$$

For identical biosensors in the array, the multi-compartment model comprises similar sets of ODEs on the biosensors, described by (2.15)-(2.16), where the only distinction among them is the input concentration A_i . Therefore, for all the biosensors, the response is the same function of the corresponding outer compartment concentration. The response of biosensor i at time t for the concentration A_1 at the inlet of the flow chamber can be expressed as

$$\tilde{g}_i(A_1, t) = \tilde{g}(A_i, t - \tilde{t}_i), \quad (3.15)$$

where $\tilde{g}(A_i, t)$ is the response of a single biosensor with concentration A_i in its associated outer compartment obtained by (2.12)-(2.14). Recall that the time shift \tilde{t}_i in (2.19) is the response delay of biosensor i . Using (3.15) and the recursion (2.17), the finite sample variance using N biosensors and S time samples is obtained as (3.6). Similarly by taking the second derivative of (3.9) and using (3.14), $\partial_{i,k}^2\hat{A}^*$ is obtained as

$$\partial_{i,k}^2\hat{A}^* = \frac{2\frac{\partial\tilde{g}_{i,k}}{\partial A}(A^*)\frac{\partial^2\tilde{g}_{i,k}}{\partial A^2}(A^*)}{\left[\sum_{j,l}\left|\frac{\partial\tilde{g}_{j,l}}{\partial A}(A^*)\right|^2\right]^2} - 3\left|\frac{\partial\tilde{g}_{i,k}}{\partial A}(A^*)\right|^2\frac{\sum_{j,l}\frac{\partial\tilde{g}_{j,l}}{\partial A}(A^*)\frac{\partial^2\tilde{g}_{j,l}}{\partial A^2}(A^*)}{\left[\sum_{j,l}\left|\frac{\partial\tilde{g}_{j,l}}{\partial A}(A^*)\right|^2\right]^3}$$

By substituting the derivatives from (3.14) and using the above equation, (3.13) can be rewritten as

$$E\left(\hat{A}^* - A^*\right) = O(e^2) + O(\sigma^2)O(e) + O(\sigma^4) \\ + \frac{\sum_{i,k} e_{i,k}(A^*) \frac{\partial \tilde{g}_{i,k}(A^*)}{\partial A}}{\sum_{i,k} \left| \frac{\partial \tilde{g}_{i,k}(A^*)}{\partial A} \right|^2} - \frac{\sigma^2 \sum_{i,k} \frac{\partial \tilde{g}_{i,k}(A^*)}{\partial A} \frac{\partial^2 \tilde{g}_{i,k}(A^*)}{\partial A^2}}{2 \left[\sum_{i,k} \left| \frac{\partial \tilde{g}_{i,k}(A^*)}{\partial A} \right|^2 \right]^2}.$$

Using (3.15) and the recursion (2.17), the bias is derived as (3.7).

3.3 Estimation Results for an Array of Ion Channel Switch Biosensor

In this section, the multi-compartment model of Section 2.2.2 is used to estimate analyte concentration in the example of the ICS biosensor array given in Chapter 2. Numerical examples for estimating the concentration A^* are provided. Here, the analytical results of Section 3.2 for the ICS biosensor array is compared with the corresponding simulated results. The attainable improvement in the estimate based on the number of biosensors is also evaluated.

The variance and bias of the finite-sample estimator \hat{A}^* (3.1) are estimated by Monte Carlo simulations and then compared with the values approximated by (3.6) and (3.7). The standard deviation and bias of \hat{A}^* for different number of biosensors are shown in Table 3.1. The estimate is obtained with $S = 300$ time samples with sampling rate 1 sample/s. The actual value of the initial concentration is $A^* = 10^{-8}$ Mol/m³. The noise variance σ^2 is set at $\sigma^2 = 0.1\bar{D}(0)$, where $\bar{D}(0)$ is the initial dimer concentration. Table 3.1 shows that the estimation variance, is decreasing faster than $1/N$ as N increases. The reason is that

the variance in (3.6) can be written as $E\left(\hat{A}^* - E(\hat{A}^*)\right)^2 = \sigma^2 / \sum_{i=1}^N d_i$, where

$$d_i = \alpha^{2i-2} \sum_{k=1}^S \left| \frac{\partial \tilde{g}}{\partial A}(\alpha^{i-1} A^*, t_{i,k} - \tilde{t}_i) \right|^2 \quad (3.16)$$

is increasing with i for $i \in \{1, \dots, N\}$. In order to justify this, the variations of the response $\tilde{g}(A, t) = F(\bar{\mathbf{u}}_1(t))$, obtained by the two-compartment model (2.12)-(2.14) with $A_1 = A$, is investigated here. Fig.3.1 illustrates the response of ICS biosensor $\tilde{g}(A, t)$ versus the concentration A of target molecules in the outer compartment. It can be seen that the response curve has the form of the sigmoid function and saturates for low and high concentration. As a result, there exists a concentration $A_c(t)$ for each time instant t such that in the range $A > A_c(t)$, the response $\tilde{g}(A, t)$ is convex in A . Therefore, the derivative $\partial \tilde{g}(A, t) / \partial A$ is increasing. Since $\partial \tilde{g}(A, t) / \partial A$ is negative, $[\partial \tilde{g}(A, t) / \partial A]^2$ is decreasing in A for $A > A_c(t)$. Assume that the sampling time points $t_{i,k}$ for each biosensor are selected such that the time difference $\tilde{t}_{i,k} = t_{i,k} - \tilde{t}_i$ in (3.6) is constant with i and is equal to t_k for $i \in \{1, 2, \dots, N\}$. Define $H(A)$ as $H(A) = \sum_{k=1}^S [\partial \tilde{g}(A, t_k) / \partial A]^2$. Then, there is a concentration A_c^* such that in the range $A > A_c^*$, $H(A)$ is decreasing. Then, d_i , defined in (3.16), can be written as $d_i = \alpha^{2i-2} H(\alpha^{i-1} A^*)$. If $A > A_c^*$, due to the decreasing behaviour of $H(A)$ in A , d_i has the possibility to be increasing in i . In order to explain the ascending behaviour of d_i in the results of this section, $H(A)$ and $\alpha^2 H(\alpha A)$ are compared in Fig.3.2 for the given example. From the experimental values of the parameters, α in (2.17) is obtained as $\alpha = 0.82$. The number of time samples in computation of $H(A)$ is $S = 300$ and the sampling rate is 1 sample/s. Fig.3.2 shows that there exist a range (A^m, A^n) such that for $A \in (A^m, A^n)$

$$\alpha^2 H(\alpha A) > H(A), \quad H(A) = \sum_{k=1}^S [\partial \tilde{g}(A, t_k) / \partial A]^2. \quad (3.17)$$

If $A^*, \alpha^{N-2}A^* \in (A^m, A^n)$, then, according to (3.17), it can be written that $d_{i+1} > d_i$ for $i \in \{1, \dots, N\}$. Therefore, based on the expression (3.6) for variance, using N biosensors decreases the estimation variance to less than $1/N$ of the variance obtained with a single biosensor.

If $A^* \in (A^m, A^n)$, depending on the values of α , A^* , and A^m , there exists an integer N^* such that for $2 \leq N \leq N^*$, we have $\alpha^{N-2}A^* \in (A^m, A^n)$. Since $A^* \in (A^m, A^n)$, the maximum threshold N^* exists and is greater than or equal to 2. An expression for N^* can be obtained as

$$N^* = \left\lfloor \log_{\alpha} \frac{A^m}{A^*} \right\rfloor + 2, \quad (3.18)$$

where A^m is defined in (3.17), A^* is the concentration of target molecules at the inlet of the flow chamber, and α is defined in (2.17). In (3.18), $\lfloor x \rfloor$ is the floor function that maps x to the largest integer that is not greater than x . For the given value of A^m in Fig.3.2, the initial concentration $A^* = 10^{-8}\text{Mol/m}^3$, and $\alpha = 0.82$, the value of N^* is obtained as $N^* = 4$. From what described above, if $A^* \in (A^m, A^n)$, using $2 \leq N \leq N^*$ biosensors decreases the estimation variance to less than $1/N$ of the variance obtained with a single biosensor.

The results for the estimation bias in Table 3.1 show that the magnitude of the bias is increasing with N for $N = 1, 2, 3$ biosensors and then it decreases at $N = 4$. This behaviour can be explained by tracking the changes of the two separate terms in the evaluation of bias in (3.7). The first term on the right-hand side of (3.7) depends on the deterministic error $e_{i,k}$ between the PDE response and the response of the multi-compartment model, whereas the second term depends on the variance σ^2 of the random measurement noise. For the given example, the values of these terms are evaluated separately for $N = 1, 2, 3, 4$ in Table 3.2. As it can be seen, the second term in (3.7) is positive and decreasing with the number of

biosensors. The second term is positive because, as explained earlier, the first derivative $\frac{\partial \tilde{g}(A,t)}{\partial A}$ is negative and the second derivative $\frac{\partial^2 \tilde{g}(A,t)}{\partial A^2}$ is positive due to the convexity of the response $\tilde{g}(A,t)$. The denominator of the second term is increasing with the number of biosensors, as explained before, and it is increasing much faster than the numerator. The first term on the right-hand side of (3.7) is negative. In order to justify its variations, the deterministic error $e_{i,k}$ should be evaluated. The sampled error $e_{i,k} = e_i(t_{i,k})$ is the absolute error between the PDE and the multi-compartment responses at time samples $t_{i,k}$. The variations of the absolute error $e_i(t) = \bar{D}_i(t) - \bar{D}_i^{\text{ODE}}(t)$ are plotted in Fig.3.3. Since the value of $e_i(t)$ for the biosensors $i = 1, 2, 3$ is positive and the first derivative $\frac{\partial \tilde{g}(A,t)}{\partial A}$ is negative, the first term in (3.7) is negative for $N = 1, 2, 3$. For $i = 1, 2, 3$, the error $e_{i,k}$ have the same sign and are increasing in magnitude. Therefore, they add to the magnitude of the first term in (3.7). The error $e_4(t)$ and its time samples $e_{4,k}$, on the other hand, is negative in some parts. This results in reducing the magnitude of the first term in (3.7). It can also be seen than the first term dominates the second term in (3.7) for $N = 2, 3, 4$. With the above explanation, it can be concluded that the estimation bias depends tightly on the multi-compartment approximation error. The bias can fluctuate due to the change in sign and magnitude of this error.

3.4 Summary

In this chapter, we estimated the injection analyte concentration A^* at the inlet of the flow chamber (2.1 using multiple surface-based biosensors embedded in the flow chamber. The dynamics of analyte flow and the surface capture of analytes along with the other reactions on the biosensors are described by the PDE model (2.2)-(2.7). We use the approximate multi-compartment ODE model, developed in Chapter 2, to solve the estimation problem. The results of this chapter can be summarized as:

Table 3.1: Comparison between the simulated and approximate values for the variance and bias of the estimate \hat{A}^* obtained by (3.1): The simulated and analytical values of the standard deviation and normalized bias for $S = 300$ time samples are shown. The sampling rate is 1 sample/s. The target molecule concentration at the inlet of the flow chamber is $A^* = 10^{-8}$ Mol/m³. The noise variance is set at $\sigma^2 = 0.1\bar{D}(0)$, where $\bar{D}(0)$ is the value of the response at $t = 0$.

	$\sqrt{E\left(\hat{A}^* - E(\hat{A}^*)\right)^2}/A^*$		$E\left(\hat{A}^* - A^*\right)/A^*$	
	Simulated	Analysis (3.6)	Simulated	Analysis (3.7)
N=1	0.095	0.094	0.002	0.003
N=2	0.064	0.065	-0.022	-0.021
N=3	0.05181	0.05185	-0.028	-0.029
N=4	0.043	0.044	-0.0267	-0.0270

Table 3.2: The variations of the first and second terms on the right-hand side of (3.7) for the results of Table 3.1.

	First term in (3.7)	Second term in (3.7)	Total bias (3.7)
N=1	-0.004	0.007	0.003
N=2	-0.024	0.003	-0.021
N=3	-0.031	0.002	-0.029
N=4	-0.028	0.001	-0.027

1. The initial concentration A^* at the inlet of a flow chamber can be estimated with the ICS biosensor array using the multi-compartment model. According to the results for the estimation bias and variance in Table 3.1, using an array of four sensors reduces the estimation error from 10% to 5% in terms of the root mean squared error. The estimation is based on 300 measurement samples on each biosensor during the first 300 seconds of the response.
2. When the initial concentration A^* is in a certain range, the estimation variance can be reduced to less than $1/N$ by using N biosensors. This nonlinear effect is not specific to the given example and can occur in any estimation problem using a sensor

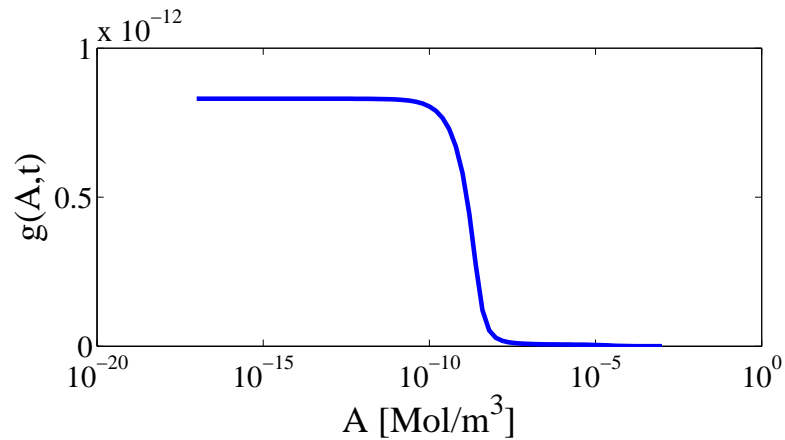
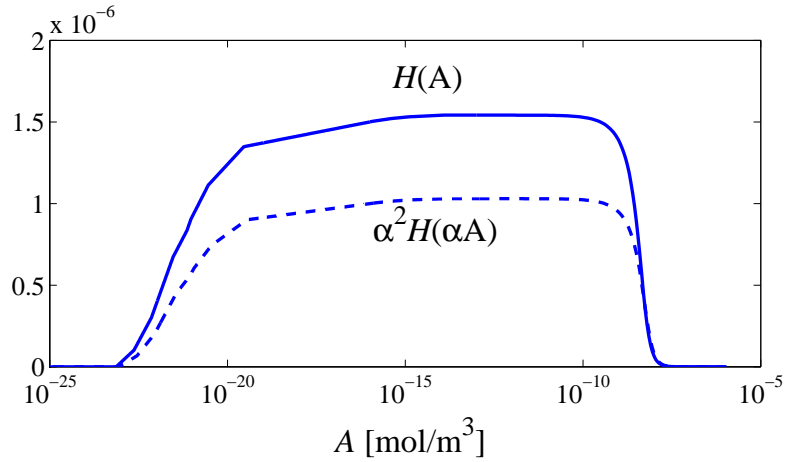


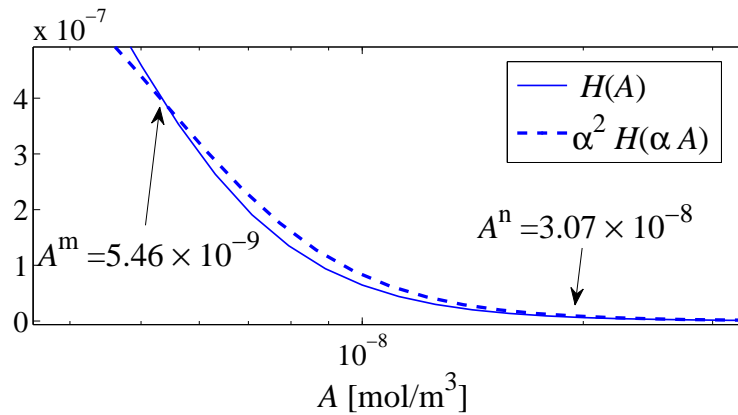
Figure 3.1: The response $\tilde{g}(A, t) = F(\bar{\mathbf{u}}_1(t))$ of a single biosensor, obtained by the two-compartment model (2.12)-(2.14) with $A_1 = A$, is insensitive to low concentrations of target molecules. By increasing the concentration of target molecules, the sensitivity of $\tilde{g}(A, t)$ (the magnitude of the derivative $\partial\tilde{g}(A, t)/\partial A$) initially increases and then decreases to zero for large values of concentration. The response is plotted for a time horizon of 300s.

array, where the sensor response is nonlinear in terms of the unknown quantity. Due to the measurement effect on the system state or time and space variations of the process under measurement, identical sensors in an array can function in different operating points with different sensitivities. Consider a single sensor in such a system. If another sensor is added such that it operates with a higher sensitivity compared to the previous one, the estimation variance is reduced to less than half.

3. The measurement error in the developed multi-compartment model comprises a white noise, which includes the PDE modeling error and the measurement noise, and a deterministic error between the responses of the multi-compartment model and the PDE model. According to (3.12), the contribution of the deterministic error to the estimation variance is insignificant compared to the random noise. The estimation bias is however dependent on both the deterministic error and the noise variance. The deterministic error is a result of the multi-compartment approximation. This error is due to discretization and is inevitable in numerical methods for solving estimation



(a)



(b)

Figure 3.2: The ascending behaviour of d_i , defined in (3.16), is investigated by comparing $H(A)$ and $\alpha^2 H(\alpha A)$ (a), where $H(A)$ is defined in (3.17). The plot in the interval $A \in (A^m, A^n)$ is magnified (b). For the value of A in this interval, we have $\alpha^2 H(\alpha A) > H(A)$. In our example of the estimation problem, the concentration at the inlet of the flow chamber $A^* = 10^{-8} \text{ Mol/m}^3$ belongs to this interval. Using $N \leq N^* = 4$ biosensors, for N^* obtained by (3.18), the variance of the estimation is decreased to less than $1/N$ of the variance obtained by a single biosensor.

problems in PDE models.

4. The estimation bias is mainly influenced by the multi-compartment approximation error. The bias can fluctuate with the number of biosensors if the magnitude and

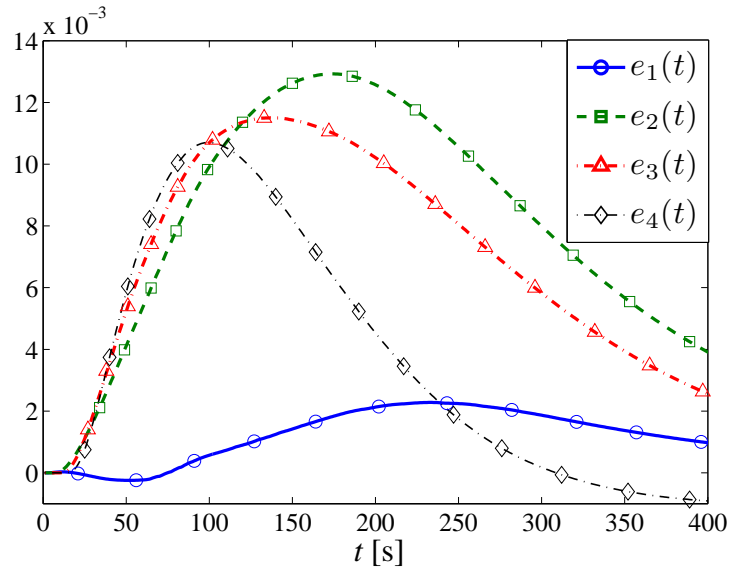


Figure 3.3: The absolute error $e_i(t) = \bar{D}_i(t) - \bar{D}_i^{\text{ODE}}(t)$ between the responses of the PDE model (2.2)-(2.7) and the multi-compartment ODE model (2.15)-(2.19) for $A^* = 10^{-8}$ Mol/m³. The flow rate is $Q = 10$ μ L/min. The number of biosensors is $N = 4$. The biosensor length and spacing are respectively $L = 2$ mm $d = 1$ mm.

sign of this error fluctuate with the number of biosensors.

5. Using the developed multi-compartment ODE model provides an insight into the dynamical behaviour of the biosensors and significantly reduces the amount of computation for the estimation problem. Using this model enables the evaluation of estimation bias and variance via an analytic expression, which can also determine how the parameters in the system influence these values.

Chapter 4

Improved Analyte Collection Rate by Using Multiple Sensors

In the previous chapter, we solved the concentration estimation problem and investigated the estimation improvement based on the number of biosensors used for measurements. Using an array of biosensors, the estimation improvement depends on the sensitivity of individual biosensors to the input concentration. We investigated how the biosensor sensitivity to the injection concentration changes with the biosensor position in the array along the flow direction. In this chapter, we focus on improving the detection of target molecules rather than estimating their concentration. We combine the measurements of multiple sensors to form a response that is stronger than that of a single sensor with the same total sensing surface area. The stronger output response improves detection probability of small target molecule concentrations.

Consider a single surface-based sensor for detection of analytes in the flow chamber. When the binding kinetics are mass-transport limited, the capture rate of analyte at this surface is faster than passive diffusion can replenish. Most of the analyte molecules are captured close to the entry port of the flow chamber. If a single large sensing surface is used, depletion of analyte occurs downstream within the flow chamber. At these downstream areas, capture of analyte at the sensor surface is delayed until the analyte depletion near the entry port is saturated. This results in the sensor response rate slower than determined by the analyte-receptor reaction rates at the sensor surface. Fig.4.1(a) illustrates the depletion

effect for a flow chamber of capillary height h and analyte concentration A^* (the sensor and its parameters are specified in Section 4.2 for an ion channel switch biosensor). This chapter proposes replacing a single surface-based sensor by an array of spaced smaller sensors with the same total sensing surface area for detection of minute concentrations (nano to pico-molar) of analyte in a fluid flow chamber. A minute analyte concentration (MAC) is defined as a concentration where the intermolecular spacing of the analyte is greater than the passive diffusion distance undergone by the analyte during the sensor response time. It is shown that in the mass-transport influenced case, when the transport rate of analyte is comparable to or smaller than the intrinsic reaction rates at the sensor surface, substantial improvements in the response rate can be obtained from the array relative to the initial single large surface. Formulas are derived to support our hypothesis for quantifying the improvement in performance and optimal size of the sensors in the array. We present a quantitative design in which the sensor response rate is optimized at MAC levels of analyte by replacing a single sensor of area A with an array of N sensors of area $\frac{A}{N}$. The space between the sensors permits analyte to be replenished between the individual elements in the array (as shown in Fig.4.1(b)). When optimized, the analyte capture rate per unit area on the array is substantially improved. The results of our analysis are compared with experimental data obtained for an ICS biosensor and a surface plasmon resonance biosensor. A sensing array can enhance the total analyte collection rate by mitigating the mass-transport limitations on the binding kinetics of a reactive surface outlined in Chapter 1. As described in Chapter 1, Squires et al have explored the mass-transport effects on the kinetics of a surface-based sensor [1]. Based on this analysis, an explicit expression is derived in this chapter to quantify the total analyte collection rate on multiple sensors. Based on the constructed PDE model in Chapter 2, we validate our analytical results using the numerical solutions of the PDE.

Table 4.1: Maximum attainable improvement in analyte collection rate, defined in (4.4), for two real-life biosensors; The ion channel switch biosensor (a) and the BIACORE biosensor (b). The improvement is obtained by replacing a single sensor with a uniform array of N smaller sensors of similar type. The analyte injection concentration is $A^* = 1\text{pM}$ (a) and $A^* = 25\text{nM}$ (b). The total length of the sensors in each array is $L = 2\text{mm}$ (a) and $L = 1\text{mm}$ (b), which is equal to the length of the initial single sensor. The sensor spacing is considered to be sufficiently large in each case to allow the analyte concentration to reach its maximum value in the gaps between the sensors. (Parameters are specified in Section 4.2 and Section 4.3 and their values for the initial single sensor are given in Table 4.2 and Table 4.3.)

(a)				
	Sensor length (mm)	Damkohler number D_i (for sensor i)	Collection rate improvement $\left(J^{-1} \sum_{i=1}^N J_i - 1\right)$ (%) compared to one sensor	
			Numerical	Analysis (4.4)
$N = 2$	1	1.82	11.86	11.78
$N = 4$	0.5	1.44	24.20	25.07
$N = 5$	0.4	1.34	27.94	29.55

(b)				
	Sensor length (mm)	Damkohler number D_i (for sensor i)	Collection rate improvement $\left(J^{-1} \sum_{i=1}^N J_i - 1\right)$ (%) compared to one sensor	
			Numerical	Analysis (4.4)
$N = 2$	0.5	2.41	15.50	17.85
$N = 5$	0.2	1.77	35.67	44.23

The main results of this chapter are stated as follows:

1. In Section 4.1, a formula is derived for characterizing the improvement of multiple sensors compared to a single sensor in the mass-transport influenced case.
2. Numerical studies and experimental data are compared to validate the predictive model. The results for two case-studies, an ICS biosensor and a surface plasmon resonance biosensor, are illustrated in Table 4.1. The results show that using multiple sensors can increase total analyte collection rate by more than 11% in these examples

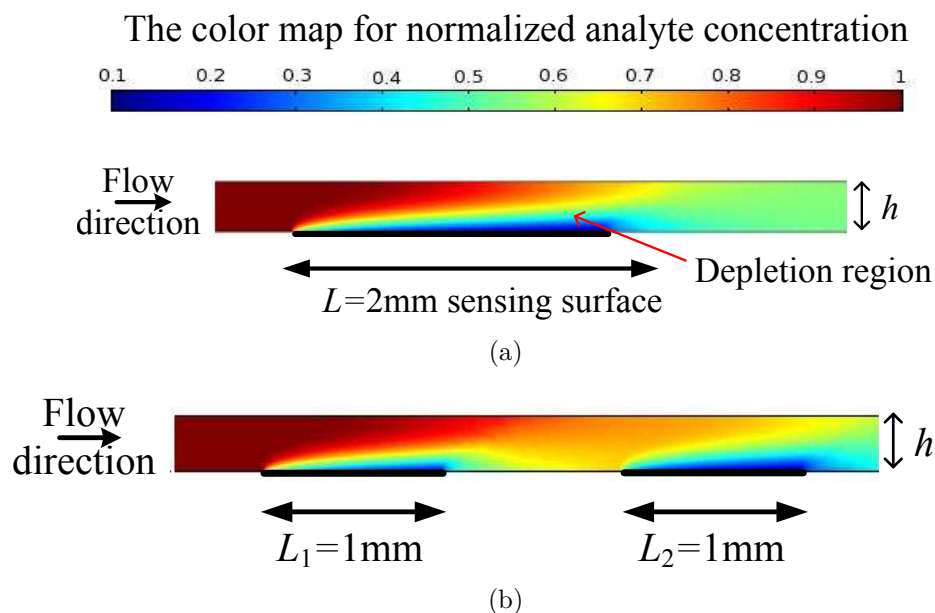


Figure 4.1: Depletion in analyte concentration along a sensor. (a): The analytes are bound close to the entry to the flow chamber causing a depletion in analyte concentration for subsequent binding sites and an overall slowing of the sensor response. (b): Replacing the sensor with two spaced out half-sized sensors allows analyte to be replenished between the individual sensors.

compared to a comparable single sensing area. Also the tables show that the formula we derive for predicting the performance improvement fits remarkably accurately to the actual performance improvement. By analyte collection rate on a sensing surface, we mean the surface integral of inward analyte diffusive flux on the surface.

4.1 Multiple-Sensor Array can Mitigate Mass-Transport Limits

Binding kinetics on a sensor are influenced by finite reaction rates and the transport rate of analytes to the surface. Due to mass-transport limitations, a depletion region is formed on the sensor surface which hinders the analyte transport to further parts on the sensor. Using

an array of multiple smaller sensors can change the mass-transport limitations on total analyte collection rate. Section 4.1.1 specifies the mass-transport and kinetics conditions where the total analyte collection rate can be higher on an array of multiple sensors than a single sensor with the same total sensing surface area. Then, in Section 4.1.2, the analyte collection rate on a single sensor is compared to a multiple-sensor array, where the total sensing area is fixed. A formula is derived for the attainable improvement in analyte collection rate.

4.1.1 Binding Kinetics in the Mass-Transport Phase Diagram

Based on the classification of mass-transport conditions and different binding kinetics conditions introduced in Chapter 1, this section specifies those conditions where multiple-sensor array can improve analyte collection rate.

Recall the classification of different binding kinetics based on the value of the dimensionless Damkohler number in Chapter 1. When $D_a \ll 1$, the reactive flux is much smaller than the diffusive flux and the binding kinetics are reaction-limited. When D_a increases to values greater than 1, the kinetics start to become mass-transport influenced. The kinetics become mass-transport limited when $D_a \gg 1$ [39]. In order to benefit from splitting the sensing area, the kinetics conditions should be mass-transport influenced, i.e. the Damkohler number D_a should be sufficiently large. Using multiple sensors in the reaction-limited regime is irrelevant because distributed placement of the sensing surfaces can only influence the transport rate of analyte to the sensor.

While the Damkohler number determines the binding kinetics regime, the mass-transport condition is determined by the Péclet number and the dimensionless length of the sensor. Different mass-transport regions are classified in Fig.1.2 in Chapter 1, based on these values. When the Péclet number is too small or the sensor is too long, the sensor grabs all

the analytes delivered by the flow. Region (i) in the phase diagram in Fig.1.2 corresponds to this full collection regime, where the analyte collection rate on the sensor is equal to the input advective flux. This region is not interesting to the method of splitting the sensing area since the collection rate is already at its maximum level and cannot exceed the input advective flux.

Using an array of multiple sensors can increase total analyte collection rate in region (ii) and (iii) in the phase diagram in Fig.1.2. Region (iii) is not in the scope of this thesis. We focus on region (ii) in the phase diagram since the experimental values of the parameters in our case-studies (Section 4.2 and Section 4.3) belong to this region.

Consider the flow chamber (2.1) described in Chapter 2 with only a single sensor in the chamber. As described in Chapter 2, the steady-state diffusive flux on a sensor with length L and width w_s is approximated as $J = \gamma L w_s \nabla A$, where γ is the analyte diffusion constant. Here, the analyte concentration gradient ∇A on the surface is approximated by $\nabla A = \frac{A^* - a(t)}{\delta}$ where δ is the thickness of the depletion region and $a(t)$ is the analyte concentration just above the sensor surface in the depleted region. For the mass-transport conditions in region (ii) of the mass-transport phase diagram in Fig.1.2, δ is obtained by (2.10). In the mass-transport limited regime, it is assumed that the sensor has infinite binding capacity. Therefore, the region above the sensor is completely depleted yielding $a(t) = 0$. The mass-transport limited diffusive flux is thus obtained as (1.7). For finite reaction rates on the sensor, the two extremes on the analyte collection rate given by the mass-transport limit and the reaction-rate limit balance the steady-state analyte collection rate to [1, 61]

$$J = A^* w \gamma F \frac{D_a}{1 + D_a}, \quad F \approx 1.47 P_{eH}^{1/3} \lambda^{2/3}, \quad (4.1)$$

where A^* is the analyte injection concentration as described in (2.4), w is the width of the

sensor, and γ is the diffusion constant. In the computation of F , the Péclet number P_{eH} is defined in (1.6), and $\lambda = L/h$ is the ratio of the sensor length to the height of the flow chamber. Using (1.4) and (1.7) in Chapter 1, the Damkohler number D_a is obtained as

$$D_a = \frac{Lk_{on}\theta}{\gamma F}, \quad (4.2)$$

where k_{on} is the forward reaction rate, θ is the total binding site concentration on the sensor, and F is obtained in (4.1).

Note that by "steady-state analyte collection rate", we mean the analyte collection rate at the time when the depletion zone on the sensor evolves quasi-steadily. The quasi-steady state occurs if the time it takes the sensor to achieve equilibrium is much greater than the time for the depletion region to form [1]. Throughout this thesis, it is assumed that the depletion region on the sensor achieves a quasi-steady state. The provided examples also satisfy this condition.

4.1.2 Improving Analyte Collection Rate Using Multiple Sensors

This section demonstrates that mass-transport limits on analyte collection rate can be mitigated by using an array of multiple sensors instead of a single sensor of the same total sensing surface area. Firstly, an expression is derived for the total analyte collection rate on each individual sensor in a linear array of surface-based sensors. Then, having the total sensing area fixed, the sum of collection rates on all the sensors is maximized versus the size of the individual sensors.

Consider a linear array of N sensors with dimensionless lengths $\lambda_1, \lambda_2, \dots, \lambda_N$ along the flow direction in the flow chamber described in Section 2.1 of Chapter 2. The sensors are

operating in region (ii) of the phase diagram in Fig.1.2, under a mass-transport influenced condition. It is assumed that the sensors are sufficiently spaced out in the flow chamber such that the quasi steady-state analyte concentration in the gaps between the sensors achieves its maximum.

Maximum attainable improvement in the steady-state analyte collection rate based on multiple-sensor measurements:

Consider replacing a single sensor with the array described above while the total sensing surface area is fixed. The sensors have the same width w equal to the width of the flow chamber. The total dimensionless length of the sensors in the array can thus be written as $\sum_{i=1}^N \lambda_i = \lambda$, which is equal to the length of the initial single sensor. The following results will be derived:

Result I: The steady-state analyte collection rate J_i on sensor i for $i = 1, 2, \dots, N$ can be obtained as

$$J_i \approx w\gamma A_i F_i \frac{D_{ai}}{1 + D_{ai}}, \quad A_i = \left(1 - \frac{F_{i-1} D_{ai-1}}{P_{eH} (1 + D_{ai-1})}\right) A_{i-1}, \quad (4.3)$$

where w is the width of the flow chamber, γ is the diffusion constant, and P_{eH} is the Péclet number obtained by (1.6). The dimensionless flux F_i on sensor i is obtained by replacing λ with λ_i in (4.1). Similarly, the Damkohler number D_{ai} of sensor i is obtained by (4.2) for the corresponding length L_i and dimensionless flux F_i . Here, we define $F_0 = 0$, and $A_0 = A^*$, where A^* is the analyte injection concentration defined in (2.4).

Result II: The improvement in analyte collection rate, obtained by replacing a single sensor with an array of spaced sensors, can be defined as $J^{-1} \sum_{i=1}^N J_i - 1$, where J is the analyte collection rate on the initial single sensor obtained by (4.1). The maximum value of the defined improvement with respect to the values of the length of the array sensors is obtained as

$$\max_{\lambda_1, \dots, \lambda_N, \sum_{i=1}^N \lambda_i = \lambda} J^{-1} \sum_{i=1}^N J_i - 1 \approx \frac{1 + D_a}{k D_a} - \frac{1 + D_a}{k D_a} \left(1 - \frac{N^{-2/3} k D_a}{N^{1/3} + D_a} \right)^N - 1, \quad (4.4)$$

where k is defined as

$$k = 1.47 P_{eH}^{-2/3} \lambda^{2/3}, \quad (4.5)$$

and D_a is the Damkohler number of the initial single sensor obtained by (4.2).

Derivation of (4.3) and (4.4): According to (4.1), examining the validity of (4.3) for the first sensor ($i = 1$) is straightforward. Its derivation for $i = 2, 3, \dots, N$ is based on induction. The steady-state analyte concentration A_2 above the second sensor can be computed by deducting the analyte collection rate J_1 on the first sensor from the input advective flux $J_C = A^*Q$. It is assumed that the sensors are sufficiently spaced out such that analyte can be replenished between the individual sensors. Therefore, the analyte concentration A_2 above the second sensor is obtained as $A_2 \approx \frac{1}{Q} (A^*Q - J_1)$. Using (1.6) and (4.3) to compute J_1 , A_2 can be obtained as $A_2 \approx A^* \left(1 - \frac{F_1 D_{a1}}{P_{eH} (1 + D_{a1})} \right)$. Similarly, the expression (4.3) for the steady-state analyte collection rate on any sensor in the array is derived by deducting the total collection rate on the previous sensors from the input convective flux. From (4.3), the flux J_i on sensor i can be obtained as

$$J_1 = J (1 + D_a^{-1}) \frac{\alpha_1}{\alpha_1^{1/3} + D_a^{-1}}, \quad (4.6)$$

$$J_i = J (1 + D_a^{-1}) \frac{\alpha_i}{\alpha_i^{1/3} + D_a^{-1}} \left(1 - k \frac{\alpha_{i-1}}{\alpha_{i-1} + D_a^{-1}} \right) \dots \left(1 - k \frac{\alpha_1}{\alpha_1^{1/3} + D_a^{-1}} \right), \quad i \geq 2,$$

where D_a is the Damkohler number on the original sensor defined in (4.2), and k , obtained by (4.5), is the ratio of the collection rate of the single sensor to the input convective

flux. In (4.6), α_i is the ratio of the length of biosensor i to the total length L , obtained as $\alpha_i = \lambda_i/\lambda$, where $\sum_{i=1}^N \alpha_i = 1$. It can be proved that there is a set of values for α_i or equivalently for λ_i such that the function $J^{-1}J_T = J^{-1} \sum_{i=1}^N J_i$ is greater than 1, which means that the total collection rate J_T on the sensor-array is greater than the collection rate J on the single sensor. The total collection rate $J_T = \sum_{i=1}^N J_i$ is symmetric with respect to α_i or λ_i for $i \in \{1, 2, \dots, N\}$. If it can be proved that the function $J^{-1}J_T$ is unimodal with respect to $0 \leq \alpha_i \leq 1$, $J^{-1}J_T$ will be greater than 1, under the constraint $\sum_{i=1}^N \alpha_i = 1$, for all values of α_i . Also it can be concluded that $J^{-1}J_T$ is maximized at the center of symmetry, where $\alpha_i = 1/N$. In this case, $J^{-1}J_T$ is greater than one for all values of λ_i . The proof of $J^{-1}J_T$ being unimodal is complicated. In fact, the simulation results show that the function would be unimodal for a certain range of k , defined in (4.5). It can be proved that for $N = 2$ and $D_a \gg 1$, the function $J^{-1}J_T$ is concave in the region $\alpha_1 + \alpha_2 = 1$ for $k \leq 3^{-1}2^{2/3} \approx 0.53$. Simulations show that for $N > 2$ and $D_a \gg 1$, this upper bound for k relaxes as N increases. Please note that k cannot exceed 1 since, from the definition, it is the ratio of the collection rate of the single sensor to the input convective flux.

For a large set of experimental values of P_{eH} and λ in region (ii) of the mass-transport phase diagram in Fig.1.2, the value of k belongs to the desired range. Thus, the maximum improvement in analyte collection rate is attained at the point where the sensors in the array have equal length. At this point, the total collection rate $J_T = \sum_{i=1}^N J_i$ is a finite geometric series with the common ratio $1 - \frac{N^{-2/3}kD_a}{N^{1/3}+D_a}$, where D_a is the Damkohler number for the initial single sensor and k is defined in (4.5). The maximum value of the defined improvement in (4.4) is then obtained by computing the value of the derived geometric series.

Taking the limit of (4.4) as D_a goes to infinity yields the maximum attainable improve-

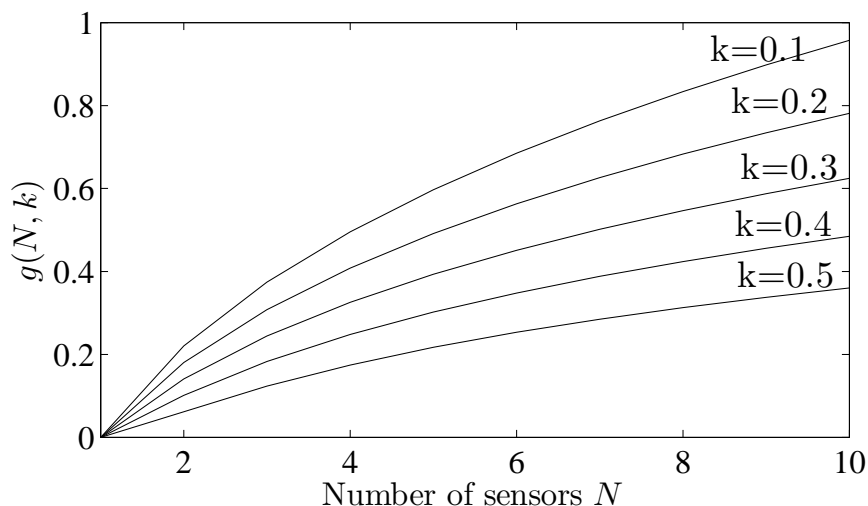


Figure 4.2: The variations of maximum improvement in analyte collection rate in the mass-transport limited regime, as defined in (4.7): The improvement is based on replacing a single sensor with N sensors while the total sensing area is fixed. The parameter k , defined in (4.5), is the ratio of the analyte collection rate on the single sensor to the input advective flux. By increasing the value of k , the attainable improvement in analyte collection rate reduces.

ment in analyte collection rate in a mass-transport limited regime denoted by $g(k, N)$:

$$g(k, N) = k^{-1} - k^{-1} \left(1 - \frac{k}{N^{2/3}} \right)^N - 1. \quad (4.7)$$

Here k is defined in (4.5) and N is the number of sensors in the array. Fig.4.2 shows how $g(k, N)$ changes with the number of sensors N for different values of k . The results show that for a fixed number of sensors, the improvement in analyte collection rate increases as k decreases.

In the above discussion, the sensors are assumed to be sufficiently spaced out to allow the quasi-steady analyte concentration to achieve its maximum in the gaps between the sensors.

4.2 Case-Study I: Ion Channel Switch Biosensor

In this section, the PDE model of Section 2.1 together with the analysis of Section 4.1 are used to predict the behavior of an ICS biosensor. The PDE model and the reaction equations for an array of ICS biosensors are described in Section 2.3.1. We provide numerical results that quantify the improvement obtained by using multiple ICS biosensors compared to a single biosensor. Numerical values of the improvement in analyte collection rate are compared with the analysis in (4.4). Numerical results are obtained by solving the PDE model (2.2)-(2.7) using the COMSOL multi-physics simulation software. In order to demonstrate that the PDE model (2.2)-(2.7) is an accurate model, the single biosensor response predicted by the PDE model is compared with the one generated by a computer model, called Sensim, that is included in the ICS analysis package. This model simulates the binding experiments on the ICS biosensor.

The experimental parameter values for streptavidin-biotin interaction on a single ICS biosensor are given in Table 4.2 [43]. The values of the Péclet number and the dimensionless length of the single sensor belong to region (ii) in the mass-transport phase diagram in Fig.1.2. The value of the Damkohler number $D_a = 2.29$ is obtained by (4.2), where $k_{on} = f_1$ and $\theta = B^* + C^*$. Since this value is greater than one, the biosensor operates in a mass-transport influenced regime. The single biosensor in the flow chamber is replaced with a linear array of multiple biosensors while the total sensing surface area is fixed. The biosensors are connected in parallel in the external circuit such that the measured output current is the sum of the currents of all biosensors. The variations of total conductance of the biosensors are recorded as the array response.

Table 4.1(a) illustrates the improvement in analyte collection rate defined in (4.4). The numerical results are compared with the analytical expression (4.4) for uniform arrays of $N = 2$, $N = 4$, and $N = 5$ biosensors. The total length of the biosensors in the array is

Table 4.2: Parameter values for streptavidin-biotin interaction on ICS biosensor

Chamber and biosensor dimensions	
Sensor length L (mm)	2
Chamber width W (mm)	3
Chamber height h (mm)	0.1
Primary species concentration	
Binding site B^* (molecules/cm ²)	1×10^{11}
Free monomers C^* (molecules/cm ²)	1×10^9
Tethered monomers S^* (molecules/cm ²)	1×10^{10}
Reaction rate constants	
$f_1 = f_2 = f_6$ (M ⁻¹ s ⁻¹)	8×10^6
$f_3 = f_4$ (cm ² molecule ⁻¹ s ⁻¹)	5×10^{-9}
$f_5 = f_7$ (cm ² molecule ⁻¹ s ⁻¹)	1×10^{-10}
$r_1 = r_2 = r_3 = r_4 = r_6$ (s ⁻¹)	1×10^{-6}
$r_5 = r_7$ (s ⁻¹)	1.5×10^{-2}
Diffusion constant γ (cm ² s ⁻¹)	1.5×10^{-6}
Flow rate Q (μ L/min)	10
Dimensionless parameters	
Péclet number P_{eH}	370.37
Dimensionless sensor length $\lambda = \frac{L}{h}$	20
Damkohler number D_a	2.29
k : Ratio of the collection rate to the input flux	0.21

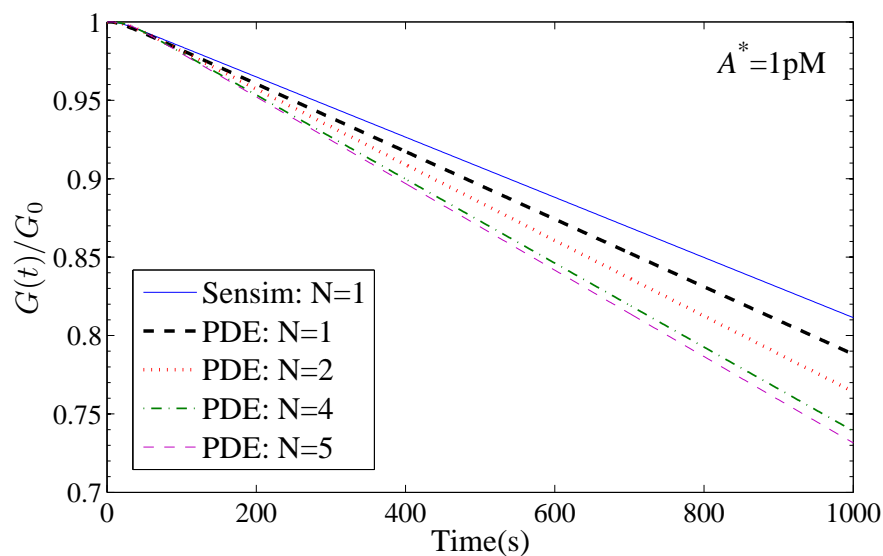
fixed and equal to the length of the single biosensor in Table 4.2. The sensor spacing is selected as five times the length of each biosensor in the array. Experiments show that this value allows the analyte concentration to reach its maximum value in the gaps between the biosensors. The analyte injection concentration is $A^* = 1\text{pM}$. The results show that the total analyte collection rate improves with the number of biosensors. Note that the kinetics conditions are transport-influenced because the values of the Damkohler number for each sensor is greater than one.

Fig.4.3(a) compares the responses of the single biosensor and the multiple-biosensor arrays studied in Table 4.1(a). For a multiple ICS-biosensor array, the response is charac-

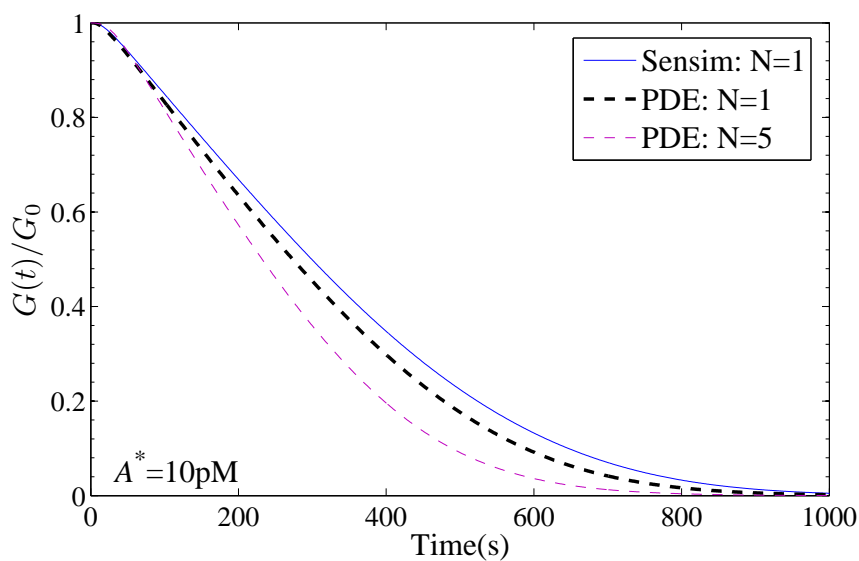
terized as the variations of normalized total conductance of the sensors, denoted by $\frac{G(t)}{G_0}$. G_0 denotes the initial conductance of the single biosensor, which is equal to the initial total conductance of the biosensor array. As mentioned earlier, the biosensors are connected in parallel in the external circuit. Therefore, their total conductance is measured in the external circuit. The selection of the parameter values in Table 4.2 together with the low analyte injection concentration $A^* = 1\text{pM}$ result in a linear sensor response. The response rate is proportional to the total analyte collection rate. Fig.4.3(b) shows similar results for the analyte injection concentration $A^* = 10\text{pM}$. The response is nonlinear with time because of higher analyte concentration.

4.3 Case-Study II: BIACORE Biosensor

In this section, a single BIACORE biosensor is replaced with a uniform linear array of BIACORE biosensors to quantify the improvement in analyte collection rate. BIACORE biosensor is an optical biosensor where the changes in the index of refraction is monitored as the analytes bind to the surface [92]. When there are multiple BIACORE sensors, one can take the average of the individual sensor responses. It will be shown that the average response of multiple BIACORE sensors is higher than the response of a single BIACORE sensor with the same total sensing surface area. The response of SPR-based biosensors are measured in resonance units (RU). One RU is approximately equivalent to a change of 10^{-10}g/cm^2 in mass on the surface when the analyte is a protein [88]. The experimental results for a single BIACORE biosensor are extracted from a work by Myszkka [88]. The binding data corresponds to an antigen-antibody interaction where the antigen is a soluble form of the human T-cell receptor (DID2) that attaches to a monoclonal antibody from IgG1 called mAb CE9.1 [53]. Analytes (the antigens) flow past a BIACORE biosensor with the parameter values given in Table 4.3. Table 4.1(b) compares the corresponding



(a)



(b)

Figure 4.3: The response of a uniform array of N ICS biosensors for different values of N . The total sensing surface area is fixed. All the biosensors have the same width and their total length is $L = 2\text{mm}$. Other parameter values are given in Table 4.2. The analyte injection concentration is $A^* = 1\text{pM}$ (a) and $A^* = 10\text{pM}$ (b). The sensor spacing $d = \frac{5L}{N}$ is five times the length of individual sensors in the array.

Table 4.3: Parameter values for the BIACORE biosensor

Chamber and biosensor dimensions	
Sensor length L (mm)	1
Chamber width w (mm)	3
Chamber height h (mm)	0.2
Receptor surface density	
Monoclonal antibody mAb CE9.1 (RU)	1400
Reaction rate constants	
k_{on} ($M^{-1}s^{-1}$)	1.2×10^6
k_{off} (s^{-1})	2.9×10^{-4}
diffusion constant γ (cm^2s^{-1})	1×10^{-6}
Flow rate Q ($\mu L/min$)	60
Dimensionless parameters	
Péclet number P_{eH}	3.33×10^3
Dimensionless sensor length $\lambda = \frac{L}{h}$	5
Damkohler number D_a	3.04
Ratio of the collection rate to the input flux k	0.02

analytical and numerical results for the attainable improvement. The numerical results are compared with the analysis in (4.4) for uniform arrays of $N = 2$ and $N = 5$ sensors. The sensor spacing is selected as approximately twice the length of each sensor in the array. Experiments show that for the given flow rate ($60\mu L/min$), this distance allows the analyte concentration to reach its maximum value in the gaps between the sensors. Due to higher flow rate in this example compared to the ICS biosensor in Section 4.2, the required sensor spacing is smaller here. The analyte injection concentration is $A^* = 25nM$ [88].

Fig.4.4 compares the responses of the BIACORE biosensor arrays studied in Table 4.1(b). The response of a sensor-array is characterized as the average of the responses of the individual sensors measured in resonance units. As mentioned earlier, the SPR response is used to detect changes in the index of refraction caused by mass changes on the sensor surface. The rate of change in the index of refraction is proportional to the change in the

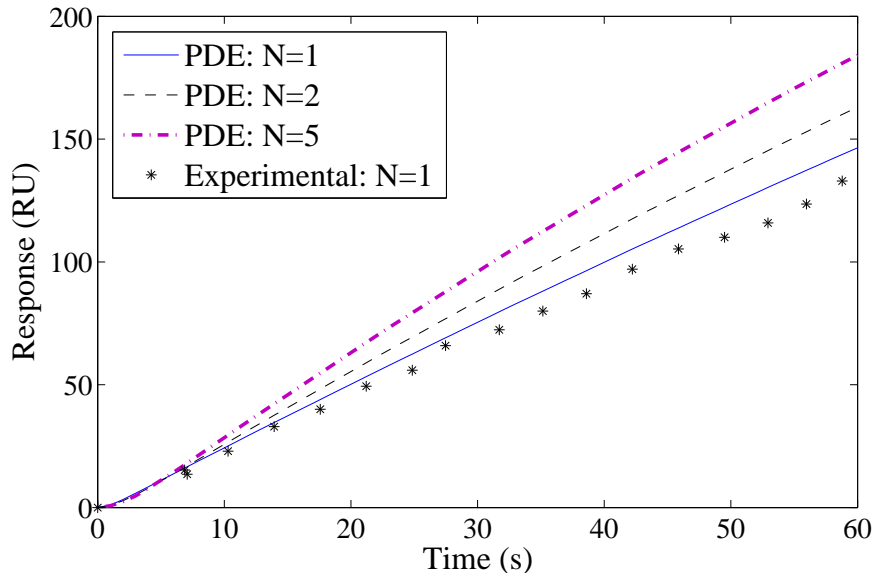


Figure 4.4: The response of a uniform array of N BIACORE biosensors for different values of N . The total sensing surface area is fixed. The total length of the biosensors is $L = 1\text{mm}$. Relevant parameter values are given in Table 4.3. The analyte injection concentration is $A^* = 25\text{nM}$. The sensor spacing is $d = \frac{2L}{N}$.

mass surface density. Denoting the total analyte collection rate on a BIACORE biosensor by J , the response rate is thus proportional to $\frac{J}{L}$. In an array of sensor, the response rate of sensor i is proportional to $\frac{NJ_i}{L}$. The rate of the average response is thus proportional to $\frac{\sum_{i=1}^N J_i}{L}$. Because of higher total collection rate on multiple sensors than a single sensor ($\sum_{i=1}^N J_i > J$), the response rate is higher in a sensor array than a single sensor.

4.3.1 Effect of Flow Rate on Analyte Collection Rate

In this section, the improvement in analyte collection rate, defined in (4.4), is obtained and compared for different flow rates on the BIACORE biosensor. The results quantify the effect of flow rate on analyte collection rate.

The improvement in analyte collection rate is obtained by replacing a single BIACORE biosensor with a uniform array of two biosensors while the total sensing surface area remains

Table 4.4: The maximum improvement in analyte collection rate for different flow rates: The improvement, as defined in (4.4), is obtained by replacing a single BIACORE biosensor with a uniform array of two BIACORE biosensors. The total sensing surface area is fixed. The total length of the biosensors in the array is $L = 1\text{mm}$, which is equal to the length of the single biosensor. Other parameter values are given in Table 4.3. The sensor spacing is considered to be sufficiently large in each case to allow the analyte to replenish between the individual sensors.

Flow rate $Q(\mu\text{L}/\text{min})$	Damkohler number D_a	The ratio k (4.5)	Collection rate improvement $(J^{-1}(J_1 + J_2) - 1)$ (%) compared to one sensor	
			Numerical	Analysis (4.4)
60	3.04	0.02	15.50	17.85
200	2.03	0.009	14.98	15.85
1000	1.19	0.003	11.38	12.57

fixed. The parameter values are given in Table 4.3. Table 4.4 compares the numerical results with the analytical results obtained by (4.4). The results in this table show that increasing the flow rate results in lower improvement in analyte collection rate. This is due to the reduction of the Damkohler number, which indicates that the binding kinetics move towards the reaction-limited regime. The value of k in (4.5) is decreasing with the flow rate. Although, lower values of k yield higher improvements in (4.4) for fixed values of D_a and N (as shown in Fig.4.2), the effect of Damkohler number is dominating. Fig.4.5 compares the responses of the single BIACORE biosensor and the two-BIACORE biosensor array of Table 4.4 for different flow rates. For the given parameters, the response changes non-linearly with the collection rate.

4.4 Summary

This chapter demonstrates that with a fixed sensing surface area, using an array of multiple small sensors instead of a single sensor can substantially improve analyte collection rate,

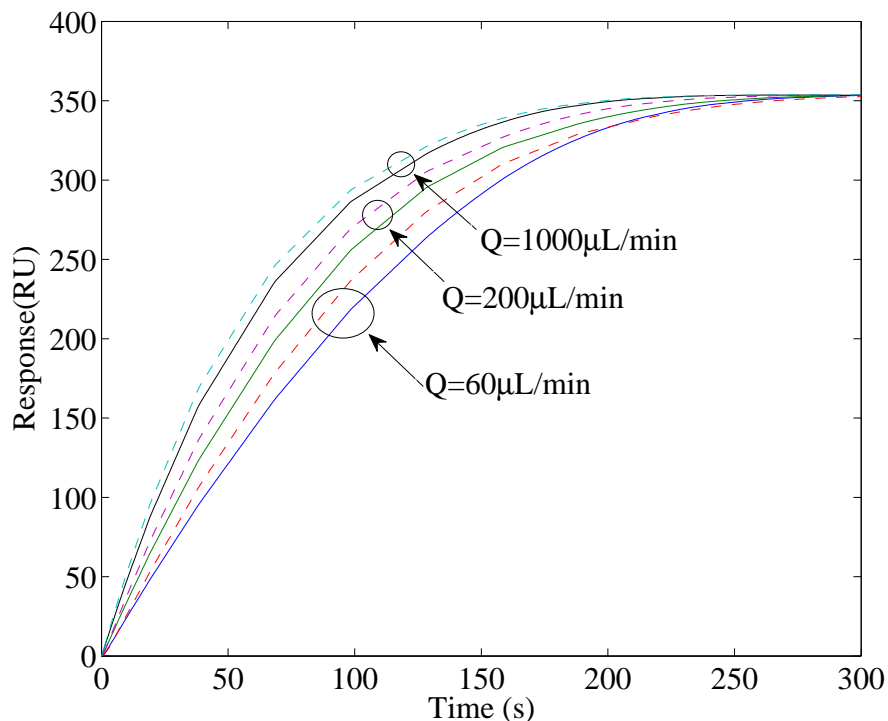


Figure 4.5: Comparison between the responses of a single BIACORE biosensor and a uniform array of two biosensors for different flow rates Q . The solid lines correspond to the single biosensor response and the dashed lines illustrate the responses of the two-biosensor arrays. The total sensing surface area is fixed. Relevant parameter values are given in Table 4.3. The analyte injection concentration is $A^* = 25\text{nM}$. The maximum sensor spacing is $d = \frac{2L}{N}$ for $Q = 60\mu\text{L}/\text{min}$.

which results in higher response rate and detection sensitivity. Table 4.1 demonstrates this for two real-life biosensors. It is shown that for sufficiently spaced-out sensors in the array, maximum analyte collection rate can be obtained by setting the size of all sensors equal. The derived expression (4.4) for the maximum improvement in analyte collection rate depends on the number of sensors N , the Damkohler number D_a defined in (1.4), and the ratio k defined in (4.5). Here is a summary on how these parameters affect the improvement in analyte collection rate:

1. According to (4.4), when the kinetics condition approaches to mass-transport limited

(higher Damkohler number D_a), multiple sensors improve the collection rate more significantly. This is also verified by intuition due to the fact that distributing the sensing surface along the flow direction can only affect the mass-transport limit on the analyte collection rate. In the mass-transport limited regime, the maximum improvement (4.4) increases to $g(k, N)$ in (4.7).

2. In the reaction-limited regime ($D_a \ll 1$), multiple sensors cannot improve analyte collection rate. The expression (4.4) is not valid in this regime. The analyte concentration, everywhere in the flow chamber, achieves the injection concentration A^* . In this case, the collection rate J_i on sensor i is obtained by (4.3) and (1.4) as $J_i = A^*k_{on}\theta wL_i$, which is equal to the reactive flux on the sensor. Thus, the total collection rate is equal to the reaction-limited collection rate of a single sensor.
3. Increasing the value of k reduces the improvement (4.4) in analyte collection rate. This effect can be justified by the physical interpretation of k . The value of k is the ratio of the collection rate of the single sensor to the input convective flux that is the maximum attainable analyte collection rate. When k increases to 1, we can expect that multiple sensors yield less improvement in analyte collection rate until k hits the full collection region.
4. The results in Section 4.4 show that increasing the flow rate reduces the attainable improvement in analyte collection rate that is obtained by multiple-sensor measurements. The reason is that the binding kinetics change towards the reaction-limited regime.

In Section 4.3, it was shown that splitting the sensing area yields higher improvements in the response of BIACORE biosensor compared to the ICS biosensor in Section 4.2. The reasons are the higher value of Damkohler number and smaller value of k for the BIACORE

biosensor.

Chapter 5

On the Accuracy of the Two-Compartment Model

The analyses of our previous chapters relies on the accuracy of the two-compartment model (2.12)-(2.14). In this chapter, we construct a mathematical proof for the two-compartment model and derive an upper bound for its approximation error.

The two-compartment model (2.12)-(2.14) is based on the asymptotic solution of advection-diffusion in a fluid flow in the classical Graetz problem. The Graetz problem involves mass transfer to the walls of a round tube from a fluid in a laminar flow with parabolic profile. The wall of the tube downstream of a certain point is maintained at a constant concentration. The two-compartment model derivation is based on the approximation of the mass flux to the wall of the tube. Although, this flux is obtained under the constant boundary condition, the results have been used in the form of the two-compartment model, where the boundary concentration is time and space varying. To our best knowledge, there is not a rigorous mathematical proof for the accuracy of the two-compartment model in the current literature. Therefore, we construct a mathematical proof for the two-compartment model in this chapter. We derive an upper bound for the modeling error in the approximation of the immobilized species concentration on the reactive surface.

Graetz [40, 71, 93] treated the mass transfer problem in a round tube by the method of separation of variables by neglecting the axial diffusion under the condition that the Péclet number is large. In 1928, André Lévêque observed that convective heat transfer in a flowing

fluid is affected only by the velocity values very close to the surface [70]. For flows of large Prandtl/Péclet number, the heat/mass transition from surface to the free stream takes place across a very thin region close to the surface. Lévêque solved the Graetz problem near the wall downstream the tube close to the near end of the mass-transfer section. In this region (diffusion layer), the velocity distribution can be linearly approximated. Also the effect of cylindrical geometry disappears and Lévêque found that the solution of the approximate differential equation depends only on a combined variable, which is the ratio of the distance from the wall surface to the cube root of the axial distance from the beginning of the mass-transfer section. Then, the rate of mass transfer (the mass flux) towards the tube wall was obtained. The Lévêque solution is also applicable to the problem of mass transfer to a flat plate. The two-compartment model relates to the Lévêque solution.

After a brief review of the Lévêque solution, we will describe how the two-compartment model can be derived by making a simplifying assumption in Section 5.1. We do not resort to this simplistic derivation of the two-compartment model and construct a detailed mathematical proof in Section 5.2, where the order of accuracy of this model compared to the PDE model is derived.

5.1 The Two-Compartment Model Based on the Lévêque Solution

In this section, derivation of the two-compartment model based on the Lévêque solution is described.

Lévêque derived the solution of the concentration in the boundary layer of a laminar flow with parabolic profile in a round tube. In a similar mass-transfer problem on a flat plate, the boundary layer concentration is obtained by the same formula. Here, we directly derive

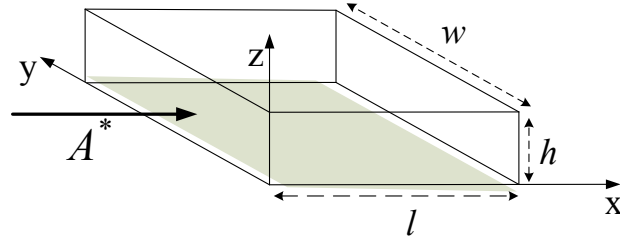


Figure 5.1: The fluid containing analytes enters from the left side of the flow chamber. The analyte concentration at the inlet is A^* as expressed in the boundary conditions in 5.6.

the L ev eque solution, which is an asymptotic solution, for the advection diffusion equation (2.2) in a tube with rectangular cross section and then derive the two-compartment model.

Consider the flow chamber (2.1) with only a single sensor as shown in Fig.5.1. The sensor is fitted to the flow chamber with the same length and width. Consider the advection-diffusion PDE model (2.2)-(2.7) for this system:

$$A_t = \gamma(A_{zz} + A_{xx}) - v(z)A_x \quad (5.1)$$

$$A(x, z, 0) = A_0(x, z)$$

$$A(0, z, t) = A^*$$

$$A_x(l, z, t) = 0$$

$$A_z(x, h, t) = 0$$

$$\gamma A_z(x, 0, t) = \mathfrak{R}(\mathbf{u}(x, t), A(x, 0, t)),$$

coupled with

$$\mathbf{u}_t(x, t) = \mathfrak{F}(\mathbf{u}(x, t), A(x, 0, t)) \quad (5.2)$$

$$\mathbf{u}(x, 0) = \mathbf{u}_0,$$

In (5.1)-(5.2), t denotes time, γ is the target molecule diffusion constant and $v(z)$ describes

the fully developed velocity profile in the flow chamber defined by (1.5). The concentration at the inlet of the flow chamber is constant equal to A^* . The rate of grabbing analytes on the sensor is denoted by $\mathfrak{R}(\mathbf{u}(x, t), A(x, 0, t))$, where $\mathbf{u}(x, t)$ is the surface vector concentration of immobilized chemical species at point x and time t on the biosensor. Here, each chemical reaction that occurs on the sensor has the form



where each one of B and C is either the analyte or one of the immobilized components and D can only be one of the immobilized components. By merging the concentration vector of immobilized species \mathbf{u} to the concentration $a(x, t) = A(x, 0, t)$ into one big vector \mathbf{V} , the reaction law for the i -th component of \mathbf{V} , denoted by $\mathbf{V}(i)$, has the form

$$\frac{d\mathbf{V}(i)}{dt} = \sum_{m=1}^M \sum_{\substack{n=1 \\ n>m}}^N k_{m,n} \mathbf{V}(m)^s \mathbf{V}(n)^p, \quad (5.4)$$

where $p, s \in 0, 1$ and $k_{m,n} \in \mathbb{R}$ corresponds to the reaction rate constants. In (5.4), $k_{m,i}, k_{i,n} < 0$. This is due to the fact that aggregation of each reactant on one side of a reaction increases the reaction rate towards the reverse direction causing the reduction of that reactant. The analyte on the surface, which binds to the immobilized components on the sensor, is always on the left-hand side of the reaction of the form (5.3). Thus, considering (5.4) for the rate of change of the analyte concentration $A(x, 0, t)$ in the reactions, $A(x, 0, t)$ only appears in bilinear terms with negative coefficient. For example, $\mathfrak{R}(\mathbf{u}(x, t), A(x, 0, t))$, which is the negative of the rate of change of analyte in the reactions, can have the form

$$\mathfrak{R}(\mathbf{u}, A) = A(f_1 \mathbf{u}(1) + f_2 \mathbf{u}(2) + f_3 \mathbf{u}(3)) - r_1 \mathbf{u}(4) - r_2 \mathbf{u}(5) - r_3 \mathbf{u}(6), \quad (5.5)$$

Without loss of generality about our assumptions, we take this form for \mathfrak{R} for simplicity in our proof in the next section.

Here, we use a general form of initial condition $A(x, z, 0) = A_0(x, z)$. We first non-dimensionalize the model. Denote $q = \frac{h}{l}$, $\epsilon = \frac{\gamma w}{6Q} = \frac{1}{6P_{eH}}$, $\tau = \frac{\gamma t}{h^2}$, $X = \frac{x}{l}$, $Z = \frac{z}{h}$, $u(X, Z, \tau) = \frac{A(x, z, t)}{A^*}$, $\beta(X, \tau) = \frac{\mathbf{u}(x, t)}{\mathbf{u}_0(1)}$, and $\beta_0 = \frac{\mathbf{u}_0}{\mathbf{u}_0(1)}$, where $\mathbf{u}_0(1)$ is the first element of the vector \mathbf{u}_0 . Then

$$\begin{aligned}
 u_\tau &= u_{ZZ} + q^2 u_{XX} + \frac{qZ(Z-1)}{\epsilon} u_X & (5.6) \\
 u(X, Z, 0) &= \frac{A_0(x, z)}{A^*} \\
 u(0, Z, \tau) &= 1 \\
 u_X(1, Z, \tau) &= 0 \\
 u_Z(X, 1, \tau) &= 0 \\
 u_Z(X, 0, \tau) &= R(\beta, a),
 \end{aligned}$$

coupled with

$$\begin{aligned}
 \beta_\tau(X, \tau) &= F(\beta, a) & (5.7) \\
 \beta(X, 0) &= \beta_0,
 \end{aligned}$$

where $a(X, \tau) = u(X, 0, \tau)$, $R(\beta, a) = \frac{h}{\gamma A^*} \mathfrak{R}(\mathbf{u}_0(1)\beta, A^*a)$ and $F(\beta, a) = \frac{h^2}{\gamma \mathbf{u}_0(1)} \mathfrak{F}(\mathbf{u}_0(1)\beta, A^*a)$. For a high Péclet number, ϵ is small and asymptotic expansions can be used to obtain approximate solutions. Using asymptotic expansion technique [74], the inner solution (in the region near the surface of the sensor but not close to the end points) can be written as the

following asymptotic series:

$$u(X, Z, \tau) = u_0\left(X, \frac{Z}{\epsilon^\alpha}, \tau\right) + \sum_{n=1}^{\infty} u_n\left(X, \frac{Z}{\epsilon^\alpha}, \tau\right) \epsilon^{n\eta}, \quad Z \ll 1, \quad (5.8)$$

where $\eta, \alpha > 0$. Here, the thickness of the boundary layer is of order ϵ^α . The values of α and η are obtained by finding the dominant balances. By substituting (5.8) in the PDE (5.6) and balancing the leading order terms, we obtain $\alpha = 1/3$ and

$$u_{0\zeta\zeta} = q\zeta u_{0X}, \quad (5.9)$$

where $\zeta = \frac{Z}{\epsilon^{1/3}}$, $u_{0\zeta\zeta}$ is the second order derivative of u_0 with respect to ζ and u_{0X} is the first order derivative of u_0 with respect to X . The solution to (5.9) is obtained by a similarity transformation, which yields

$$u_0(X, \zeta, \tau) = \int_0^{\zeta X^{-1/3}} K_1(\tau) \exp\left(-\frac{q}{9}\nu^3\right) d\nu + K_2(\tau). \quad (5.10)$$

Assuming that on the boundary $u_0(X, 0, \tau) = \tilde{u}(\tau)$, then we obtain $K_2(\tau) = \tilde{u}(\tau)$. By matched asymptotic method, another boundary condition is given as $u_0(X, \zeta, \tau) \rightarrow 1$ as $\zeta \rightarrow \infty$ [40]. Therefore, the dominant term of the inner solution is obtained as

$$u_0(X, Z\epsilon^{-1/3}, \tau) = \left(\frac{q}{9}\right)^{1/3} \frac{1 - \tilde{u}(\tau)}{\Gamma(4/3)} \int_0^{Z(\epsilon X)^{-1/3}} \exp\left(-\frac{q}{9}\nu^3\right) d\nu + \tilde{u}(\tau). \quad (5.11)$$

From (5.8) and (5.11), the derivative $\frac{\partial}{\partial Z}u(X, 0, \tau)$ on the sensor surface can be approximated as

$$\frac{\partial}{\partial Z}u(X, 0, \tau) \approx \left(\frac{q}{9\epsilon X}\right)^{1/3} \frac{1 - \tilde{u}(\tau)}{\Gamma(4/3)}. \quad (5.12)$$

Converting (5.12) back to dimensional form and setting $l = L$, we obtain the surface average diffusive flux on the sensor surface as

$$\frac{\gamma}{L} \int_0^L \frac{\partial}{\partial z} A(x, 0, t) dx \approx \gamma \frac{(9/4)^{1/3}}{\Gamma(4/3)} \left(\frac{Q}{\gamma w h^2 L} \right)^{1/3} (A^* - \bar{a}(t)). \quad (5.13)$$

Therefore, the surface average diffusive flux on the sensor surface is obtained as $\frac{\gamma}{\delta} (A^* - \bar{a}(t))$, where δ is obtained by (2.13). Then, the time variations of the analyte surface concentration $a(t)$ is obtained by deducting the analyte grabbing rate on the surface:

$$\delta \frac{da(t)}{dt} = \frac{\gamma}{\delta} (A^* - a(t)) - \mathfrak{R}(\bar{\mathbf{u}}(t), a(t)), \quad a(0) = 0, \quad (5.14)$$

Here, δ is interpreted as the thickness of the diffusion layer and $\bar{\mathbf{u}}(t)$ is the surface average of $\mathbf{u}(t)$. In (5.14), the derivative $\frac{da(t)}{dt}$ is multiplied by the thickness δ because the total mass transport per unit length across the diffusion layer changes the total mass along δ . The time variations of $\bar{\mathbf{u}}$ is governed by the following ODE system:

$$\bar{\mathbf{u}}_t = \mathfrak{F}(\bar{\mathbf{u}}, a), \quad \bar{\mathbf{u}}(0) = \mathbf{u}_0 \quad (5.15)$$

The assumption that the concentration $u_0(X, 0, \tau) = \tilde{u}(\tau)$ on the boundary is space-invariant is the simplifying assumption in this derivation. In the next section, we construct a more rigorous proof for the accuracy of the two-compartment model, where we obtain the order of its approximation error.

5.2 Proof of the Accuracy of the Two-Compartment Model

The above derivation of the two-compartment model is based on the assumption that the analyte concentration on the sensor surface is only a function of time, which is not a well-supported assumption. Also, the order of approximation is not determined in the above derivation. In this section, we construct a rigorous mathematical proof to derive an upper bound on the approximation error of the two-compartment model.

We use the following assumptions:

1. The derivatives u_τ , u_X , and u_{XX} of (5.6)-(5.7) are bounded.
2. There is $h_0 = O(\epsilon^{1/3})$ such that the derivative u_{ZZ} is bounded for $h_0 = O(\epsilon^{1/3}) \leq Z \leq 1 - h_0$.
3. For $Z = O(h_0)$, $u_Z(X, Z, \tau) = O(h_0^{-1}) = O(\epsilon^{-1/3})$, $u_{ZZ}(X, Z, \tau) = O(h_0)$, $u_{Z^3}(X, Z, \tau) = \partial^3 u / \partial Z^3 = O(1)$, and the highest order of magnitude for $u_{Z^n} = \partial^n u / \partial Z^n$, $n \geq 4$ is $O(h_0^{-1})$.
4. The solution u and β of (5.6)-(5.7) is non-negative.

The above assumptions are justifiable through asymptotic analysis and numerical analysis. Based on asymptotic analysis and numerical experiments, the time derivative and the derivatives in X direction along the flow direction are bounded. Therefore, assumption (1) is a reasonable assumption. The region $h_0 \leq Z \leq 1 - h_0$ in assumption (2) consists of two regions; the region $h_0 \ll Z \ll 1 - h_0$ far from the surface, where boundary layers along Z direction forms and $Z = O(h_0)$ or $1 - Z = O(h_0)$ are in the boundary layers. In the region outside the boundary layers, the derivatives with respect to Z are bounded. In the regions inside the boundary layers, i.e. $Z = O(h_0)$ or $1 - Z = O(h_0)$, the derivatives can be

unbounded. However, taking the second derivative of (5.11) with respect to Z , shows that $u_{ZZ}(X, Z, \tau)$ for $Z = O(h_0)$ is bounded. Similarly, we can show this for $1 - Z = O(h_0)$. Assumption (3) can be justified by taking the derivatives of (5.11) with respect to Z . It is assumed in assumption (4) that the solution of (5.6)-(5.7) is non-negative. This is based on the principle that the PDE accurately describes the variations of concentration, which is a non-negative physical quantity.

Theorem 1 *Assume system (5.6)-(5.7) has a solution (u, β) such that $u \in C^{1,2,3}((0, T) \times (0, 1) \times (0, 1))$. Assume that $\epsilon \ll 1$, $h_0 = O(\epsilon^{1/3})$ and $Z < h_0$. Then, based on the assumptions (1) to (4), β could be approximated by the solution of the following ODE system*

$$\begin{aligned} \tilde{u}_\tau(X, Z, \tau) &= \frac{2}{h_0(h_0 - Z)} (1 - \tilde{u}(X, Z, \tau)) - \frac{2}{h_0} R(\tilde{\beta}(X, \tau), \tilde{u}(X, Z, \tau)), & (5.16) \\ \tilde{u}(X, Z, 0) &= A_0(X, Z)/A^* \\ \tilde{\beta}_\tau(X, Z, \tau) &= F(\tilde{\beta}(X, Z, \tau), \tilde{u}(X, Z, \tau)) \\ \tilde{\beta}(X, Z, 0) &= \beta_0, \end{aligned}$$

where

$$\int_0^1 |\tilde{\beta} - \beta|^2 dX \leq O(\epsilon^{1/3}).$$

Remark 2 *Using the definition of the dimensionless variables and parameters in (5.6)-(5.7), the non-dimensional form of the two-compartment model (5.14)-(5.15) is obtained as*

$$\tilde{u}_\tau = \frac{1}{\Delta^2} (1 - \tilde{u}) - \frac{1}{\Delta} R(\tilde{\beta}, \tilde{u}), \quad (5.17)$$

$$\begin{aligned}\tilde{u} &= 0 \\ \tilde{\beta}_\tau &= F(\tilde{\beta}, \tilde{u}) \\ \tilde{\beta} &= \beta_0,\end{aligned}$$

where Δ is obtained as $\Delta = 1.23(\frac{\epsilon}{q})^{1/3}$ using (2.13). This model is also obtained by choosing $h_0 = 2\Delta$, $Z = h_0/2$, and $A_0(X, Z) = 0$ in (5.16). In this case, $h_0 = O(\epsilon^{1/3})$ and $Z < h_0$, which satisfy the conditions in Theorem 1.

Proof For $h_0 \leq Z \leq 1 - h_0$, system (5.6) could be approximated by

$$\begin{aligned}\tilde{u}_X(X, Z, \tau) &= 0, \\ \tilde{u}(0, Z, \tau) &= 1,\end{aligned}\tag{5.18}$$

which means that $\tilde{u}(X, Z, \tau) = 1$. In fact, put $\bar{u}(X, Z, \tau) = \tilde{u}(X, Z, \tau) - u(X, Z, \tau)$. Then

$$\bar{u}_X(X, Z, \tau) = \frac{\epsilon}{qZ(1-Z)} [u_\tau(X, Z, \tau) - u_{ZZ}(X, Z, \tau) - q^2 u_{XX}(X, Z, \tau)] = O(\eta_1) + O(\eta_2)\tag{5.19}$$

$$\bar{u}(0, Z, \tau) = 0,$$

which implies that $\bar{u} = O(\eta_1) + O(\eta_2)$, with $\eta_1 = \frac{\epsilon}{qh_0}$ and $\eta_2 = \frac{q\epsilon}{h_0}$. Here, we use the assumption that u_τ , u_{XX} , and u_{ZZ} are bounded according to assumptions (1) and (2).

Consider the following PDE system:

$$\hat{u}_\tau = q^2 \hat{u}_{XX} + \frac{q}{\epsilon} Z(Z-1) \hat{u}_X + \hat{u}_{ZZ} + G(X, Z, \tau), \quad 0 < Z < h_0\tag{5.20}$$

$$\hat{u}(X, Z, 0) = A(X, Z, 0)/A^*$$

$$\hat{u}(0, Z, \tau) = 1$$

$$\hat{u}_X(1, Z, \tau) = 0$$

$$\hat{u}(X, h_0, \tau) = 1$$

$$\hat{u}_Z(X, 0, \tau) = R(\hat{\beta}, \hat{u}(X, 0, \tau)) \quad (5.21)$$

$$\hat{\beta}_\tau(X, Z, \tau) = F(\hat{\beta}(X, Z, \tau), \hat{u}(X, Z, \tau)) = F(\hat{\beta}(X, Z, \tau), \hat{u}(X, 0, \tau)) + O(Z) \quad (5.22)$$

$$\beta(X, Z, 0) = \beta_0,$$

where

$$G(X, Z, \tau) = O\left(\frac{Z}{h_0} + h_0\right). \quad (5.23)$$

Define the error between the system (5.6)-(5.7) and (5.20) by $\check{u} = u - \hat{u}$. The error \check{u} satisfies the following PDE system:

$$\check{u}_\tau = q^2 \check{u}_{XX} + \frac{q}{\epsilon} Z(Z-1) \check{u}_X + \check{u}_{ZZ} + G(X, Z, \tau) \quad 0 < Z < h_0 \quad (5.24)$$

$$\check{u}(X, Z, 0) = 0$$

$$\check{u}(0, Z, \tau) = 0$$

$$\check{u}_X(1, Z, \tau) = 0 \quad (5.25)$$

$$\check{u}(X, h_0, \tau) = u(X, h_0, \tau) - 1 \quad (5.26)$$

$$\check{u}_Z(X, 0, \tau) = R(\beta, a) - R(\hat{\beta}, \hat{a}) \quad (5.27)$$

$$\check{\beta}(X, Z, \tau)_\tau = F(\beta, a) - F(\hat{\beta}, \hat{a}) + O(Z)$$

$$\check{\beta}(X, Z, 0) = 0.$$

Here, $\hat{a} = \hat{u}(X, 0, \tau)$.

We obtain

$$\begin{aligned}
 \frac{1}{2} \frac{d}{d\tau} \int_0^{h_0} \int_0^1 \check{u}^2 dX dZ &= \int_0^{h_0} \int_0^1 \check{u} \check{u}_\tau dX dZ \\
 &= \int_0^{h_0} \int_0^1 \check{u} \left[q^2 \check{u}_{XX} + \frac{q}{\epsilon} Z(Z-1) \check{u}_X + \check{u}_{ZZ} \right] dX dZ \\
 &+ \int_0^{h_0} \int_0^1 \check{u} G(X, Z, \tau) dX dZ.
 \end{aligned} \tag{5.28}$$

For the first term in the above integral, we use integration by parts as follows:

$$\begin{aligned}
 \int_0^{h_0} \int_0^1 q^2 \check{u} \check{u}_{XX} dX dZ &= \int_0^{h_0} q^2 \check{u} \check{u}_X \Big|_{X=0}^1 - \int_0^{h_0} \int_0^1 q^2 |\check{u}_X|^2 dX dZ \\
 &= -q^2 \int_0^{h_0} \int_0^1 |\check{u}_X|^2 dX dZ
 \end{aligned} \tag{5.29}$$

Here, we used the boundary conditions (5.25) and (5.26). The second term in the integral (5.28) can be written as

$$\begin{aligned}
 \int_0^{h_1} \int_0^1 \frac{q}{\epsilon} Z(Z-1) \check{u} \check{u}_X dX dZ &= \int_0^{h_1} \frac{q}{2\epsilon} Z(Z-1) [\check{u}^2]_{X=0}^1 dZ \\
 &= \int_0^{h_1} \frac{q}{2\epsilon} Z(Z-1) \check{u}^2(1, Z, \tau) dZ.
 \end{aligned} \tag{5.30}$$

We then approximate $\check{u}^2(1, Z, \tau)$ using the first order Taylor expansions as

$$\check{u}^2(1, Z, \tau) = \check{u}^2(1, h_0, \tau) + 2\check{u}(1, h_0, \tau)\check{u}_Z(1, h_0, \tau)(Z - h_0) + O((Z - h_0)^2)$$

Equation (5.30) can thus be expressed as

$$\begin{aligned}
 \int_0^{h_0} \int_0^1 \frac{q}{\epsilon} Z(Z-1) \check{u} \check{u}_X dX dZ &= \int_0^{h_0} \frac{q}{2\epsilon} Z(Z-1) \check{u}^2(1, h_0, \tau) dZ \\
 &+ \int_0^{h_0} \frac{q}{\epsilon} Z(Z-1) [\check{u}(1, h_0, \tau)\check{u}_Z(1, h_0, \tau)(Z - h_0) + O((Z - h_0)^2)] dZ
 \end{aligned}$$

$$\begin{aligned}
 &= \frac{q}{2\epsilon} \left(\frac{h_0^3}{3} - \frac{h_0^2}{2} \right) \check{u}^2(1, h_0, \tau) + \check{u}(1, h_0, \tau) \check{u}_Z(1, h_0, \tau) \int_0^{h_0} \frac{q}{\epsilon} Z(Z-1)(Z-h_0) dZ \\
 &+ O\left(\frac{h_0^4 q}{\epsilon}\right)
 \end{aligned}$$

According to assumption (3), the term $Zu_Z(1, h_0, \tau)$ is bounded. Since, the PDE (5.20) has the same structure as (5.6)-(5.7), the term $Z\hat{u}_Z(1, h_0, \tau)$ is also bounded. Therefore $\check{u}_Z(1, h_0, \tau)$ is also bounded. Using the boundary condition (5.27) and boundedness of $Z\check{u}_Z(1, h_0, \tau)$, (5.30) can be written as

$$\int_0^{h_0} \int_0^1 \frac{q}{\epsilon} Z(Z-1) \check{u} \check{u}_X dX dZ = O\left(\frac{qh_0^2}{\epsilon}(\eta_1 + \eta_2)\right) = O(h_0) \quad (5.31)$$

For the third term in the integral (5.28), we have

$$\begin{aligned}
 &\int_0^{h_0} \int_0^1 \check{u} \check{u}_{ZZ} dX dZ = \int_0^1 [\check{u} \check{u}_Z]_{Z=0}^{h_0} dX - \int_0^1 \int_0^{h_0} |\check{u}_Z|^2 dZ dX \\
 &= \int_0^1 \check{u}(X, h_0, \tau) \check{u}_Z(X, h_0, \tau) dX - \int_0^1 \check{a} \left[R(\beta, a) - R(\hat{\beta}, \hat{a}) \right] dX \\
 &\quad - \int_0^1 \int_0^{h_0} |\check{u}_Z|^2 dZ dX,
 \end{aligned} \quad (5.32)$$

where $\check{a} = a - \hat{a} = u(X, 0, \tau) - \hat{u}(X, 0, \tau)$. Using (5.5) for the second integral in (5.32), it can be expressed that

$$\begin{aligned}
 &- \check{a} \left[R(\beta, a) - R(\hat{\beta}, \hat{a}) \right] \\
 &= \frac{h\mathbf{u}_0(1)}{\gamma} (-f_1 \check{a}(a\mathbf{u}(1) - \hat{a}\hat{\mathbf{u}}(1)) - f_2 \check{a}(a\mathbf{u}(2) - \hat{a}\hat{\mathbf{u}}(2)) - f_3 \check{a}(a\mathbf{u}(3) - \hat{a}\hat{\mathbf{u}}(3))) \\
 &+ \frac{h\mathbf{u}_0(1)}{\gamma A^*} (r_1 \check{a} \check{\mathbf{u}}(4) + r_2 \check{a} \check{\mathbf{u}}(5) + r_3 \check{a} \check{\mathbf{u}}(6)) \\
 &= \frac{h\mathbf{u}_0(1)}{\gamma} (-f_1 \check{a}^2 \mathbf{u}(1) - f_1 \hat{a} \check{a} \check{\mathbf{u}}(1) - f_2 \check{a}^2 \mathbf{u}(2) - f_2 \hat{a} \check{a} \check{\mathbf{u}}(2)) \\
 &+ \frac{h\mathbf{u}_0(1)}{\gamma A^*} (r_1 \check{a} \check{\mathbf{u}}(4) + r_2 \check{a} \check{\mathbf{u}}(5) + r_3 \check{a} \check{\mathbf{u}}(6)) \leq K\lambda |\check{a}|^2 + \frac{K}{\lambda} |\check{\beta}|^2,
 \end{aligned} \quad (5.33)$$

where $\lambda > 0$ in the Cauchy inequality is chosen arbitrarily and $0 < K < \infty$ is a constant. Throughout the proof $K = K + 1$. Here, we use assumption (4), where the solution β to the original system (5.6)-(5.7) is assumed to be nonnegative. Using assumption (3), we obtain

$$\int_0^1 \check{u}(X, h_0, \tau) \check{u}_Z(X, h_0, \tau) dX = O(h_0^{-1}(\eta_1 + \eta_2)) = O(h_0)$$

Using (5.32), (5.33), and the above equation, we have

$$\begin{aligned} \int_0^1 \int_0^{h_0} \check{u} \check{u}_{ZZ} dZ dX &\leq K\lambda \int_0^1 |\check{a}|^2 dX + \frac{K}{\lambda} \int_0^1 |\check{\beta}|^2 dX - \int_0^1 \int_0^{h_1} |\check{u}_Z|^2 dZ dX \\ &+ O(h_0) \end{aligned} \quad (5.34)$$

Based on the Cauchy inequality and (5.23), we can write the last term of (5.28) as

$$\begin{aligned} \int_0^{h_0} \int_0^1 \check{u} G(X, Z, \tau) dX dZ &\leq \int_0^{h_0} \int_0^1 \check{u}^2 dX dZ + \int_0^{h_0} \int_0^1 G^2(X, Z, \tau) dX dZ \\ &\leq \int_0^{h_0} \int_0^1 \check{u}^2 dX dZ + O(h_0) \end{aligned} \quad (5.35)$$

According to (5.29), (5.31), (5.34), and (5.35), we have

$$\begin{aligned} \frac{1}{2} \frac{d}{d\tau} \int_0^{h_0} \int_0^1 |\check{u}|^2 dX dZ &\leq -q^2 \int_0^{h_0} \int_0^1 |\check{u}_X|^2 dX dZ + K\lambda \int_0^1 |\check{a}|^2 dX \\ &+ \frac{K}{\lambda} \int_0^1 |\check{\beta}|^2 dX - \int_0^1 \int_0^{h_0} |\check{u}_Z|^2 dZ dX \\ &+ \int_0^{h_1} \int_0^1 \check{u}^2 dX dZ + O(h_0) \end{aligned}$$

Based on the Trace theorem [94], there exists a $C > 0$ such that

$$\int_0^1 |\check{a}|^2 dX \leq C \left[\int_0^1 \int_0^{h_0} |\check{u}|^2 dZ dX + \int_0^1 \int_0^{h_0} |\check{u}_X|^2 dZ dX + \int_0^1 \int_0^{h_0} |\check{u}_Z|^2 dZ dX \right]$$

Therefore,

$$\begin{aligned} \frac{1}{2} \frac{d}{d\tau} \int_0^{h_0} \int_0^1 |\check{u}|^2 dX dZ &\leq -q^2 \int_0^{h_0} \int_0^1 |\check{u}_X|^2 dX dZ + K\lambda \int_0^1 \int_0^{h_1} |\check{u}|^2 dZ dX \quad (5.36) \\ &+ K\lambda \int_0^1 \int_0^{h_0} |\check{u}_X|^2 dZ dX + K\lambda \int_0^1 \int_0^{h_1} |\check{u}_Z|^2 dZ dX \\ &+ \frac{K}{\lambda} \int_0^1 |\check{\beta}|^2 dX - \int_0^1 \int_0^{h_1} |\check{u}_Z|^2 dZ dX \\ &+ \int_0^{h_1} \int_0^1 \check{u}^2 dX dZ + O(h_0) \end{aligned}$$

For $\check{\beta}$ we have

$$\frac{1}{2} \frac{d}{d\tau} \int_0^1 |\check{\beta}|^2 dX = \int_0^1 \check{\beta}^T \check{\beta}_\tau dX = \int_0^1 \check{\beta} \left(F(\beta, a) - F(\check{\beta}, \check{a}) + O(Z) \right)$$

Based on our discussion on (5.4), our derivation in (5.33) and the positivity of a and β as the solutions of the original PDE (5.6)-(5.7), we can similarly obtain

$$\check{\beta}^T \left(F(\beta, a) - F(\check{\beta}, \check{a}) \right) \leq K\hat{\lambda} \int_0^1 |\check{a}|^2 dX + \frac{K}{\hat{\lambda}} \int_0^1 |\check{\beta}|^2 dX. \quad (5.37)$$

Using the Cauchy inequality, we also have

$$\int_0^1 \check{\beta} O(Z) dX \leq K\hat{\lambda} O(Z^2) + \frac{K}{\hat{\lambda}} \int_0^1 |\check{\beta}|^2 dX$$

Hence, based on the Trace theorem, we have

$$\begin{aligned} \frac{1}{2} \frac{d}{d\tau} \int_0^1 |\check{\beta}|^2 dX &\leq K\hat{\lambda} \int_0^1 \int_0^{h_0} |\check{u}|^2 dZ dX + K\hat{\lambda} \int_0^1 \int_0^{h_0} |\check{u}_X|^2 dZ dX \\ &+ K\hat{\lambda} \int_0^1 \int_0^{h_0} |\check{u}_Z|^2 dZ dX + \frac{K}{\hat{\lambda}} \int_0^1 |\check{\beta}|^2 dX + O(h_0^2 \hat{\lambda}) \end{aligned} \quad (5.38)$$

We choose λ and $\hat{\lambda}$ such that $K\lambda + K\hat{\lambda} - 1 \leq 0$ and $K\lambda + K\hat{\lambda} - q^2 \leq 0$. Then, the sum of (5.36) and (5.38) yields

$$\begin{aligned} \frac{1}{2} \frac{d}{d\tau} \int_0^1 \int_0^{h_0} |\check{u}|^2 dZ dX + \frac{1}{2} \frac{d}{d\tau} \int_0^1 |\check{\beta}|^2 dX &\leq (K\lambda + K\hat{\lambda} + 1) \int_0^1 \int_0^{h_0} |\check{u}|^2 dZ dX \\ &+ \left(\frac{K}{\lambda} + \frac{K}{\hat{\lambda}} \right) \int_0^1 |\check{\beta}|^2 dX + O(h_0) + O(h_0^2 \hat{\lambda}) \end{aligned} \quad (5.39)$$

Using the Gronwall's inequality, for a bounded compact interval of time, we have

$$\int_0^1 \int_0^{h_1} |\check{u}|^2 dZ dX + \int_0^1 |\check{\beta}|^2 dX \leq O(h_0) + O(h_0^2 \hat{\lambda}) \quad (5.40)$$

Now consider the solution $\hat{u}(X, Z, \tau)$ of (5.20) for $0 < Z < h_0$. Using the Taylor series expansion and assumption (3), it can be expressed that

$$\hat{u}(X, h_0, \tau) = \hat{u}(X, Z, \tau) + (h_0 - Z)\hat{u}_Z(X, Z, \tau) + \frac{(h_0 - Z)^2}{2}\hat{u}_{ZZ}(X, Z, \tau) + (h_0 - Z)^3 O(1)$$

and

$$\hat{u}(X, 0, \tau) = \hat{u}(X, Z, \tau) - Z\hat{u}_Z(X, Z, \tau) + \frac{Z^2}{2}\hat{u}_{ZZ}(X, Z, \tau) + Z^3 O(1)$$

Therefore, by adding the above two equations, we obtain

$$\frac{\hat{u}(X, h_0, \tau) - \hat{u}(X, Z, \tau)}{h_0 - Z} + \frac{\hat{u}(X, 0, \tau) - \hat{u}(X, Z, \tau)}{Z} = \frac{h_0}{2} \hat{u}_{ZZ}(X, Z, \tau) + [(h_0 - Z)^2 + Z^2] O(1)$$

Using (5.22), assumption (3), and the first order Taylor expansion, we have

$$\begin{aligned} \hat{u}(X, 0, \tau) &= \hat{u}(X, Z, \tau) - ZR(\hat{\beta}(X, \tau), \hat{u}(X, 0, \tau)) + Z^2O(1) \\ &= \hat{u}(X, Z, \tau) - ZR(\hat{\beta}(X, \tau), \hat{u}(X, Z, \tau)) + Z^2O(1). \end{aligned}$$

Therefore, according to (5.21) we have

$$\begin{aligned} \hat{u}_{ZZ}(X, Z, \tau) &= \frac{2}{h_0(h_0 - Z)} \left[1 - \hat{u}(X, Z, \tau) - (h_0 - Z)R(\hat{\beta}(X, \tau), \hat{u}(X, Z, \tau)) \right] \quad (5.41) \\ &\quad + \frac{2[Z + (h_0 - Z)^2 + Z^2] O(1)}{h_0} \\ &= \frac{2}{h_0(h_0 - Z)} \left[1 - \hat{u}(X, Z, \tau) - (h_0 - Z)R(\hat{\beta}(X, \tau), \hat{u}(X, Z, \tau)) \right] \\ &\quad - O\left(\frac{Z}{h_0} + h_0\right) \end{aligned}$$

Thus, the solution of the PDE system (5.20) is equal to the solution of the following PDE system:

$$\begin{aligned} \hat{u}_\tau &= q^2 \hat{u}_{XX} + \frac{q}{\epsilon} Z(Z - 1) \hat{u}_X \quad (5.42) \\ &\quad + \frac{2}{h_0(h_0 - Z)} \left[1 - \hat{u} - (h_0 - Z)R(\hat{\beta}, \hat{u}) \right] \quad 0 < Z < h_0 \end{aligned}$$

$$\hat{u}(X, Z, 0) = A_0(X, Z)/A^*$$

$$\hat{u}(0, Z, \tau) = 1$$

$$\hat{u}_X(1, Z, \tau) = 0$$

coupled with

$$\hat{\beta}_\tau = F(\hat{\beta}, \hat{u}), \quad \hat{\beta}(X, Z, 0) = \beta_0. \quad (5.43)$$

There, (5.40) is valid for the difference \check{u} between the solutions of (5.6)-(5.7) and (5.42)-(5.43).

Define the error between the system (5.6)-(5.7) and (5.42)-(5.43) by $\check{u} = u - \hat{u}$. The solution of (5.42)-(5.43) is equal to the solution of the following PDE system for $Z < h_1 < h_0$: Now consider the system

$$\tilde{u}_\tau = \frac{2}{h_0(h_0 - Z)} \left[1 - \tilde{u}(X, Z, \tau) - (h_0 - Z)R(\tilde{\beta}, \tilde{u}) \right], \quad 0 < Z < h_1 \leq h_0, \quad (5.44)$$

$$\tilde{u}(X, Z, 0) = A(X, Z, 0)/A^*$$

coupled with

$$\tilde{\beta}(X, Z, \tau)_\tau = F(\tilde{\beta}(X, Z, \tau), \tilde{u}(X, Z, \tau)) \quad (5.45)$$

$$\tilde{\beta}(X, Z, 0) = \beta_0$$

Define the errors $\bar{u} = \hat{u} - \tilde{u}$ and $\bar{\beta} = \hat{\beta} - \tilde{\beta}$ between the solutions of (5.42)-(5.43) and (5.44)-(5.45) for $0 < Z < h_1 \leq h_0$. The errors \bar{u} and $\bar{\beta}$ satisfy

$$\begin{aligned} \bar{u}_\tau = & -\bar{u} \frac{2}{h_0(h_0 - Z)} - \frac{2}{h_0} \left[R(\hat{\beta}, \hat{u}) - R(\tilde{\beta}, \tilde{u}) \right] \\ & + q^2 \hat{u}_{XX} + \frac{q}{\epsilon} Z(Z - 1) \hat{u}_X, \quad 0 < Z < h_1 \leq h_0, \quad \bar{u}(X, Z, 0) = 0 \end{aligned}$$

coupled with

$$\begin{aligned}\bar{\beta}_\tau &= F(\hat{\beta}, \hat{u}) - F(\tilde{\beta}, \tilde{u}) \\ \bar{\beta}(X, Z, 0) &= 0\end{aligned}$$

Then, we obtain

$$\begin{aligned}\frac{1}{2} \frac{d}{d\tau} |\bar{u}|^2 &= \bar{u} \bar{u}_\tau = -\bar{u}^2 \frac{2}{h_0(h_0 - Z)} - \frac{2}{h_0} \bar{u} \left[R(\hat{\beta}, \hat{u}) - R(\tilde{\beta}, \tilde{u}) \right] \\ &\quad + \bar{u} W(X, Z, \tau),\end{aligned}$$

where

$$W(X, Z, \tau) = q^2 \hat{u}_{XX}(X, Z, \tau) + \frac{q}{\epsilon} Z(Z - 1) \hat{u}_X(X, Z, \tau),$$

is bounded according to assumption (1). Similar to (5.33), we can show that

$$-\bar{u} \left[R(\hat{\beta}, \hat{u}) - R(\tilde{\beta}, \tilde{u}) \right] \leq K \lambda_1 |\bar{u}|^2 + \frac{K}{\lambda_1} |\bar{\beta}|^2. \quad (5.46)$$

by proving the positivity of the solution $\tilde{\beta}$ of (5.44)-(5.45) [95]. Using the Cauchy inequality, we have

$$\bar{u} W(X, Z, \tau) \leq \frac{1}{\lambda_2} \bar{u}^2 + \lambda_2 W^2(X, Z, \tau)$$

Hence we obtain

$$\frac{1}{2} \frac{d}{d\tau} |\bar{u}|^2 \leq \left(\frac{1}{\lambda_2} - \frac{2}{h_0(h_0 - Z)} \right) \bar{u}^2 + \frac{K \lambda_1}{h_0} \bar{u}^2 \quad (5.47)$$

$$+ \frac{K}{\lambda_1 h_0} |\bar{\beta}|^2 + W^2 \lambda_2$$

Using the same argument we used in (5.37), it can be expressed that

$$\frac{1}{2} \frac{d}{d\tau} |\bar{\beta}|^2 \leq K \lambda_3 |\bar{u}|^2 + \frac{K}{\lambda_3} |\bar{\beta}|^2. \quad (5.48)$$

We use the positivity of solution of (5.44)-(5.45) to obtain (5.48). Adding up the two inequalities (5.47) and (5.48) and based on the Gronwall's inequality, for a compact bounded interval of time we have

$$|\bar{u}|^2 + |\bar{\beta}|^2 \leq O(q^4 \lambda_2) + O\left(\frac{q^2 h_1^2}{\epsilon^2} \lambda_2\right) + O\left(\frac{q^3 h_1}{\epsilon} \lambda_2\right) \quad (5.49)$$

From (5.40) and (5.49), we have

$$\int_0^1 \left(|\check{\beta}|^2 + |\bar{\beta}|^2 \right) dX \leq O(q^4 \lambda_2) + O\left(\frac{q^2 h_1^2}{\epsilon^2} \lambda_2\right) + O\left(\frac{q^3 h_1}{\epsilon} \lambda_2\right) + O(h_0) + O(h_0^2 \hat{\lambda}). \quad (5.50)$$

Thus,

$$\begin{aligned} \int_0^1 |\beta - \tilde{\beta}|^2 dX &\leq O(q^4 \lambda_2) + O\left(\frac{q^2 h_1^2}{\epsilon^2} \lambda_2\right) + O\left(\frac{q^3 h_1}{\epsilon} \lambda_2\right) \\ &\quad + O(h_0) + O(h_0^2 \hat{\lambda}) \end{aligned} \quad (5.51)$$

Here, we pick $h_1 = h_0$ and λ_2 small enough such that the first three terms on the right-hand side of (5.51) is smaller than the other terms. The value of $\hat{\lambda}$ is also small enough to neglect $O(h_0^2 \hat{\lambda})$. Thus, 5.51) can be expressed as

$$\int_0^1 |\beta - \tilde{\beta}|^2 dX \leq O(h_0) = O(\epsilon^{1/3})$$

The variable $Z < h_0$ in (5.44)-(5.45) behaves as a parameter in an ODE system. Since $h_1 = h_0$, the system (5.44)-(5.45) is equivalent to (5.16).

5.3 Summary

In this chapter, we derive the two-compartment model (2.12)-(2.14) using asymptotic analysis that is based on the existing Lévêque solution for the corresponding PDE. This derivation is contingent on the assumption that the analyte concentration on the binding surface is not spatially varying, which is not a well-supported assumption. Therefore, we prove the accuracy of the two-compartment model, by deriving a tight bound on the difference between the two-compartment solution and the PDE solution. The proof is based on the Trace theorem and the Gronwall's inequality.

Chapter 6

Conclusions and Discussion

In this chapter, we first conclude the thesis in Section 6.1 by summarizing our results and highlighting the contributions. We then discuss different aspects of this work that require further research, where we also suggest several topics for future work in Section 6.2.

6.1 Research Contributions

This thesis develops dynamical models for modeling and analysis of biosensor arrays. It proposes methods to improve molecular detection and concentration estimation in dynamical fluid flow systems by using arrays of surface-based sensors. The contributions are mainly divided into three parts. The first part corresponds to developing PDE and ODE models. In the second part, the developed ODE model is used for estimating the concentration of target molecules in a flow chamber with a biosensor array. These results can be summarized as follows:

1. In Chapter 2, we construct the PDE model (2.2)-(2.7) to describe the dynamics of analytes flowing over a linear array of surface-based biosensors. The PDE model is a generic model that describes the dynamics of mass transport over multiple binding surfaces. We then construct the multi-compartment ODE model (2.15)-(2.19) to approximate the PDE model and solve the parameter estimation problem. The multi-compartment model approximates the asymptotic solution of the PDE system. We derive the multi-compartment ODE model by extending the existing

two-compartment model using the divergence theorem. We specify the range of experimental parameters, in terms of dimensionless physical quantities, where the multi-compartment model is valid. The accuracy of the derived model is illustrated for an ICS biosensor array as an actual example. The structure and operation of ICS biosensors are described in Chapter 1. The PDE and ODE models for this type of biosensor are specified and solved numerically. We show how the PDE model and ODE approximations can satisfactorily model this novel biosensor. In the multi-compartment ODE model, the entire infinite dimensional PDE system is converted to only a few dimensional ODE system. The derived ODE system involves even less state space variables than those obtained by applying conventional discretization methods such as finite difference, finite element, or modal analysis. Not only does the multi-compartment model significantly reduce the computational complexity of the concentration estimation problem, but it also provides an insight into the dynamical behaviour of the system.

2. In Chapter 3, the estimation of analyte concentration is posed as a parameter estimation problem in the multi-compartment ODE model (2.2)-(2.7) derived in Chapter 2. The estimate is computed numerically for the ICS biosensor example of Chapter 2 via the nonlinear least squares method. Using the results of the ODE model, analytic expressions are derived for the finite-sample estimation bias and variance. Then, the attainable improvement in the estimation based on the number of biosensors is evaluated. One of the main results is that the measurements from N biosensors can yield less than $1/N$ estimation variance compared to the measurements of a single biosensor. This result is not specific to the given example and can be generalized to any estimation problem using biosensor arrays, when the biosensors have a saturating behaviour similar to the sigmoidal form illustrated in Fig.3.1. Due to this

nonlinear saturating behaviour, the sensitivity of the biosensor may increase in lower concentrations although the response may decrease.

In the third part of the thesis, we improve target molecule detection of low concentrations by splitting a sensing surface into multiple smaller surfaces that are spaced out in the flow direction. In other words, we investigate the detection improvement obtained by replacing a single sensor by an array of the same total sensing area. Unlike the measurement technique used in Chapter 3, we combine the measurements taken by the individual sensors for detection. The corresponding results in Chapter 4 demonstrate that with a fixed sensing surface area, using an array of multiple sensors instead of a single sensor can substantially improve analyte collection rate, which results in higher response rate. The results are illustrated for two real-life biosensors; the ICS biosensor and the BIACORE surface plasmon biosensor. The results of Chapter 4 can be summarized as follows:

1. Distributing the sensing surface along the flow direction affect the mass-transport limit on the analyte collection rate. When the kinetics condition approaches to the mass-transport limited regime (higher Damkohler number), multiple sensors improve the collection rate more significantly. On the other hand, in the reaction-limited regime, multiple sensors cannot improve analyte collection rate.
2. It is shown that for sufficiently spaced-out sensors in the array, the analyte collection rate is maximized when the sensors have equal size.
3. An explicit formula for the maximum attainable improvement in analyte collection rate is obtained in (4.4), which relates the maximum attainable improvement ratio to the total length of the sensing surface in the array, the height of the flow chamber, the Damkohler and Péclet numbers, and the number of sensors. Using the derived expression, we also discuss the effect of changing these parameters on analyte collection

rate and provide their physical interpretation.

In the last part of the thesis, we construct a mathematical proof to derive a tight upper bound for the modeling error of the two-compartment model. This error bound is of the order of $O(P_{eH}^{-1/3})$, where P_{eH} is the Péclet number.

6.2 Discussion and Future Work

In the following, we consider several interesting possibilities for application and extension of the current work:

1. The developed multi-compartment model is an insightful model, which can be used for design purposes where certain parameters such as binding site concentration, biosensor size, flow chamber dimension, and etc. can be optimized.
2. The developed models in this work can fit in the broad context of transport-binding experiments. For example, they can be used for analysis of thin film deposition processes to study thin film deposition rates.
3. The multi-compartment model derived in Chapter 2 can be generalized to a two-dimensional array of surface-based sensors. The fundamental idea behind the multi-compartment model is the boundary layer formed on the sensor surface due to the large value of the Péclet number. Using the same basics, we can consider two-compartment blocks above sensors in a two-dimensional array. It is possible to derive a similar approximate model with asymptotic analysis.
4. An interesting future work is adaptive sensor scheduling for concentration estimation, where on/off switching of the sensors is adaptively controlled to minimize a cost function of estimation errors and measurement costs. As described previously,

taking measurements affects the governing advection-diffusion system. Not only does sensor switching affect the system state, but it also changes the measurement process on other sensors. Adaptive sensing in this case is a special case of active control problems, where the actions control both the system and the measurements. Besides, the system is partially observed and the optimal switching policy is difficult to obtain analytically. By discretizing the PDE system in time and space, the state and measurement equations can be expressed as

$$\begin{aligned}x_{k+1} &= f(x_k, u_k, w_k) \\z_k &= h_k(x_k, u_k, v_k),\end{aligned}$$

where x_k is the state at time k , u_k is the action at time k , which can be considered a vector of zeros and ones in our case (The values 0 and 1 respectively refer to "off" and "on" states for each sensor). Here w_k and v_k respectively refer to the system noise and the measurement noise. The vector of measurements of all sensors at time k is denoted by z_k . The active control problem in this case can be formulated as minimizing a performance criterion of the form

$$J = E \left\{ \sum_{k=1}^T l_k(x_k, u_k) \right\},$$

where the expectation (denoted as E) is taken with respect to the random variable x_k . In the above equation, T denotes the time horizon over which the performance is optimized. This is a control problem in a hidden Markov model, where the actions affect both the states and the measurement process. Optimal and suboptimal algorithms are presented in [96, 97] for the scheduling of sensors for (finite-state) hidden Markov models using a stochastic dynamic programming framework. However, the

sensor switching does not change the underlying Markov process in [96, 97], whereas in our case, one should consider the effect of sensor switching on the system state. Similar to our problem, the state transition and observation are both adaptively controlled in the work presented in [98]. In this work, the state actions and measurement actions are independent, whereas in our case, one set of actions affect both the state and the measurement. The cost function in [98] has a quadratic form.

5. The multi-compartment model and the results of Chapter 2 and Chapter 3 correspond to the cases where the ratio of the length of the sensor to the height of the flow chamber is not too small ($P_{e_H} \gg 1/\lambda^2$) [1]. In the future, similar analysis can be performed for sensing surface strips which are much narrower than the height of the flow chamber. By small ratio of the sensor length to the height, we mean sensors operating in region (iii) of the phase diagram in Fig.1.2.
6. In Chapter 4, we derive the optimal size of the sensors in the array for maximum analyte collection rate. We assume the sensor spacing provides uniform analyte concentration in the space before the sensors. Computing the required distance can be suggested as an extension to this work. It should be noted that in addition to the boundary layers formed above the sensors, there are interior boundary layers along the flow direction. These boundary layers are formed inside the PDE domain, at the sensor edges in the flow chamber. The thickness of these boundary layers can approximate the required distance between two sensors.
7. The identifiability and stability of the solution of the concentration estimation problem can be investigated in future. Converting the PDE model to the multi-compartment ODE model can make the proof of identifiability and stability easier. However, proving the continuity and injectivity of the nonlinear output least squares is complicated

in general.

8. The proof of the two-compartment model in Chapter 5 can be extended to derive the order of accuracy of the entire multi-compartment model.

Bibliography

- [1] T. Squires, R. Messinger, and S. Manalis, “Making it stick: convection, reaction and diffusion in surface-based biosensors,” *Nature Biotechnology*, vol. 26, pp. 417–426, 2008.
- [2] R. Ackerberg, R. Patel, and S. Gupta, “Heat-mass transfer to a finite strip at small peclet numbers,” *Fluid Mechanics*, vol. 86, pp. 49–65, 1978.
- [3] B. Cornell, V. Braach-Maksvytis, L. King, P. Osman, B. Raguse, L. Wiczorek, and R. Pace, “A biosensor that uses ion-channel switches,” *Nature*, vol. 387, pp. 580–583, 1997.
- [4] P. Leonard, S. Hearty, J. Brennan, L. Dunne, J. Quinn, T. Chakraborty, and R. OKennedy, “Advances in biosensors for detection of pathogens in food and water,” *Enzyme and Microbial Technology*, vol. 32, no. 1, pp. 3–13, 2003.
- [5] V. Krishnamurthy, S. Monfared, and B. Cornell, “Ion-channel biosensors part I: Construction, operation and clinical studies,” *IEEE Trans. on Nanotechnology*, vol. 9, no. 3, pp. 303–312, 2010.
- [6] D. Zhdanov and S. Sorokin, “Biosensor measuring system for the control of biological activity of water solutions,” in *Electronic Instrument Engineering, 2008. APEIE 2008. 9th International Conference on Actual Problems of*, vol. 01, Sept. 2008, pp. 11–14.
- [7] Y. Lin, F. Lu, Y. Tu, and Z. Ren, “Glucose biosensors based on carbon nanotube nanoelectrode ensembles,” *Nano Letters*, vol. 4, no. 2, pp. 191–195, 2004.
- [8] L. C. Clark and C. Lyons, “Electrode systems for continuous monitoring in cardiovascular surgery,” *Annals of the New York Academy of Sciences*, vol. 102, no. 1, pp. 29–45, 1962.
- [9] A. Agah, A. Hassibi, J. D. Plummer, and P. B. Griffin, “Design requirements for integrated biosensor arrays,” in *Proc. of SPIE*, vol. 5699, 2005, pp. 403–413.
- [10] G. MacBeath and S. L. Schreiber, “Printing proteins as microarrays for high-throughput function determination,” *Science*, vol. 289, no. 5485, pp. 1760–1763, 2000.
- [11] J. W. Silzel, B. Cercek, C. Dodson, T. Tsay, and R. J. Obremski, “Mass-sensing, multianalyte microarray immunoassay with imaging detection,” *Clin. Chem.*, vol. 44, no. 9, pp. 2036–2043, 1998.

- [12] M. M. Varma, D. D. Nolte, D. H. Inerowicz, and E. F. Regnier, “High-speed label-free multi-analyte detection through micro- interferometry,” in *Proc. of SPIE*, vol. 4966, no. 9, 2003, pp. 58–64.
- [13] N. Nguyen and S. Wereley, *Fundamentals and Applications of Microfluidics*, ser. Artech House integrated microsystems series. Artech House, 2002.
- [14] F. White, *Fluid Mechanics*. McGraw Hill, 2010.
- [15] J. M. Haile, *Molecular Dynamics Simulation: Elementary Methods*, ser. A Wiley-Interscience publication. Wiley, 1997.
- [16] J. R. Cannon, *The One-Dimensional Heat Equation*. Cambridge University Press and Reading, 1984.
- [17] H. T. Banks and K. Kunisch, *Estimation Techniques for Distributed Parameter Systems*. Birkhäuser, 1989.
- [18] G. Chavent, “Local stability of the output least square parameter estimation technique,” *Matematica Aplicada e Computacional*, vol. 2, pp. 3–22, 1983.
- [19] , “Identifiability of linear systems in hilbert spaces,” *SIAM J. Contr. Optim.*, vol. 21, pp. 501–530, 1983.
- [20] M. Courdresses, M. G. Polis, and M. Amouroux, “On the identifiability of parameters in a class of parabolic distributed systems,” *IEEE Trans. Automat. Contr.*, vol. AC-26, pp. 474–477, 1981.
- [21] C. Groetsch, *The theory of Tikhonov regularization for Fredholm equations of the first kind*, ser. Research notes in mathematics. Pitman Advanced Pub. Program, 1984.
- [22] A. Tikhonov and V. Arsenin, *Solutions of ill-posed problems*, ser. Scripta series in mathematics. Winston, 1977.
- [23] T. Chung, *Computational Fluid Dynamics*. Cambridge University Press, 2002.
- [24] T. Bader, A. Wiedemann, K. Roberts, and U. D. Hanebeck, “Model-based motion estimation of elastic surfaces for minimally invasive cardiac surgery,” in *Proc. of IEEE International Conference on Robotics and Automation (ICRA)*, Rome, April 2007.
- [25] G. E. Karniadakis and S. Sherwin, *Spectral/hp Element Methods for Computational Fluid Dynamics*. Oxford University Press, 2005.
- [26] J. Matthes, L. Gröll, and H. B. Keller, “Source localization by spatially distributed electronic noses for advection and diffusion,” *IEEE Trans. on Signal Processing*, vol. 53, no. 5, pp. 1711–1719, 2005.

- [27] J. Berthier and P. Silberzan, *Microfluidics for Biotechnology*, ser. Artech House integrated microsystems series. Artech House, 2010.
- [28] M. N. Özisik and H. R. B. Orlande, *Inverse heat transfer: fundamentals and applications*. Taylor and Francis, 2000.
- [29] A. Shidfar, R. Zolfaghari, and J. Damirchi, “Application of sinc-collocation method for solving an inverse problem,” *Journal of Computational and Applied Mathematics*, vol. 233, no. 2, pp. 545–554, 2009.
- [30] D. V. Antonov, “Boundary observation of nonstationary neutron transport in a plane-parallel medium,” *Computational Mathematics and Modelling*, vol. 7, no. 4, pp. 339–344, 1996.
- [31] N. V. Kerov, “Solution of the two-dimensional inverse heat-conduction problem in a cylindrical coordinate system,” *Computational Mathematics and Modelling*, vol. 45, no. 5, pp. 1245–1249, 1983.
- [32] A. Nehorai, B. Porat, and E. Paldi, “Detection and localization of vapor-emitting sources,” *IEEE Trans. on Signal Processing*, vol. 43, 1995.
- [33] B. Porat and A. Nehorai, “Localizing vapor-emitting sources by moving sensors,” *IEEE Trans. on signal Processing*, vol. 44, no. 4, pp. 1018–1021, April 1996.
- [34] J. Matthes, L. Gröll, and H. B. Keller, “Source localization by spatially distributed electronic noses for advection and diffusion,” *IEEE Trans. on Signal Processing*, vol. 53, pp. 1711–1719, 2005.
- [35] A. Keats, E. Yee, and E.-S. Lien, “Bayesian inference for source determination with applications to a complex urban environment,” *Atmospheric environment*, vol. 41, no. 3, pp. 465–479, January 2007.
- [36] T. K. Chow, B. Kosovic, and S. Chan, “Source inversion for contaminant plume dispersion in urban environments using building resolving simulations,” in *Proc. of Ninth Annual George Mason University Conference on Atmospheric Transport and Dispersion Modeling*, 2005.
- [37] B. Kosovic, G. Sugiyama, T. K. Chow, K. Dyer, W. Hanley, G. Johannesson, S. Loosmore, J. K. Lundquist, A. Mirin, J. Nitao, R. Serban, and C. Tong, “stochastic source inversion methodology and optimal sensor network design,” in *Proc. of Ninth Annual George Mason University Conference on Atmospheric Transport and Dispersion Modeling*, 2005.
- [38] R. Rapley, P. Robins, and P. A. Thomas, “Source term estimation and probabilistic sensor modelling,” in *Proc. of Ninth Annual George Mason University Conference on Atmospheric Transport and Dispersion Modeling*, 2005.

- [39] L. Leal, *Advanced Transport Phenomena: Fluid Mechanics and Convective Transport Processes*. Cambridge: Cambridge University Press, 2007.
- [40] J. Newman, “The fundamental principles of current distribution and mass transport in electrochemical cells,” *Electroanalytical Chemistry*, vol. 6, pp. 279–297, 1973.
- [41] S. Sjölander and C. Urbaniczky, “Integrated fluid handling system for biomolecular interaction analysis,” *Analytical Chemistry*, vol. 63, pp. 2338–2345, 1991.
- [42] R. A. Vijayendran, F. S. Ligler, and D. E. Leckband, “A computational reaction-diffusion model for the analysis of transport-limited kinetics,” *Analytical Chemistry*, vol. 71, pp. 5405–5412, 1999.
- [43] S. Monfared, V. Krishnamurthy, and B. Cornell, “A molecular machine biosensor: Construction, predictive models and experimental studies,” *Biosensors and Bioelectronics*, vol. 34, no. 1, pp. 261–266, April 2012.
- [44] A. Katiyar, S. Thiel, V. Guliants, and N. Pinto, “Investigation of the mechanism of protein adsorption on ordered mesoporous silica using flow microcalorimetry,” *J. Chromatogr.*, vol. A 1217, pp. 1583–1588, 2010.
- [45] V. Krishnamurthy, S. Monfared, and B. Cornell, “Ion-channel biosensors part II: Dynamic modeling, analysis and statistical signal processing,” *IEEE Trans. on Nanotechnology*, vol. 9, no. 3, pp. 313–321, 2010.
- [46] B. Cornell, *Optical Biosensors: Present and Future*. Amsterdam: Elsevier, 2002, p. 457.
- [47] F. Separovic and B. Cornell, *Biological Membrane Ion Channels*. New York: Springer-Verlag, 2007, pp. 595–621.
- [48] B. Hille, *Ionic Channels of Excitable Membranes*, 3rd ed. Sunderland, MA: Sinauer Associates, 2001.
- [49] S. Chung, O. Andersen, and V. Krishnamurthy, *Biological Membrane Ion Channels*, ser. Biological and Medical Physics, Biomedical Engineering. Springer, 2007.
- [50] “Biosensing with surface plasmon resonance how it all started,” *Biosensors and Bioelectronics*, vol. 10, no. 8, pp. i – ix, 1995.
- [51] X. Yin and S. University, *Optical Nonspecular Phenomena at the Surface Plasmon Resonance and Their Applications*. Stanford University, 2008.
- [52] R. Rich and D. Myszka, “Survey of the year 2001 commercial optical biosensor literature,” *Journal of Molecular Recognition*, vol. 15, pp. 352–376, 2002.

- [53] D. Myszka, T. Morton, M. Doyle, and I. Chaiken, “Kinetic analysis of a protein antigen-antibody interaction limited by mass transport on an optical biosensor,” *Biophysical Chemistry*, vol. 64, pp. 127–137, 1997.
- [54] M. Fivash, E. Towler, and R. Fisher, “Biacore for macromolecular interactions,” *Current Opinion in Biotechnology*, vol. 9, pp. 97–101, 1998.
- [55] D. G. Myszka, X. He, M. Dembo, T. A. Morton, and B. Goldstein, “Extending the range of rate constants available from biacore: Interpreting mass transport-influenced binding data,” *Biophysical Journal*, vol. 75, pp. 583–594, 1998.
- [56] P. Garland, “Optical evanescent wave methods for the study of biomolecular interactions,” *Quarterly Reviews of Biophysics*, vol. 29, pp. 91–117, 1996.
- [57] P. Prinsen and T. Odijk, “Collective diffusion coefficient of proteins with hydrodynamic, electrostatic, and adhesive interactions,” *Journal of Chemical Physics*, vol. 127, no. 11, 2007.
- [58] M. Abolfath-Beygi and V. Krishnamurthy, “Cooperative maximum likelihood estimation for fluid flow dynamics in biosensor arrays,” in *IEEE International Conference on Acoustics, Speech and Signal Processing (ICASSP)*, Prague, Czech Republic, May 2011, pp. 3788–3791.
- [59] —, “Biosensor arrays for collaborative detection of analytes,” in *Proc. of Asilomar Conference on Signals, Systems and Computers*, Pacific grove, CA, November 2011, pp. 1699–1703.
- [60] —, “Detection of target molecules using surface-based biosensor arrays in fluid flows,” in *IEEE International Conference on Acoustics, Speech and Signal Processing (ICASSP)*, Kyoto, Japan, March 2012, pp. 3913–3916.
- [61] M. Abolfath-Beygi, V. Krishnamurthy, and B. Cornell, “Multiple surface-based sensors for enhanced molecular detection in fluid flow systems,” *IEEE Sensor Journal*, vol. 13, no. 4, pp. 1265–1273, April 2013.
- [62] S. Monfared, V. Krishnamurthy, and B. Cornell, “Chemical kinetics and mass transport in an ion channel based biosensor,” in *Proc. of IEEE Conference on Decision and Control*, Atlanta, GA, December 2010, pp. 4685–4690.
- [63] R. W. Glaser, “Antigen-antibody binding and mass transport by convection and diffusion to a surface: A two-dimensional computer model of binding and dissociation kinetics,” *Analytical Biochemistry*, vol. 213, pp. 152–161, 1993.
- [64] J. Brody, P. Yager, R. Goldstein, and R. Austin, “Biotechnology at low reynolds numbers,” *Biophysical Journal*, vol. 71, pp. 3430–3441, 1996.

- [65] D. R. Thévenot, K. Toth, R. A. Durst, and G. S. Wilson, “Electrochemical biosensors: recommended definitions and classification,” *Biosensors and Bioelectronics*, vol. 16, pp. 121–131, 2001.
- [66] A. Sadana and N. Sadana, *Handbook of Biosensors and Biosensor Kinetics*. Elsevier Science, 2010.
- [67] C. Baldwin, *Chemical Reactions*, ser. Material Matters/freestyle Express. Heinemann-Raintree, 2005.
- [68] B. K. Lok, Y. L. Cheng, and C. R. Robertson, “Protein adsorption on crosslinked polydimethylsiloxane using total internal reflection fluorescence,” *Journal of Colloid and Interface Science*, vol. 91, no. 1, pp. 104–116, 1983.
- [69] M. Abolfath-Beygi, V. Krishnamurthy, and B. Cornell, “Multiple surface-based biosensors for enhanced molecular detection in fluid flow systems,” *Sensors Journal, IEEE*, vol. 13, no. 4, pp. 1265–1273, April 2013.
- [70] M. A. Lévêque, “Les lois de la transmission de chaleur par convection,” *Ann. des Mines, Mémoires*, vol. 13, pp. 201–239, 1928.
- [71] L. Graetz, “Über die wärmeleitfähigkeit von flüssigkeiten,” *Annalen der Physik und Chemie*, vol. 25, pp. 337–357, 1885, part II.
- [72] W. Hundsdorfer and J. G. Verwer, *Numerical Solution of Time-Dependent Advection-Diffusion-Reaction Equations*. Springer Computational Mathematics, 2003.
- [73] P. Kokotović, H. K. Khalil, and J. O’Reilly, *Singular perturbation methods in Control: Analysis and design*. Siam, 1999.
- [74] E. Hinch, *Perturbation Methods*, ser. Cambridge Texts in Applied Mathematics. Cambridge University Press, 1991.
- [75] S. Klein, J. Timmer, and J. Honerkamp, “Analysis of multichannel patch clamp recordings by hidden markov models,” *Biometrics*, vol. 53, no. 3, pp. 870–884, 1997.
- [76] P. Amestoy, I. Duff, and J.-Y. L’Excellent, “Multifrontal parallel distributed symmetric and unsymmetric solvers,” *Comput. Methods Appl. Mech. Eng.*, vol. 184, pp. 501–520, 1998.
- [77] L. F. Shampine and M. W. Reichelt, “The matlab ode suite,” *SIAM Journal on Scientific Computing*, vol. 18, pp. 1–22, 1997.
- [78] P. Kaps, S. Poon, and T. Bui, “Rosenbrock methods for stiff odes: A comparison of richardson extrapolation and embedding technique,” *Computing*, vol. 34, pp. 17–40, 1985.

- [79] B. Szabó and I. Babuška, *Introduction to Finite Element Analysis: Formulation, Verification and Validation*, ser. Wiley series in computational mechanics. Wiley, 2011.
- [80] Comsol, *Comsol Multiphysics User's Guide 4.3a*, Comsol, 2012.
- [81] T. E. Tezduyar, R. Glowinski, J. Liou, T. Nguyen, and S. Poole, "Block-iterative finite element computations for incompressible flow problems," in *Proceedings of the 2nd international conference on Supercomputing*, ser. ICS '88, 1988.
- [82] "Comparison of some finite element methods for solving the diffusion-convection-reaction equation," *Computer Methods in Applied Mechanics and Engineering*, vol. 156, no. 1–4, pp. 185–210, 1998.
- [83] D. W. Trott and M. K. Gobbert, "Finite element convergence for time-dependent pdes with a point source in comsol 4," in *Proc. of the COMSOL Conference*, Boston, MA, 2011.
- [84] T. Mason, A. Pineda, C. Wofsy, and B. Goldstein, "Effective rate models for the analysis of transport-dependent biosensor data," *Mathematical Bioscience*, vol. 159, pp. 123–144, 1999.
- [85] D. A. Edwards, "Estimating rate constants in a convection diffusion system with a boundary reaction," *IMA Journal of Applied Mathematics*, vol. 63, pp. 89–112, 1999.
- [86] B. Goldstein, D. Coombs, X. He, A. R. Pineda, and C. Wofsy, "The influence of transport on the kinetics of binding to surface receptors: application to cell and bio-core," *Journal of Molecular Recognition*, vol. 12, pp. 293–299, 1999.
- [87] D. JO'Shannessy, "Determination of kinetic rate and equilibrium binding constants for macromolecular interactions: a critique of the surface plasmon resonance literature," *Current Opinion in Biotechnology*, vol. 5, pp. 65–71, 1994.
- [88] D. G. Myszka, "Kinetic analysis of macro molecular interactions using surface plasmon resonance biosensors," *Current Opinion in Biotechnology*, vol. 8, pp. 50–57, 1997.
- [89] P. Schuck, "Use of surface plasmon resonance to probe the equilibrium and dynamic aspects of interactions between biological macromolecules," *Annual Review of Biophysics and Biomolecular Structure*, vol. 26, pp. 541–566, 1997.
- [90] P. Deuffhard, *Newton Methods for Nonlinear Problems*, ser. Springer Series in Computational Mathematics. Springer, 2011.
- [91] A. Ackleh, E. Allen, R. Kearfott, and P. Seshaiyer, *Classical and Modern Numerical Analysis: Theory, Methods and Practice*, ser. Chapman and Hall/CRC Numerical Analysis and Scientific Computation Series. Taylor & Francis, 2011.

- [92] D. Myszka, “Kinetic, equilibrium, and thermodynamic analysis of macromolecular interactions with biacore,” *Methods in Enzymology*, vol. 323, pp. 325–340, 2000.
- [93] L. Graetz, “Über die wärmeleitfähigkeit von flüssigkeiten,” *Annalen der Physik und Chemie*, vol. 18, pp. 79–94, 1883, part I.
- [94] L. C. Evans, *Partial differential equations*, 2nd ed. American Mathematical Society, 2010.
- [95] W. Hundsdorfer and J. Verwer, *Numerical Solution of Time-Dependent Advection-Diffusion-Reaction Equations*, ser. Springer Series in Computational Mathematics. Springer, 2007.
- [96] V. Krishnamurthy, “Algorithms for optimal scheduling and management of hidden markov model sensors,” *Signal Processing, IEEE Transactions on*, vol. 50, no. 6, pp. 1382–1397, 2002.
- [97] V. Krishnamurthy and D. V. Djonin, “Structured threshold policies for dynamic sensor scheduling a partially observed markov decision process approach,” *Signal Processing, IEEE Transactions on*, vol. 55, no. 10, pp. 4938–4957, 2007.
- [98] I. Meier, L. J. Peschon, and R. Dressler, “Optimal control of measurement subsystems,” *Automatic Control, IEEE Transactions on*, vol. 12, no. 5, pp. 528–536, October 1967.